

# **Development of GaN Diodes with NiN Electrodes for Power Electronics and Temperature Sensing Applications**

**NiN 電極を有するパワーエレクトロニクス及び  
温度センシング用 GaN ダイオードの研究**



**Department of Electrical and  
Electronic Engineering**

**李小波**

**March 2020**



## Abstract

Schottky barrier diode (SBD) is a critical device of antenna-rectifier (rectenna) circuit in the microwave wireless power transmission systems, which is widely used in electric vehicle power charging, energy harvesting systems, power source, and in-building wireless power distribution. Gallium nitride (GaN)-based materials exhibit many extraordinary features, including large bandgap, higher breakdown field, higher electron mobility and higher electron saturation velocity, accordingly GaN-SBDs have attracted much attention for improving the efficiency of microwave wireless power transmission system. However, the most common Ni anode is reported to form a Ni-N alloy (a mixture of Ni<sub>3</sub>N, NiN and so on) after thermal treatment, resulting in the degradation of stability. This is required more stability materials to replace the Ni for the Schottky contact application. Moreover, GaN-based electronic devices have shown the excellent thermal stability and strong temperature dependence, meaning that it can be a possible candidate for temperature sensing. In this thesis, we discussed the synthesis and application of nickel nitride (Ni<sub>x</sub>N) for GaN electron devices application. Meanwhile, we also investigated the GaN based pn diodes and SBD diodes for temperature sensor application.

Ni<sub>x</sub>N films were deposited by magnetron reactive sputtering under varying N<sub>2</sub> partial pressure (P(N<sub>2</sub>)) conditions range from 0.005 to 0.184 Pa. With the increasing P(N<sub>2</sub>), the deposition rate decreases while the resistivity and root mean square roughness increased. X-ray diffraction (XRD) and X-ray photoelectron spectra (XPS) indicate that Ni<sub>4</sub>N and Ni<sub>3</sub>N phases dominate the films at low and medium P(N<sub>2</sub>), respectively. In addition, Ni<sub>2</sub>N phase can be also obtained at high P(N<sub>2</sub>). The Ni/N ratio evaluated from the energy dispersive X-ray spectrum is consistent with the Ni<sub>x</sub>N phases showed in the XRD spectra of different P(N<sub>2</sub>). Comparing with the GaN diodes with Ni anode, the Schottky barrier height and turn-on voltage of the Schottky barrier diodes with Ni<sub>x</sub>N anode are increased with 0.03~0.18 eV and 0.03~0.15 V, respectively. Capacitance-voltage curves demonstrated that good interface quality with no obvious hysteresis is realized.

Especially, Ni<sub>3</sub>N anode diodes obtained at medium P(N<sub>2</sub>) possess a high barrier height and a low reverse leakage current and are regarded as a promising anode material. The temperature-dependent current voltage characteristics demonstrate that the Ni<sub>3</sub>N-SBDs have better thermal stability than that of Ni-SBDs, owing to the suppression of interface

reaction between Ni and GaN. In addition, the thermal stability of GaN diode with Ni<sub>3</sub>N anode is potential for temperature sensing application with the sensitivity of approximately 1.3 mV/K.

P-NiO/n-GaN pn diodes and TiN/GaN SBDs were investigated extensively by varying the device diameter and current level. For the NiO/GaN pn diode, it is demonstrated that the series resistance and ideality factor dominate the sensitivity at the fully-turn-on state. However, the series resistance weakly influenced the sensitivity of the TiN/GaN SBDs temperature sensor at the fully-turn-on state. After subtracting the component of series resistance, the sensitivity decreases and increases with the increased device diameters for the p-NiO/n-GaN pn diodes and TiN/GaN SBDs temperature sensors, respectively.

For both type temperature sensors, in the sub-threshold state, a good linear relationship between sensitivity and the corresponding current density have been observed for devices with different diameters. A low current density is corresponding to the high sensitivity. The NiO/GaN pn diodes and TiN/GaN SBD presenting good thermal stability and linearity from 25 to 200 °C are promising candidates for temperature sensing application.

We also investigated the NiN/GaN SBD for temperature sensor application. While in the sub-threshold region, a good linear relationship between sensitivity and the corresponding current density have been observed for a 200µm diameter NiN/GaN SBD temperature sensor. Comparing with TiN, Ni and NiN electrode GaN SBD temperature sensor, the NiN electrode device shows a near-ideal theoretical sensitivity of a GaN SBD temperature sensor which is calculated by the TE model from GaN based SBDs.

We fabricated NiN-gated AlGaIn/GaN HFETs by magnetron reactive sputtering with a Ni target in an ambient Ar and N<sub>2</sub> mixture gas. Gate leakage current characteristics shows that the reverse leakage current of NiN-gated HFETs is approximately reduced by one order of magnitude and the ON/OFF drain current ratio increases two order of magnitudes comparing with the conventional Ni-gated HFETs. The temperature-dependent gate leakage current-voltage characteristics demonstrate that the NiN-gated HFETs have better thermal stability.

**Keywords:** GaN, Magnetron reactive sputtering, NiN, SBD, Temperature sensor.

# CONTENTS

<b>Chapter 1: Introduction .....</b>	<b>- 1 -</b>
§1.1. Background .....	- 1 -
§1.1.1. Wireless power transmission .....	- 1 -
§1.1.2. Rectenna circuit .....	- 4 -
§1.1.3. Semiconductor materials from Si to GaN.....	- 5 -
§1.1.4. The properties of GaN .....	- 5 -
§1.2. Technology and current research of GaN based electronic devices.....	- 8 -
§1.2.1. GaN based SBD.....	- 8 -
§1.2.2. Temperature sensor application .....	- 10 -
§1.2.3. The AlGaIn/GaN HFET .....	- 12 -
§1.3. Motivation of this research .....	- 13 -
§1.4. Outline of thesis .....	- 14 -
§1.5. References.....	- 17 -
<b>Chapter 2: Synthesis and Characteristics of Nickel Nitride.....</b>	<b>- 23 -</b>
§2.1. Introduction.....	- 23 -
§2.2. Synthesis of Ni <sub>x</sub> N films at room temperature .....	- 24 -
§2.2.1. Reactive sputtering technology .....	- 24 -
§2.2.2. Deposition of Ni <sub>x</sub> N film .....	- 25 -
§2.3. Characteristics of Ni <sub>x</sub> N films at room temperature.....	- 26 -
§2.3.1. Deposition rate and resistivity of Ni <sub>x</sub> N films .....	- 26 -
§2.3.2. The phases of Ni <sub>x</sub> N films.....	- 29 -
§2.3.3. The surface morphologies of Ni <sub>x</sub> N films.....	- 31 -
§2.3.4. The chemical compositions of Ni <sub>x</sub> N films .....	- 33 -
§2.3.5. The atom proportion of Ni <sub>x</sub> N films .....	- 34 -
§2.4. Conclusion .....	- 36 -
§2.5. References.....	- 37 -
<b>Chapter 3: Ni<sub>x</sub>N film for GaN-based SBD Application .....</b>	<b>- 39 -</b>
§3.1. Introduction.....	- 39 -
§3.2 Devices structure and fabrication.....	- 40 -
§3.3. Ni <sub>x</sub> N/GaN SBDs characteristics.....	- 41 -
§3.3.1. <i>I-V</i> characterization.....	- 41 -
§3.3.2. <i>C-V</i> characteristics .....	- 45 -
§3.4. Thermal stability of Ni <sub>3</sub> N/GaN SBD .....	- 47 -
§3.4.1. Characteristic of Ni <sub>3</sub> N/GaN SBD at room-temperature .....	- 48 -
§3.4.2. Characteristic of Ni <sub>3</sub> N/GaN SBD at different temperature .....	- 49 -
§3.5. Conclusion .....	- 53 -
§3.6. References.....	- 54 -
<b>Chapter 4: GaN-based Diode for Temperature Sensor Application .....</b>	<b>- 57 -</b>

§4.1. Introduction.....	- 57 -
§4.2. NiO/GaN PND temperature sensor.....	- 57 -
§4.2.1. Theoretical modeling of a p-NiO/n-GaN heterojunction diode.....	- 58 -
§4.2.2. Device structure and fabrication.....	- 58 -
§4.2.3. Characteristics and discussion.....	- 59 -
§4.3. Correlation between anode area and sensitivity for the TiN/GaN SBD temperature sensor.....	- 65 -
§4.3.1. Device structure and fabrication.....	- 66 -
§4.3.2. Theoretical modeling of the Schottky diode.....	- 66 -
§4.3.3. Characteristics and discussion.....	- 67 -
§4.4. High linear and near-ideal NiN/GaN SBD temperature sensor.....	- 75 -
§4.4.1. NiN/GaN SBD temperature sensor in sub-threshold region.....	- 75 -
§4.4.2. Theoretical sensitivity of GaN-based SBD temperature sensor.....	- 77 -
§4.4.3. The ideal GaN-based SBD temperature sensor.....	- 77 -
§4.5. Conclusion.....	- 80 -
§4.6. References.....	- 82 -
<b>Chapter 5: NiN Gate AlGaIn/GaN HFETs.....</b>	<b>- 85 -</b>
§5.1. Introduction.....	- 85 -
§5.2. Device structure and fabrication.....	- 85 -
§5.3. Devices performances.....	- 86 -
§5.4. Conclusion.....	- 90 -
§5.5. References.....	- 91 -
<b>Chapter 6: Conclusions and Future Works.....</b>	<b>- 93 -</b>
§6.1. Summary and conclusions.....	- 93 -
§6.2. Suggestion for future works.....	- 94 -
<b>Acknowledgements.....</b>	<b>- 95 -</b>
<b>Publication list.....</b>	<b>- 97 -</b>

## Chapter 1: Introduction

### §1.1. Background

#### §1.1.1. Wireless power transmission

In recent years, with the development of the Internet of Things (IoT), large number of information is exchanged over the Internet, and barriers to information communication have further dropped, a vast community is about to be born based on the IoT. On the other hand, the number and performance of sensors and communication devices required for information collection and communication are expected to increase explosively, in which wireless power transmission is attracting attention as one of the power supply technologies due to its crucial role in these areas. Wireless power transmission is an epoch-making technology which can transmit power to other places without electrical contact, and makes it possible to freely constrain physical equipment such as power cords for electrical and electronic equipment.

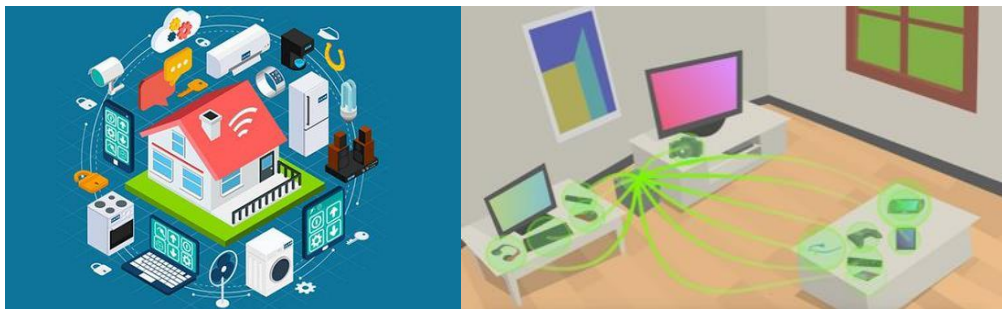


Fig. 1-1. Schematic diagram of IOT (left) and (right) wireless power transmission.

In generally, wireless power transmission can be classified into two kinds which are non-radiative coupling-based charging and radiative radio frequency (RF)-based charging [1]. The non-radiative coupling-based charging consists of magnetic resonance coupling [2], inductive coupling [3] and capacitive coupling [4] three techniques. For the radiative RF-based charging, it consists of non-directive RF power transfer and directive RF power

beamforming [5]. Due to the technical limitation [1], wireless charging is usually realized through three techniques, that are magnetic inductive coupling, magnetic resonance coupling, and RF radiation.

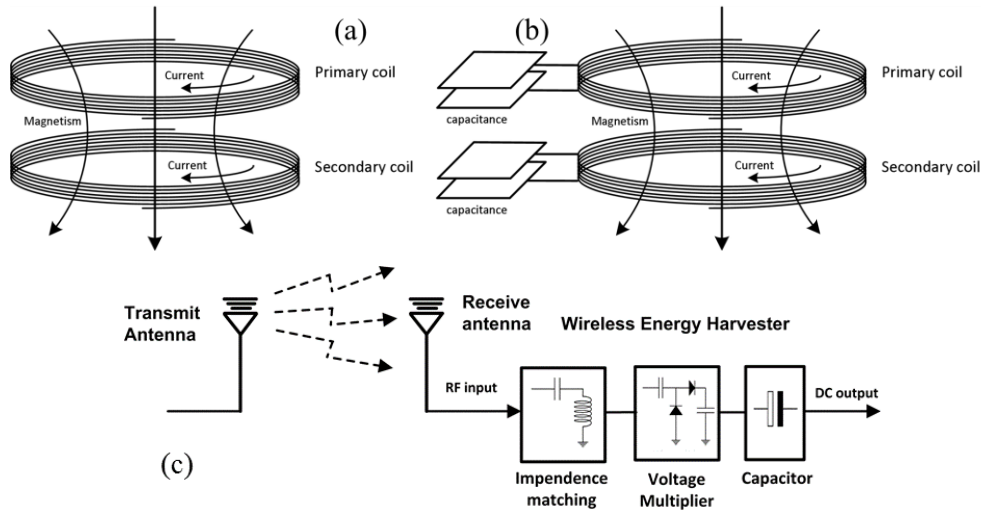


Fig. 1-2. Models of wireless charging systems for inductive coupling (a), magnetic resonance coupling (b), and RF radiation (c). [1]

Fig. 1-2 (a) shows the reference model of inductive coupling wireless charging system which is based on magnetic field induction that delivers electrical energy between two coils. For the inductive coupling, its typically operating frequency is in the kilo Hertz range. In order to enhance charging efficiency, the secondary coil should be tuned at the operating frequency [6]. Due to attenuate quickly for larger quality values of the transferred power [7], the quality factor is usually designed in small values [8]. Because of lack of the compensation of high quality factors, the effective charging distance is generally within 20cm [6]. Although the transmission range is limited, the effective charging power may be very high even kilowatts for the electric vehicle charging. [9, 10] Advantages of magnetic inductive coupling include safety, convenient operation, and high near range efficiency. Therefore, it is suitable for mobile devices and is very popular.

Magnetic resonance coupling [11] is shown in Fig. 1-2 (b), which is based on evanescent-wave coupling which creates and transfers electrical energy between two resonant coils by varying or oscillating magnetic fields. Since the two resonant coils operating at the same resonant frequency are firmly coupled, high energy transmission

efficiency can be achieved while leakage to non-resonant externalities is small. For example, a new prototype [12] has been shown to achieve a maximum power transfer efficiency of 92.6% over a distance of 0.3 cm. Due to the nature of resonance, magnetic resonance coupling also has the advantage of immunity to the surrounding environment and line of sight transfer requirements. Additionally, magnetic resonance coupling can be applied between one transmit resonator and a number of receive resonators, identifying that can charge multiple devices [13-17] at the same time. The typically operated frequency of the magnetic resonance coupling is in the megahertz frequency range, therefore the quality factor is typically high. As the charging distance increases, the high quality factor is conducive to reduce the sharp drop in the coupling coefficient, thereby reducing the charging efficiency. Consequently, it is possible to extend the effective power transfer distance to meter range.

Diffused RF/microwave are used as a medium to carry radiant energy for the RF radiation[18], furthermore, the typically travels speed is the velocity of light in the the line of sight, and the Typical RF/microwave frequencies range from 300 MHz to 300 GHz [19]. As shown in Fig. 1-2 (c), for a microwave power transmission system, the power transmission starts with the AC-to-direct current (DC) conversion, followed by a DC-to-RF conversion through Hetero-junction Field Effect Transistor (HFET) or magnetron at the transmitter side. After propagating through the air, the RF/microwave captured by the receiver rectenna are rectified into electricity again, through an RF-to-DC conversion.

Table 1-1 Comparison of different wireless charging techniques.

Wireless charging technique	Inductive coupling	Magnetic resonance coupling	RF radiation
Advantage	Simple implementation	Charging multiple devices simultaneously on different power High charging efficiency Nonline-of-sight charging	Long effective charging distance Suitable for mobile applications <b>Miniaturization</b>
Effective charging power	mW~kW	W~kW	0.1~several W
Power transfer efficiency	70~90%	40~90%	50~90%
Operating frequency	kHz range	MKz range	From 300MHz to 300GHz
Effective charging distance	From a few millimeters to a few centimeters	From a few centimeters to a few meters	Typically within several tens of meters, up to several kilometers

The RF-to-DC conversion efficiency is highly dependent on the accuracy of the impedance matching between the antenna and the voltage multiplier, the captured power density at receive antenna, and the power efficiency of the voltage multiplier that converts the received RF signals to DC voltage [20]. The advantage of the RF radiation is long effective charging distance and suitable for mobile applications, and the effective charging distance is typically within several tens of meters, up to several kilometers. The summary of the three wireless charging techniques is shown in Table 1-1.

### §1.1.2. Rectenna circuit

In microwave wireless power transmission system, the antenna-rectifier (rectenna) is considered to be a key section in microwave circuit, which is adopted to convert the RF to DC or opposite [21-23]. Fig. 1-3 shows the schematic diagram of a rectenna circuit, in which receiving antenna, band reject, rectifier, DC bypass filter and load can be integrated in to a chip. In this case, it is suitable for reducing power consumption and the overall size, and can be widely used in the mobile applications. Among them, the rectifier is a key device in the rectenna circuit, which is mostly realized by a Schottky barrier diode (SBD). However, some demands, such as low power losses [24], high breakdown voltage [25], low resistance and low parasitic capacitance are raised for rectenna circuit. SBD as the critical device of rectenna circuits in microwave wireless power transmission systems, is also widely used in energy harvesting systems, power source, and in-building wireless power distribution, is facing a new challenge.

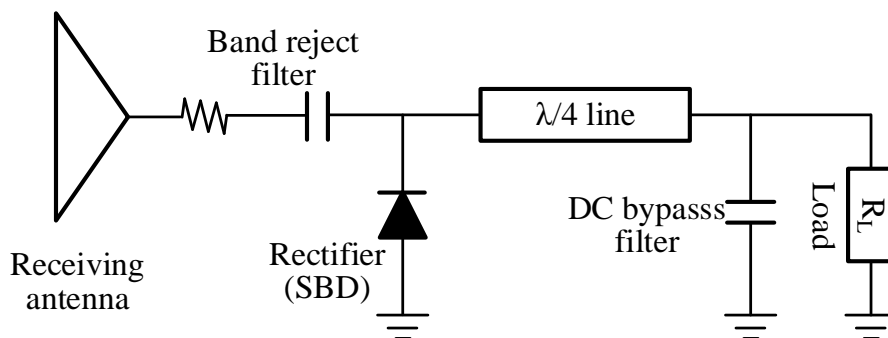


Fig. 1-3. Schematic diagram of a rectenna circuit.

### §1.1.3. Semiconductor materials from Si to GaN

Semiconductor materials can be traced back to the 19th century, which have a long history from discovery to development, from use to innovation. In 1930, the production of cuprous oxide rectifiers was successful and widely used, and semiconductor materials began to receive attention. Since the first germanium semiconductor transistor was invented by John Bardeen and Walter Brattain in 1947, the semiconductor industrial has had a booming development [26]. In the late 1950s, the development of thin film growth technology and the invention of integrated circuits, the microelectronics technology was further developed. Then, silicon (Si) became the dominated semiconductor with the standard CMOS process [27, 28]. In 1960s, the second generation of semiconductor materials represented by gallium arsenides (GaAs) materials were used to make semiconductor lasers, solid-solution semiconductors, and development in infrared, which expanded application of semiconductor materials. With the rapid development of mobile communication technology since the 1990s, semiconductor materials such as GaAs and indium phosphide (InP) have become the focus of high-speed high-frequency and high-power excitation optoelectronic devices. However, Si or GaAs material is limited for application in high temperature, high power and high frequency situation for that all these processes tend to consume extra power, generate heat and finally make the device failed at a rising temperature [29]. In recent years, research on new semiconductor materials has made breakthroughs. The advanced semiconductor materials represented by Gallium nitride (GaN) have begun to show superior superiority and are called the new engine of the communication and IOT industry.

### §1.1.4. The properties of GaN

GaN is a extremely stable and hard high melting point III-V semiconductor compound whcih is insoluble in water and acids at the room temperature. As show in Fig. 1-4, GaN mainly consists of zinc-blende (ZB) and hexago nal wurtzite (WZ) structure. Two kinds types structures exist Polarization properties, but the ZB type is metastable structure. Due to the strong polarization properties and more stablility, the WZ GaN is predominantly used in research and industry [31].

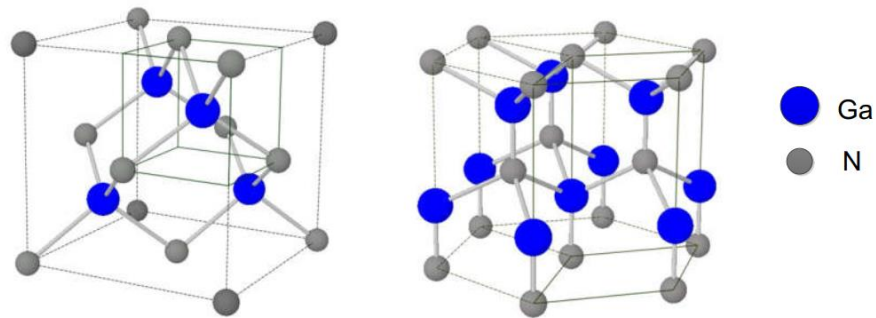


Fig.1-4. Two types ZB (left) and WZ (right) crystal structures of GaN.

For the WZ form, each nitrogen atom is bonded to four gallium atoms and vice versa in a tetrahedral bond configuration. Due to all gallium-to-nitrogen bonds parallel to the  $[0001]$  (Ga-face) or  $[000\bar{1}]$  (N-face) axis pointing in the same direction, uniaxial anisotropy about this axis is present, resulting in net spontaneous polarization along the same axis (shown in Fig. 1-5). The Ga-face and N-face of the GaN film have different physical and chemical properties. Compared with the N-face polarized film, the surface of the Ga-face polarized film is smoother, and the heteropolar structure of its polarization group nitride is superior to the plane polarization. Thus the base heterostructure currently studied is basically Ga-face polarized wurtzite structure[32, 33].

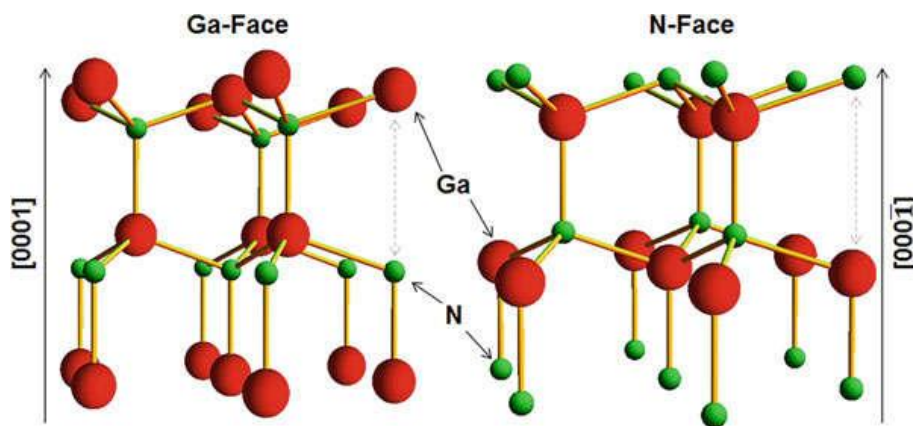


Fig. 1-5. Three-dimensional stick-and-ball illustration of “wurtzite” GaN grown in the Ga-face (left) and N-face (right) direction [34]

Table 1-2. Properties of main semiconductors

	Si	GaAs	6H-SiC	GaN
Bandgap (eV)	1.12	1.42	3.21	3.4
Lattice constant (nm)	0.543	0.565	0.308	0.319
Dielectric constant	11.9	12.9	10.32	10.4
Thermal conductivity (W/cmK)	1.56	0.46	4.9	1.3
Electron mobility (cm <sup>2</sup> /Vs)	1450	8000	400	1200 (bulk) 2000 (2DEG)
Breakdown field (V/cm)	3×10 <sup>5</sup>	4×10 <sup>5</sup>	3×10 <sup>6</sup>	3.3×10 <sup>6</sup>

The table 1-2 shows the properties of main semiconductors, comparing with other semiconductors. The GaN has these properties:

1. GaN is a direct bandgap semiconductor with a large band gap. From the Table 1-1, the band gap width of GaN (3.4 eV) is much larger than that of Si, GaAs and InP. Due to fewer intrinsic carriers at high temperatures and high radiation, intrinsic temperature of GaN-based materials is very high, which is very beneficial for manufacturing high temperature and high power devices. Therefore, compared with Si and GaAs devices, the operating temperature of GaN-based devices is much higher.

2. GaN has high breakdown field of  $3.3 \times 10^6$  V/cm which is about ten times comparing with the GaAs and Si. This property shows that the GaN is very suitable for preparing high-voltage electronic devices. It is also the physical basis for the application in high-voltage switching diodes which is widely required in the power electronic industry.

3. GaN has high electron mobility, implying that the GaN has good carrier transport properties and can be applied to the preparation of high-frequency microwave electronic devices.

Due to its excellent performances, GaN-based power devices such as transistors and rectifiers are promising candidates for the next generation high-efficiency power converters. Accordingly, GaN-SBDs have attracted much attention for improving the efficiency of a microwave wireless power transmission system. GaN-based electronic devices have shown the excellent thermal stability and strong temperature dependence, meaning that it can be a possible candidate for temperature sensing application.

Table 1-3. The parameter comparison table between Si, GaAs and GaN.

Parameters and Test Conditions	Si (HSMS 286X)	GaAs (MA4E1317)	GaN ([34])
Total Capacitance at 0V at 1MHz (pF)	0.3	0.045	0.35
Series Resistance at +10 mA ( $\Omega$ )	6	4	5.2
Forward Voltage at +1 mA (V)	0.35	0.7	0.25
Breakdown Voltage (V)	4	7	36
Time constant (pS)	1.8	0.18	1.82
Cut-off frequency (GHz)	88	880	87.5
$V_{br} \cdot f_c$ (VTHz)	0.352	6.16	3.15

For the GaN-based SBD, the excellent performance is present due to the properties of GaN materials. The table 1-3 shows the parameter comparison of there types ( Si-, GaAs- and GaN-based) SBDs. Due to utilization of the diode with large area, the parameters of the GaN is less than that of GaAs, which is expected to become higher in dot-type diode with small area and lower capacitance value. From the table, the significant high breakdown voltage is observed for GaN compared to Si and GaAs. Combine the high breakdown voltage with ever-increasing cut-off frequency, the optimized GaN-based diode has the significant promising to beyond the GaAs diode for power switching applications.

## §1.2. Technology and current research of GaN based electronic devices

### §1.2.1. GaN based SBD

GaN-based diodes mainly include PN junction diodes and SBD. The characteristics of PN junction diodes are electrons and holes participate in conduction at the same time. Their breakdown voltage is high, reverse leakage current is small, but the turn-on voltage is large. The GaN SBD formed by metal-GaN contact, which has only one kind of carrier participating in conduction. Its recovery time is short, the on-resistance and turn-on voltage are small, but its leakage current is large, and breakdown voltage is small. The energy-band diagrams [35] and a structure typical planar structure of n-type GaN-based SBD are show in the Fig. 1-6.

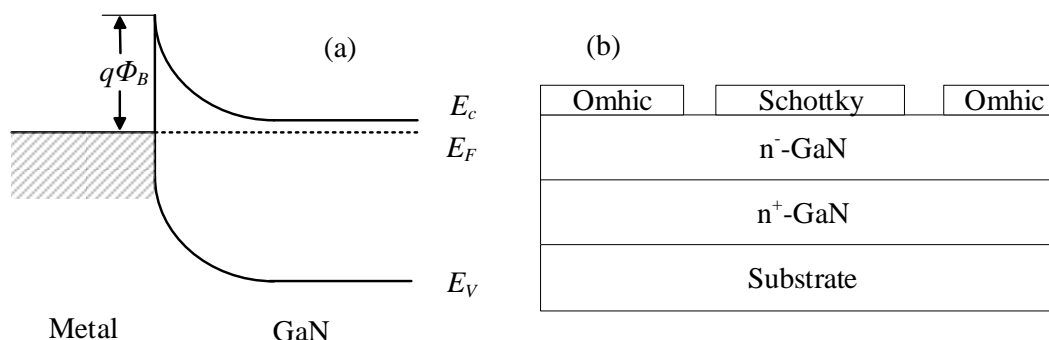


Fig. 1-6. (a) Energy-band diagrams of metal/n-GaN Schottky contact and (b) typical planar structure of GaN-based SBD.

The Schottky barrier height (SBH)  $\Phi_B$  is defined by the difference between the metal work function and the electron affinity of the semiconductor. In this case, for a n-type GaN, the metals with high work function are usually used for the anode-contact in the n-GaN-based SBDs. In the past years, the studies have invested many metals such as Platinum (Pt), palladium (Pd), gold (Au), Titanium (Ti), Wolfram (W), Nickel (Ni) et al [36-40] for n-GaN SBD application. The SBH and the turn-on voltage are in the region of 0.5~1.2 eV and 0.3~0.9 V, respectively. Nowadays, due to its relatively high work function, good adhesion as well as low cost, Ni is most commonly used as Schottky contact in the GaN-based SBDs [37, 41-44]. However, the Ni anode is reported to form Ni-N alloy (a mixture of Ni<sub>3</sub>N, Ni<sub>4</sub>N and so on) after thermal treatment, resulting in the degradation of stability [37, 45]. In this case, researchers are devoted to study more stability schottky-contact materials.

In 2010, metal nitride such as titanium nitride (TiN), molybdenum nitride (MoN<sub>x</sub>) and zirconium nitride (ZrN<sub>x</sub>) were synthesized by reactive sputtering under the argon and nitrogen and used for GaN based Schottky contact application.[46] These metal nitrides were identified as metalloid and displayed more higher SBH comparing with the pure metal. Especially for the ZrN<sub>x</sub> contact, the ideality factor and SBH were improved after annealing at 800 C for 30 s.

In 2013, TiN employed as Schottky contact was used in the HFET and showed good thermally stability [47]. Further research on TiN SBD was reported in 2014 [48], in which several TiN films are deposited using different N<sub>2</sub>/Ar reactive/inert sputtering gas ratios,

thereby varying the nitrogen content present in the sputtering gas. After thermal treatment at 850 °C for 1 min, the TiN and MoN electrodes still exhibit rectifying characteristics, while the MoSiN degrades to an ohmic-like contact.

### **§1.2.2. Temperature sensor application**

With the development of technology, temperature sensors, as one of the most widely used sensors, have been widely used in medical, industrial, aviation and civil fields. Nowadays, temperature sensing is a challenging task in the harsh environment such as high radiation levels. The most common temperature sensors among all commercially available sensors, which are being used in harsh environments, are optical sensors, thermocouples, resistive temperature detectors, thermistors, and semiconductor temperature sensors.[49, 50] Comparing with other traditional temperature sensors, semiconductor temperature sensors have many advantages such as high sensitivity, small size, low power consumption, and strong anti-interference ability [51], which are suitable for applications in harsh environments and easier integration in the integrated circuits (IC) and optoelectronic integrated circuit (OEIC). On the other hand, the semiconductor temperature sensor is more capable of temperature detection in electrochemical and photolytic water with its excellent performance. Therefore semiconductor diodes such as Schottky barrier diode (SBD) and pn diode (PND) are commonly used for temperature sensor application.

However, in the field of high temperature measurement, temperature sensors based on traditional semiconductor materials (Si and GaAs) have gradually failed to meet the requirements of social development. For example, when it comes to high temperature detection, the semiconductor characteristics of Si will change, which makes operating environment of most Si-based devices not suitable to exceed 150 °C. [52, 53] GaN-based electronic devices have shown the excellent thermal stability and strong temperature dependence, which shows the great potential in temperature sensing application. The sensing ability of a diode temperature sensor bases on the quasi-linear dependence of forward voltage on temperature, requiring good thermal stability and linearity. Their

capability of high-temperature operation allows a higher junction/ambient temperature, which is beneficial to simplify the cooling solution.

Table 1-3. The comparison of sensing properties for different types of temperature sensors.

Temperature sensor	Types	Current range (A)	Temperature range (K)	Sensitivity (mV/K)	Ref.s
<b>LED</b> (InGaN/AlGaN)	DH	0.01-0.1	300-400	2.3	[54]
<b>LED</b> (InGaN/AlGaN)	DH	$10^{-5}$ - $10^{-10}$	20-550	5.8~6.5	[55]
<b>HEMT</b> (GaN/AlGaN)	SH	9 (V)	298-523	6.5	[56]
<b>HEMT</b> (GaN/AlGaN)	SH	12 (V)	298-523	0.350	[57]
<b>PN diode</b> (GaN/SiC)	SH	$10^{-3}$ - $10^{-5}$	300-650	1.5-2.2	[58]

In 2004 [54], Y. Xi et al reported a double-heterostructure (DH) GaInN/AlGaN ultraviolet (UV) light-emitting diodes (LEDs) for temperature sensor application. The sensor sensitivity is 2.3 mV/K at a given current of 10 mA. In their study, a theoretical expression of the temperature coefficient of the diode forward voltage is developed. The three main contributions to the temperature coefficient are the intrinsic carrier concentration, the bandgap energy, and the effective density of states. In 2018 [55], V. A. Krasnov et al also reported the GaInN/AlGaN LEDs temperature sensor. They employed a commercial NICHIA NLPB500 blue LED, and obtained a higher sensitivity of 6.5 mV/K.

In 2013 [56], A. M. H. Kwan et al reported a HEMT based integrated over-temperature protection circuit, in which 6.5 mV/K sensitivity was obtained at the voltage of 9 V. In the next year [57], they reported another AlGaN/GaN HEMT integrated temperature sensor with highly linear and a sensitivity of 0.35 mV/K at 12 V.

In 2017 [58], S. Madhusoodhanan et al reported a GaN/SiC single heterojunction (SH) diode temperature sensor. In their study, four diameters devices were fabricated and measured for sensor application, and sensitivity of 2.25 mV/K was obtained from a 400  $\mu\text{m}$  diameter device at the forward current of 1mA.

The comparison of these GaN-based temperature sensors focused on the LEDs and

HEMTs is listed in Table 1-3. For the diodes temperature sensors, there are many reports related SiC based [59-62]. However, SiC SBDs temperature sensors are difficult to integrate on the GaN based IC system for detecting temperature in situ. However, there are few reports about the GaN diodes temperature sensors.

### §1.2.3. The AlGaN/GaN HFET

AlGaN/GaN HFET is an important representative of GaN electronic devices which is also named as high electron mobility transistor (HEMT). Due to its application prospects in the high temperature, high frequency, high power fields, AlGaN/GaN heterostructure becomes one of the hot spots in recent years. From the perspective of output power and frequency, AlGaN/GaN HFETs are very suitable for high-frequency and high-power applications such as wireless communication base stations, radar and automotive electronics. In the aerospace, nuclear industry, military electronics, which require high chemical and thermal stability, AlGaN/GaN HFET is also one of the ideal candidate devices.

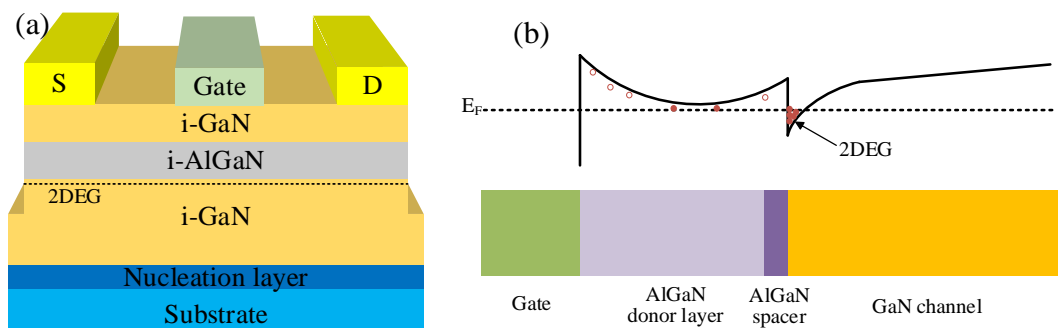


Fig. 1-7. (a) A typical AlGaN/GaN HFETs Structure, (b) the band diagram of the AlGaN/GaN heterostructure.

The typical AlGaN/GaN HFET structure was shown in Fig. 1-7 (a). The epitaxial layers were usually grown on a Si, silicon carbide SiC or sapphire substrate by metal organic chemical vapor deposition (MOCVD) or molecular beam epitaxy (MBE).[63, 64] The epitaxial layers from bottom to top are nucleation layer, i-GaN channel layer, i-AlGaN barrier layer, and cap layer. Due to the strong polarization effect of AlGaN/GaN heterostructure, the density of 2DEG for the undoped AlGaN/GaN heterostructure can be

as high as  $\sim 10^{13}$  /cm<sup>2</sup>, which has one order of magnitude higher than that of the AlGaAs/GaAs heterostructure [65].

In our previous work, Ni and TiN electrodes are normally used to develop GaN Schottky diode. TiN has lower turn-on voltage and comparable breakdown voltage comparing with Ni. However, the reverse leakage current is relative higher [66]. To suppress the reverse leakage current, new gate structure is necessary.

### **§1.3. Motivation of this research**

Currently, most commercial SBDs are Si-based or GaAs-based. However, the traditional GaAs- and Si-based commercial SBDs could not meet the development of the microwave wireless power transmission technology, which requires high conversion efficiency under high frequency and high voltage operation. In order to meet the requirement of the microwave wireless power transmission technology development, GaN-based SBD is investigated and has been used in the rectenna circuits.

Generally, the characteristics of the power devices exhibiting temperature dependence will be compromised as the junction/ambient temperature varies during operation. In addition, high temperature environment operation as well as the self-heating effect of a power device will obviously rise the junction temperature, and then deteriorate the device performance. Therefore, the thermal stability of the device and its performance at different temperatures become especially important.

Ni has been widely cited on SBDs due to its relatively high work function as well as low cost. However, Ni anode GaN SBD appears degradation after thermal treatment due to Ni-N alloy (a mixture of Ni<sub>3</sub>N, NiN and so on) in the interface of Ni and GaN layer. We previously investigated the electrical performance of SBDs with TiN contact fabricated by reactive sputtering. The TiN SBDs have a lower turn-on voltage compared with Ni SBDs and better sensitivity for temperature sensing application. However, the SBDs with TiN electrode suffer from a problem of relatively larger reverse leakage current. In this case, there is an urgent requirement for a Schottky contact material with better thermal stability and lower leakage current.

In addition, it is necessary to investigate the temperature characteristics of GaN-based SBDs. And based on its temperature sensitivity research, it is also necessary to explore

the application in temperature sensors. Moreover, the temperature sensor on GaN is not investigated extensively.

#### §1.4. Outline of thesis

This thesis reports on the Synthesis and Application of NiN for GaN Electron Devices. This thesis is divided into four parts:

In chapter 2, Nickel nitride ( $\text{Ni}_x\text{N}$ ) films were deposited by magnetron reactive sputtering under varying  $\text{N}_2$  partial pressure ( $P(\text{N}_2)$ ) conditions range from 0.005 to 0.184 Pa. With the increasing  $P(\text{N}_2)$ , the deposition rate decreases while the resistivity and root mean square roughness increases. X-ray diffraction (XRD) and X-ray photoelectron spectra (XPS) indicated that  $\text{Ni}_4\text{N}$  and  $\text{Ni}_3\text{N}$  phases dominate the films at low and medium  $P(\text{N}_2)$ , respectively. In addition,  $\text{Ni}_2\text{N}$  phase could be also obtained at high  $P(\text{N}_2)$ . The Ni/N ratio evaluated from the energy dispersive X-ray spectrum is consistent with the  $\text{Ni}_x\text{N}$  phases showed in the XRD spectra of different  $P(\text{N}_2)$ .

In chapter 3,  $\text{Ni}_x\text{N}$  films which prepared by magnetron reactive sputtering at different pressure ratios of Ar and  $\text{N}_2$  mixture gas, were employed as anode material for GaN SBD application. Compared with the GaN diodes with Ni anode, the SBH and turn-on voltage of the SBDs with  $\text{Ni}_x\text{N}$  anode are increased with 0.03~0.18 eV and 0.03~0.15 V, respectively. Capacitance-voltage ( $C-V$ ) curves demonstrate that good interface quality with no obvious hysteresis is realized.  $\text{Ni}_3\text{N}$  anode diodes obtained at medium  $P(\text{N}_2)$  possess a high barrier height and a low reverse leakage current are regarded as a promising anode material. In addition, The temperature-dependent current-voltage ( $I-V-T$ ) characteristics demonstrate that the NiN-SBDs have better thermal stability than that of Ni-SBDs, owing to the suppression of interface reaction between Ni and GaN.

In chapter 4, p-NiO/n-GaN pn diodes and TiN/GaN SBDs were investigated extensively by varying the device diameter and current level. For the NiO/GaN pn diode, it is demonstrated that the series resistance and ideality factor dominate the sensitivity at the fully-turn-on state. However, the series resistance weakly influences the sensitivity of the TiN/GaN SBDs temperature sensor at the fully-turn-on state. After subtracting the component of series resistance, the sensitivity decreases and increases with the increased

device diameters for the p-NiO/n-GaN pn diodes and TiN/GaN SBDs temperature sensors, respectively. A maximum sensitivity of 2.58 mV/K is achieved for the p-NiO/n-GaN pn diodes with a diameter of 100  $\mu\text{m}$  at 20 mA. While, a maximum sensitivity of 1.22 mV/K is achieved from the 300  $\mu\text{m}$  diameter device at the given current of 20 mA for the TiN/GaN SBDs temperature sensors.

For both type temperature sensors, in the sub-threshold state, a good linear relationship between sensitivity and the corresponding current density have been observed for devices with different diameters. A low current density is corresponding to the high sensitivity. The NiO/GaN pn diodes and TiN/GaN SBD presenting good thermal stability and linearity from 25 to 200  $^{\circ}\text{C}$  are promising candidates for temperature sensing application. Moreover, The leakage current in the reverse bias region versus temperature ( $S_{\text{In}}$ ) of the TiN/GaN SBD also presents a sensitivity of approximately 48 mA/K and shows weak dependence on the diameter and bias voltage.

We also investigated the NiN/GaN SBD for temperature sensor application. While in the sub-threshold region, a good linear relationship between sensitivity and the corresponding current density have been observed for a 200 $\mu\text{m}$  diameter NiN/GaN SBD temperature sensor. A low current density is corresponding to the high sensitivity. Based on those result, it demonstrates that the sensitivity of a Schottky barrier diode is correlated with the current density ( $I_D/A$ ). Finally, the theoretical sensitivity of GaN-based SBD temperature sensor is calculated by the TE model. By comparing with TiN, Ni and NiN electrode GaN SBD temperature sensor, the NiN electrode device shows a near-ideal sensitivity of a GaN SBD temperature sensor.

In chapter 5, we fabricated NiN-gated AlGaIn/GaN HFETs by magnetron reactive sputtering with a Ni target in an ambient Ar and N<sub>2</sub> mixture gas. Gate leakage current characteristics shows that the reverse leakage current of NiN-gated HFETs is approximately reduced by one order of magnitude and the ON/OFF drain current ratio increases two order of magnitudes comparing with the conventional Ni-gated HFETs. The temperature-dependent gate leakage current-voltage characteristics demonstrate that the NiN-gated HFETs have better thermal stability.

The conclusions of the dissertation and the future plans to improve the performance of the devices are given in Chapter 6.



## §1.5. References

- [1] Lu X, Wang P, Niyato D, et al. Wireless charging technologies: Fundamentals, standards, and network applications[J]. IEEE Communications Surveys & Tutorials, 2015, 18(2): 1413-1452.
- [2] Kurs A, Karalis A, Moffatt R, et al. Wireless power transfer via strongly coupled magnetic resonances[J]. science, 2007, 317(5834): 83-86.
- [3] Ho S L, Wang J, Fu W N, et al. A comparative study between novel witrlicity and traditional inductive magnetic coupling in wireless charging[J]. IEEE Transactions on Magnetics, 2011, 47(5): 1522-1525.
- [4] Kline M, Izyumin I, Boser B, et al. Capacitive power transfer for contactless charging[C]//2011 Twenty-Sixth Annual IEEE Applied Power Electronics Conference and Exposition (APEC). IEEE, 2011: 1398-1404..
- [5] Popovic Z. Cut the cord: Low-power far-field wireless powering[J]. IEEE Microwave Magazine, 2013, 14(2): 55-62.
- [6] Wei X, Wang Z, Dai H. A critical review of wireless power transfer via strongly coupled magnetic resonances[J]. Energies, 2014, 7(7): 4316-4341.
- [7] Pantic Z, Lukic S M. Framework and topology for active tuning of parallel compensated receivers in power transfer systems[J]. IEEE Transactions on Power Electronics, 2012, 27(11): 4503-4513.
- [8] Wang C S, Covic G A, Stielau O H. Power transfer capability and bifurcation phenomena of loosely coupled inductive power transfer systems[J]. IEEE transactions on industrial electronics, 2004, 51(1): 148-157.
- [9] Wu H H, Gilchrist A, Sealy K D, et al. A high efficiency 5 kW inductive charger for EVs using dual side control[J]. IEEE Transactions on Industrial Informatics, 2012, 8(3): 585-595.
- [10] Jadidian J, Katabi D. Magnetic MIMO: How to charge your phone in your pocket[C]//Proceedings of the 20th annual international conference on Mobile computing and networking. ACM, 2014: 495-506.
- [11] Karalis A, Joannopoulos J D, Soljačić M. Efficient wireless non-radiative mid-range energy transfer[J]. Annals of physics, 2008, 323(1): 34-48.

- [12] Li X, Tsui C Y, Ki W H. A 13.56 MHz wireless power transfer system with reconfigurable resonant regulating rectifier and wireless power control for implantable medical devices[J]. *IEEE Journal of Solid-State Circuits*, 2015, 50(4): 978-989.
- [13] Cannon B L, Hoburg J F, Stancil D D, et al. Magnetic resonant coupling as a potential means for wireless power transfer to multiple small receivers[C]. *Institute of Electrical and Electronics Engineers*, 2009.
- [14] Choi J, Ryu Y H, Kim D, et al. Design of high efficiency wireless charging pad based on magnetic resonance coupling[C]//2012 9th European Radar Conference. *IEEE*, 2012: 590-593.
- [15] Kurs A, Moffatt R, Soljačić M. Simultaneous mid-range power transfer to multiple devices[J]. *Applied Physics Letters*, 2010, 96(4): 044102.
- [16] Li S, Mi C C. Wireless power transfer for electric vehicle applications[J]. *IEEE journal of emerging and selected topics in power electronics*, 2014, 3(1): 4-17.
- [17] Kim Y G, Lim Y, Yun S, et al. Mutual coupling analysis of antennas in layered media through equivalent sources for wireless power transfer[C]//2014 USNC-URSI Radio Science Meeting (Joint with AP-S Symposium). *IEEE*, 2014: 115-115.
- [18] Lu X, Wang P, Niyato D, et al. Dynamic spectrum access in cognitive radio networks with RF energy harvesting[J]. *IEEE Wireless Communications*, 2014, 21(3): 102-110.
- [19] Lu X, Wang P, Niyato D, et al. Resource allocation in wireless networks with RF energy harvesting and transfer[J]. *IEEE Network*, 2015, 29(6): 68-75.
- [20] Ladan S, Ghassemi N, Ghiotto A, et al. Highly efficient compact rectenna for wireless energy harvesting application[J]. *IEEE microwave magazine*, 2013, 14(1): 117-122.
- [21] Xie L, Shi Y, Hou Y T, et al. Wireless power transfer and applications to sensor networks[J]. *IEEE Wireless Communications*, 2013, 20(4): 140-145.
- [22] McSpadden J O, Mankins J C. Space solar power programs and microwave wireless power transmission technology[J]. *IEEE microwave magazine*, 2002, 3(4): 46-57.
- [23] Miller J M, Onar O C, Chinthavali M. Primary-side power flow control of wireless power transfer for electric vehicle charging[J]. *IEEE Journal of Emerging and Selected Topics in Power Electronics*, 2014, 3(1): 147-162.
- [24] Etinger A, Pilosof M, Litvak B, et al. Characterization of a Schottky diode rectenna for millimeter wave power beaming using high power radiation sources[J]. *Acta Physica*

Polonica A, 2017, 131(5): 1280-1284.

[25] Saitoh Y, Sumiyoshi K, Okada M, et al. Extremely low on-resistance and high breakdown voltage observed in vertical GaN Schottky barrier diodes with high-mobility drift layers on low-dislocation-density GaN substrates[J]. Applied Physics Express, 2010, 3(8): 081001.

[26] Riordan M, Hoddeson L, Herring C. The invention of the transistor[M]//More Things in Heaven and Earth. Springer, New York, NY, 1999: 563-578.

[27] SEIDENBERG P. From Germanium to Silicon, A History of Change in the Technology of the Semiconductors[J]. Facets: New Perspectives on the History of Semiconductors, 1997: 36-74.

[28] Baker R J. CMOS: circuit design, layout, and simulation[M]. Wiley-IEEE press, 2019.

[29] 陈治明, 陈守智. 宽禁带半导体电力电子器件及其应用[M]. 机械工业出版社, 2009. (In Chinese)

[30] 郝跃, 张金凤, 张进成. 氮化物宽禁带半导体材料与电子器件[J]. 科学出版社, 2013. (In Chinese)

[31] HOLT D B, YACOBI B G. Extended Defects in Semiconductors[M]. Cambridge: Cambridge University Press, 2007.

[32] Jang H W, Lee J H, Lee J L. Characterization of band bendings on Ga-face and N-face GaN films grown by metalorganic chemical-vapor deposition[J]. Applied physics letters, 2002, 80(21): 3955-3957.

[33] Dimitrov R, Murphy M, Smart J, et al. Two-dimensional electron gases in Ga-face and N-face AlGa<sub>N</sub>/Ga<sub>N</sub> heterostructures grown by plasma-induced molecular beam epitaxy and metalorganic chemical vapor deposition on sapphire[J]. Journal of Applied Physics, 2000, 87(7): 3375-3380.

[34] Pu T F, Li X B, Wang X, et al. GaN Schottky Barrier Diodes with TiN Electrode for Microwave Power Transmission[C]//Materials Science Forum. Trans Tech Publications Ltd, 2019, 954: 126-132.

[35] Sze S M, Ng K K. Physics of semiconductor devices[M]. John wiley & sons, 2006.

[36] Schmitz A C, Ping A T, Khan M A, et al. High temperature characteristics of Pd Schottky contacts on n-type GaN[J]. Electronics letters, 1996, 32(19): 1832-1833.

- [37] Guo J D, Pan F M, Feng M S, et al. Schottky contact and the thermal stability of Ni on n - type GaN[J]. *Journal of applied physics*, 1996, 80(3): 1623-1627.
- [38] Wang J, Zhao D G, Sun Y P, et al. Thermal annealing behaviour of Pt on n-GaN Schottky contacts[J]. *Journal of Physics D: Applied Physics*, 2003, 36(8): 1018.
- [39] Dobos L, Pécz B, Tóth L, et al. Structural and electrical properties of Au and Ti/Au contacts to n-type GaN[J]. *Vacuum*, 2008, 82(8): 794-798.
- [40] Zhang B J, Egawa T, Zhao G Y, et al. Schottky diodes of Ni/Au on n-GaN grown on sapphire and SiC substrates[J]. *Applied Physics Letters*, 2001, 79(16): 2567-2569.)
- [41] Kumar A, Vinayak S, Singh R. Micro-structural and temperature dependent electrical characterization of Ni/GaN Schottky barrier diodes[J]. *Current Applied Physics*, 2013, 13(6): 1137-1142.
- [42] Gu H, Hu C, Wang J, et al. Vertical GaN Schottky barrier diodes on Ge-doped free-standing GaN substrates[J]. *Journal of Alloys and Compounds*, 2019, 780: 476-481.
- [43] Ren B, Liao M, Sumiya M, et al. Nearly ideal vertical GaN Schottky barrier diodes with ultralow turn-on voltage and on-resistance[J]. *Applied Physics Express*, 2017, 10(5): 051001.
- [44] Koné S, Cayrel F, Yvon A, et al. DLTS analysis of high resistive edge termination technique - induced defects in GaN - based Schottky barrier diodes[J]. *physica status solidi (a)*, 2016, 213(9): 2364-2370.
- [45] Li L, Wang X, Liu Y, et al. NiO/GaN heterojunction diode deposited through magnetron reactive sputtering[J]. *Journal of Vacuum Science & Technology A: Vacuum, Surfaces, and Films*, 2016, 34(2): 02D104.
- [46] Ao J P, Suzuki A, Sawada K, et al. Schottky contacts of refractory metal nitrides on gallium nitride using reactive sputtering[J]. *Vacuum*, 2010, 84(12): 1439-1443.
- [47] Ao J P, Naoi Y, Ohno Y. Thermally stable TiN Schottky contact on AlGaIn/GaN heterostructure[J]. *Vacuum*, 2013, 87: 150-154.
- [48] Li L, Kishi A, Shiraishi T, et al. Electrical properties of TiN on gallium nitride grown using different deposition conditions and annealing[J]. *Journal of Vacuum Science & Technology A: Vacuum, Surfaces, and Films*, 2014, 32(2): 02B116.
- [49] Krasnov V A, Shutov S V, Yerochin S Y, et al. High Temperature Operation Limit Assessment for 4H-SiC Schottky Diode-Based Extreme Temperature Sensors[J]. *IEEE*

Sensors Journal, 2018, 19(5): 1640-1644.

[50] Kumar V, Maan A S, Akhtar J. Barrier height inhomogeneities induced anomaly in thermal sensitivity of Ni/4H-SiC Schottky diode temperature sensor[J]. Journal of Vacuum Science & Technology B, Nanotechnology and Microelectronics: Materials, Processing, Measurement, and Phenomena, 2014, 32(4): 041203.

[51] Zhang X, Jin DM, Liu LT 2014 Transd[J]. Microsys. Technol, 2014, 3(1).

[52] Rue B, Flandre D 2007 Proceedings 2007 IEEE International SOI Conference Indian Wells, CA, USA, Oct 1–4, 2007 p111

[53] de Souza M, Rue B, Flandre D, Pavanello M A 2009 Proceedings 2009 IEEE International SOI Conference Foster City, CA, USA, Oct 5–8, 2009 p1

[54] Xi Y, Schubert E F. Junction–temperature measurement in GaN ultraviolet light-emitting diodes using diode forward voltage method[J]. Applied Physics Letters, 2004, 85(12): 2163-2165.

[55] Krasnov V A, Shutov S V, Yerochin S Y, et al. High temperature diode sensors based on InGaN/AlGaN structures[J]. Journal of Vacuum Science & Technology B, Nanotechnology and Microelectronics: Materials, Processing, Measurement, and Phenomena, 2018, 36(2): 022905.

[56] Kwan A M H, Guan Y, Liu X, et al. Integrated over-temperature protection circuit for GaN smart power ICs[J]. Japanese Journal of Applied Physics, 2013, 52(8S): 08JN15.

[57] Kwan A M H, Guan Y, Liu X, et al. A highly linear integrated temperature sensor on a GaN smart power IC platform[J]. IEEE Transactions on Electron Devices, 2014, 61(8): 2970-2976.

[58] Madhusoodhanan S, Sandoval S, Zhao Y, et al. A highly linear temperature sensor using GaN-on-SiC heterojunction diode for high power applications[J]. IEEE Electron Device Letters, 2017, 38(8): 1105-1108.

[59] Kumar V, Maan A S, Akhtar J. Barrier height inhomogeneities induced anomaly in thermal sensitivity of Ni/4H-SiC Schottky diode temperature sensor[J]. Journal of Vacuum Science & Technology B, Nanotechnology and Microelectronics: Materials, Processing, Measurement, and Phenomena, 2014, 32(4): 041203.

[60] Chandrashekar M V S, Duggirala R, Spencer M G, et al. 4 H SiC betavoltaic powered temperature transducer[J]. Applied Physics Letters, 2007, 91(5): 053511.

[61] Pristavu G, Brezeanu G, Badila M, et al. A model to non-uniform Ni Schottky contact

on SiC annealed at elevated temperatures[J]. Applied Physics Letters, 2015, 106(26): 261605.

[62] Rao S, Pangallo G, Di Benedetto L, et al. A V2O5/4H-SiC Schottky diode-based PTAT sensor operating in a wide range of bias currents[J]. Sensors and Actuators A: Physical, 2018, 269: 171-174.

[63] Wang X L, Wang C M, Hu G X, et al. Improved DC and RF performance of AlGa<sub>N</sub>/Ga<sub>N</sub> HEMTs grown by MOCVD on sapphire substrates[J]. Solid-state electronics, 2005, 49(8): 1387-1390.

[64] Rajan S, Waltereit P, Poblenz C, et al. Power performance of AlGa<sub>N</sub>-Ga<sub>N</sub> HEMTs grown on SiC by plasma-assisted MBE[J]. IEEE Electron Device Letters, 2004, 25(5): 247-249.

[65] Hsu L, Walukiewicz W. Effect of polarization fields on transport properties in AlGa<sub>N</sub>/Ga<sub>N</sub> heterostructures[J]. Journal of Applied Physics, 2001, 89(3): 1783-1789.

[66] Li L, Kishi A, Liu Q, et al. Ga<sub>N</sub> Schottky barrier diode with TiN electrode for microwave rectification[J]. IEEE Journal of the Electron Devices Society, 2014, 2(6): 168-173.

## Chapter 2: Synthesis and Characteristics of Nickel Nitride

### §2.1. Introduction

Metal nitrides have the advantages of easy preparation, corrosion-resistance, chemical and thermal stability, and excellent catalytic activity [1-5], which are widely used in the fields of energy storage (super-capacitors and lithium-ion batteries) [6], electrochemical water oxidation [7], resistive random access memory cells [8], and electronic devices [9-12]. In our previous study, metal nitrides demonstrated good Schottky contact characteristics as well as good thermal stability on GaN, showing great potential for harsh environment applications [9, 11, 12]. Among those materials, TiN-anode GaN SBD with low turn-on voltage to breakdown voltage ratio is also attractive to develop microwave power rectification circuits [12]. However, the GaN SBDs with TiN electrodes have a problem that the reverse leakage current was relatively high as compared with the Ni electrodes GaN SBDs.

Nickel nitrides ( $\text{Ni}_x\text{N}$ ) are important metallic materials that have been widely used in many areas [3, 6, 8, 13]. It is reported that  $\text{Ni}_x\text{N}$  can avoid interface reaction between anode and GaN, and possesses a high work function [13], showing the potential to serve as the SBD anode to reduce leakage current. However,  $\text{Ni}_x\text{N}$  films synthesized by chemical vapor deposition, sputtering and highly reactive azides or hydrazine [13-16] present different phases, such as  $\text{Ni}_4\text{N}$ ,  $\text{Ni}_3\text{N}$ , and  $\text{Ni}_2\text{N}$ . Among those methods, sputtering is the much more suitable technique to obtain necessary phase by simply adjusting the pressure ratio of Ar and  $\text{N}_2$ .

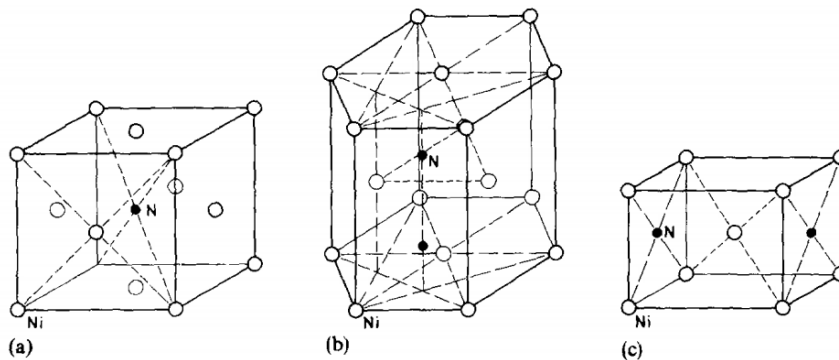


Fig. 2-1. Interstitial positions, partially occupied by nitrogen atoms, in (a)  $\text{Ni}_4\text{N}$ , (b)  $\text{Ni}_3\text{N}$  and (c)  $\text{Ni}_2\text{N}$ . [14]

Fig. 2-1 shows the crystal structures of (a) Ni<sub>4</sub>N, (b) Ni<sub>3</sub>N and (c) Ni<sub>2</sub>N. [14] The crystal structures of Ni<sub>4</sub>N, Ni<sub>3</sub>N and Ni<sub>2</sub>N are face-centered cubic (fcc), hexagonal close packed (hcp) and body-centered cubic (bcc), respectively. Among them, Ni<sub>3</sub>N and Ni<sub>2</sub>N are relatively stable in the room temperature.

In this chapter, Ni<sub>x</sub>N films were prepared by magnetron reactive sputtering at different pressure ratios of Ar and N<sub>2</sub> mixture gas. With the increasing P(N<sub>2</sub>), the deposition rate decreases while the resistivity and root mean square roughness (RMS) increase. XRD and XPS indicate that Ni<sub>4</sub>N and Ni<sub>3</sub>N phases dominate the films at low and medium P(N<sub>2</sub>), respectively. In addition, Ni<sub>2</sub>N phase can be also obtained at high P(N<sub>2</sub>). The Ni/N ratio evaluated from the energy dispersive X-ray spectrum is consistent with the Ni<sub>x</sub>N phases showed in the XRD spectra of different P(N<sub>2</sub>).

## §2.2. Synthesis of Ni<sub>x</sub>N films at room temperature

### §2.2.1. Reactive sputtering technology

Reactive sputtering is a process that allows compounds to be deposited by introducing a reactive gas (typically O<sub>2</sub> or N<sub>2</sub>) into the plasma, which is typically formed by an inert gas such as argon (most common), xenon, or krypton. In this process, the reactive gas is “activated” by the plasma and chemically reacts with the target material which is subsequently deposited on the substrate. Composition control of the resultant film is achievable by controlling the relative amounts of the inert and reactive gases. Oxides, nitrides, carbides and mixtures of all three are typically generated by reactive sputtering. The object of the reactive sputtering process is to create thin films of closely controlled stoichiometry and structure. The reactive sputtering can be divided to be RF mode and DC mode, and the substrate is set at room or high temperature.

Fig. 2-2 shows the reactive magnetron sputtering in this study (left) and schematic of reaction chamber (right). Sputtering technology bombards the target (approximately 10<sup>0</sup> to 10<sup>2</sup> eV) atoms by colliding a certain amount of kinetic energy (approximately 10<sup>2</sup> to 10<sup>3</sup> eV) with high-voltage ions into the target and side of the substrate required by the film Method of forming the required material. Generally, the adhesion is high, and the film stress is larger than that obtained by vapor deposition. Fig. 2-2 shows the magnetron sputtering system used in this thesis. In magnetron sputtering, electrons are confined

around the target by a magnetic field generated by a magnet directly below the target, thus the sputtering amount of the target can be increased and plasma damage to the substrate can be reduced. In this thesis, the distance between the target and the substrate is about 10 cm.

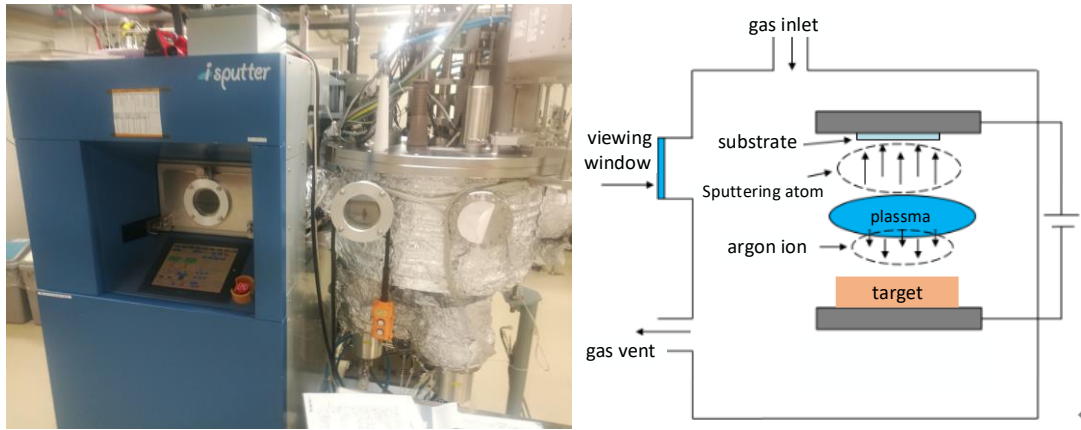


Fig. 2-2. The reactive magnetron sputtering in this study (left) and schematic of reaction chamber (right).

### §2.2.2. Deposition of $Ni_xN$ film

In this thesis, all the  $Ni_xN$  films were formed on (100) Si or sapphire substrates at the room temperature by reactive magnetron sputtering with RF model. Pure Ni target (99.99%) was reactively sputtered in an Ar and  $N_2$  mixture ambient. The deposition processes of  $Ni_xN$  films are shown in Fig. 2-3.

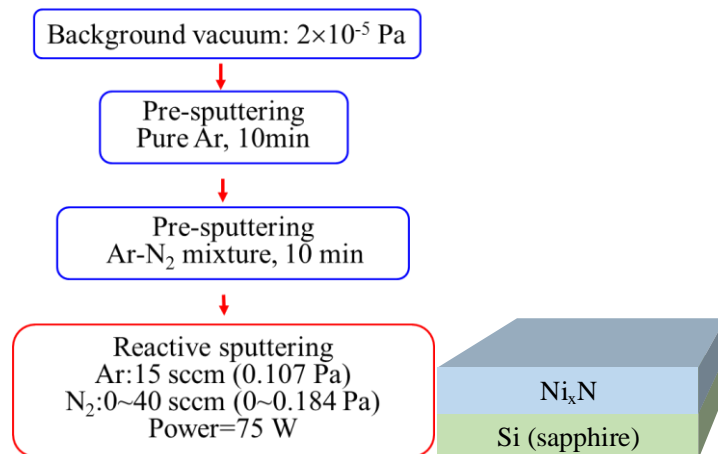


Fig. 2-3. The deposition process (left) and schematic (right) of  $Ni_xN$  film on Si or sapphire substrate.

Before the films sputtering, we clean the substrates by using acetone and pure water to remove the organic impurities. The chamber background vacuum is kept below  $2 \times 10^{-5}$  Pa.

The next step is 10 min pre-sputtering to clean the surface of the Ni target. In this step, the power is kept at 150 W, the gas is Ar with a flow rate of 30 sccm.

Then, changing the power to 75 W, and Ar flow rate to 15 sccm which converted into Ar partial pressure is 0.107 Pa. While the N<sub>2</sub> is inlet the reaction chamber with a flow rate varied from 1 to 40 sccm which converted into P(N<sub>2</sub>) are varied from 0.005 to 0.18 Pa (0.005, 0.014, 0.023, 0.046, 0.069, 0.115 and 0.184 Pa). This step is to stabilize the reaction chamber environment.

Finally, keeping the conditions of the previous step and sputtering the Ni<sub>x</sub>N and Ni films. The depiction times are 4800, 4800, 4800, 4900, 5400, 6000, 6000, and 6000 s for the P(N<sub>2</sub>) of 0, 0.005, 0.014, 0.023, 0.046, 0.069, 0.115 and 0.184 Pa, respectively.

The thickness of the Ni<sub>x</sub>N films are obtained from the average value of 5 points in the different areas by using profile-system.

Table 2-1. Deposition conditions of Ni<sub>x</sub>N films with different flow rates.

Flow rate /sccm		Partial pressure/Pa		P(N <sub>2</sub> )/ (P(N <sub>2</sub> )+P(Ar))	Time/s	Thickness/nm (measured)
Ar	N <sub>2</sub>	Ar	N <sub>2</sub>			
	0		0.000	0.00	4800	200
	1		0.005	0.04	4800	181
	3		0.014	0.11	4800	198
15	5	0.107	0.023	0.18	4900	185
	10		0.046	0.30	5400	184
	15		0.069	0.39	6000	189
	25		0.115	0.52	6000	173
	40		0.184	0.63	6000	150

## §2.3. Characteristics of Ni<sub>x</sub>N films at room temperature

### §2.3.1. Deposition rate and resistivity of Ni<sub>x</sub>N films

The deposition rate (calculated by thickness divide growth time) versus the  $P(N_2)$  is shown in the Fig. 2-4. The deposition rate is 2.4 nm/min for Ni film sputtered in the pure Ar ambient environment. With the  $P(N_2)$  increasing, the deposition rate decrease slowly to around 1.5 nm/min. The introduced nitrogen will nitridize the target surface and decrease the sputtering yield, resulting in the decrease of sputtering rate.

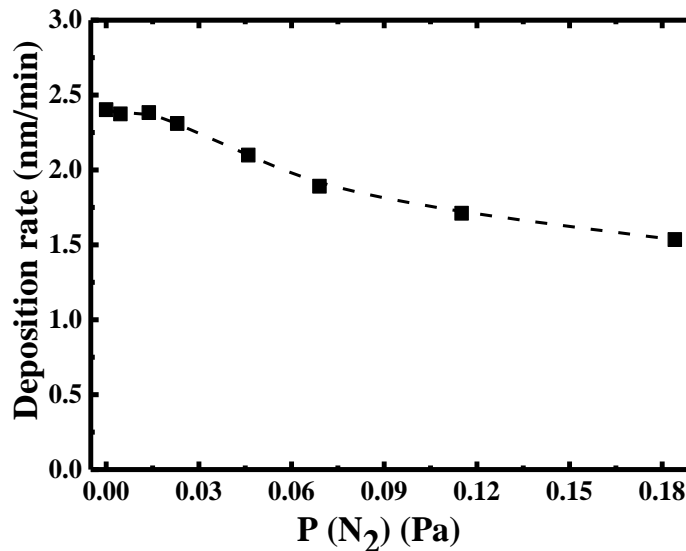


Fig. 2-4. Deposition rate of the  $Ni_xN$  films deposited at different  $P(N_2)$ .

The measurement resistivity method mainly includes transmission line mode (TLM), Hall and four-probe method. In this thesis, four-probe method was selected to measure the  $Ni_xN$  films resistivities by using a bridge structure current which is shown in Fig. 2-5. In order to accurately measure the resistivity of  $Ni_xN$ , the  $Ni_xN$  film was deposited on the sapphire substrate. The process was following the standard photolithography technology. Firstly, sapphire substrates were cleaned by using acetone and pure water. Secondly, realizing the pattern of bridge circuit on sapphire substrate by photolithography development technology. Then, sputtering  $Ni_xN$  films with different  $P(N_2)$ . Finally, removing  $Ni_xN$  films other than bridge structure patterns by lift-off technology.

As shown in the Fig. 2-6 (a), the line width ( $W$ ) of the bridge structure is set to 3, 6, 9, 12, and 15  $\mu m$  and the line length ( $L$ ) is set to 400  $\mu m$ . In the Fig. 2-6 (b), a constant current is supplied by two probes (from electrode 1 and 4) and a second set of probes are used to measure the voltage drop (from electrode 2 and 3). The total resistance is given by

$$R = \frac{V_{23}}{I_{14}} = \rho_s \frac{L}{W} \quad (2-1)$$

where  $V_{23}=V_2-V_3$ ,  $I_{14}$  is the current flowing from contact 1 to contact 4,  $\rho_s$  the sheet resistance,  $L$  the length,  $W$  the width.

To minimize the stander error, we designed a series of width ( $W=3, 6, 9, 12$  and  $15 \mu\text{m}$ ), then

$$R = \rho_s \frac{L}{W + \Delta W} \quad (2-2)$$

where,  $\Delta W$  is the line width error fromed by the fabrication process. Then, merge equation (2-1) and (2-2).

$$\frac{1}{R} = \frac{1}{\rho_s L} (W + \Delta W) = \frac{W}{\rho_s L} + \frac{\Delta W}{\rho_s L} \quad (2-3)$$

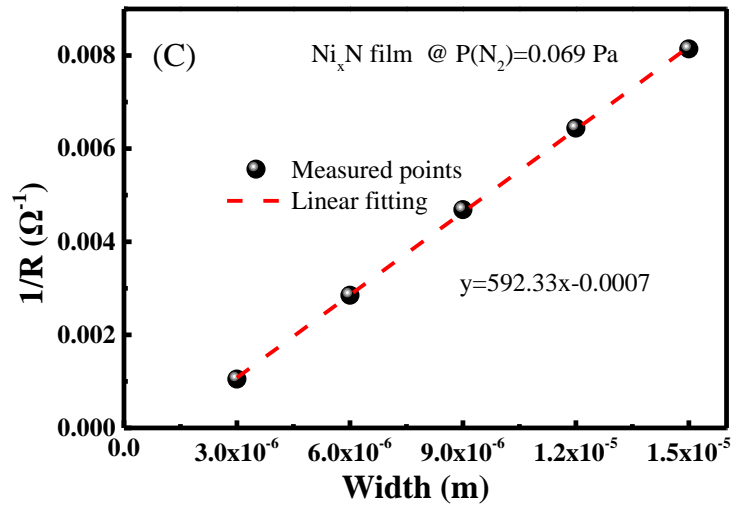
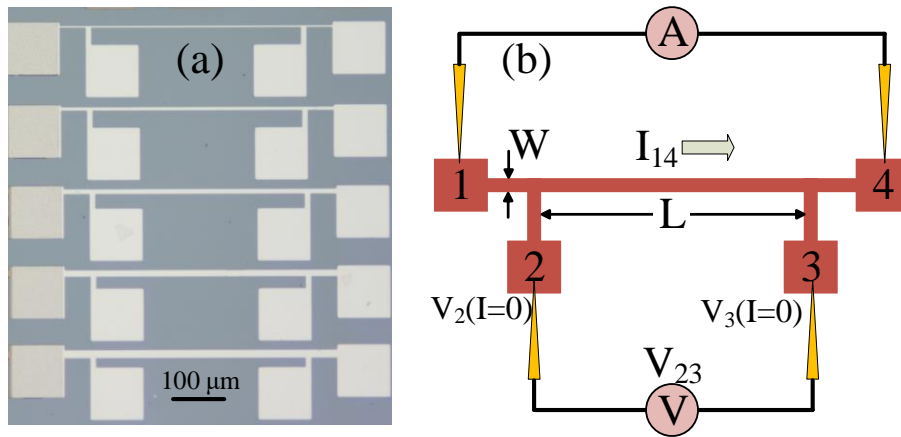


Fig. 2-5. (a) Optical image of Ni<sub>x</sub>N bridge structures, the W is 3, 6, 9, 12, and 15 μm from top to bottom, (b) a bridge sheet resistance test structure, (c) a example of calculating Ni<sub>x</sub>N film resistivity (@ 0.069 Pa) .

From the slope of the  $\frac{1}{R} \sim W$  plotting (Fig. 2-5 (c)), we can deduce the  $\rho_s$  and the buck resistance by multiply the  $\rho_s$  with the thickness of the film ( $t$ ).

The resistivity values of the Ni<sub>x</sub>N films deposited with different P(N<sub>2</sub>) are shown in Fig.2-6. The resistivity of the pure Ni film is approximately 8.9 μΩcm, which is slightly higher than that of the bulk Ni (6.9 μΩcm) due to the existence of grain boundary and impurity. As the P(N<sub>2</sub>) increasing, the resistivity increased first and then saturated at a value of approximately 110 μΩcm, which is very closed to that of Ni<sub>x</sub>N film reported by other groups. [16-18 ]

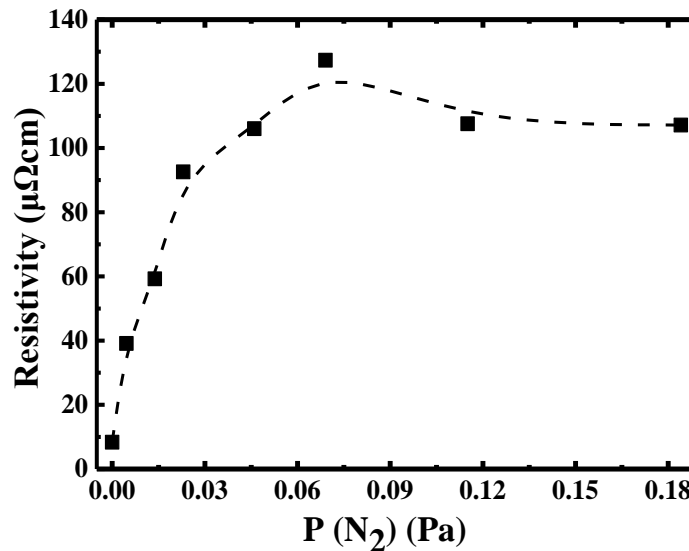


Fig. 2-6. Resistivity of the Ni<sub>x</sub>N films deposited at different P(N<sub>2</sub>).

### §2.3.2. The phases of Ni<sub>x</sub>N films

The XRD is used to measure the crystal internal structure. The X-rays are irradiated on the crystal lattice, and diffraction occurs, then the internal structure of the crystal is analyzed by analyzing the diffraction pattern [19]. In this thesis, the phase identification of deposited films were performed by XRD analysis using a Siemens D500 diffractometer

supplied with software Diffracplus with Ni-filtered Cu K $\alpha$  radiation and a scanning speed of 0.022u/s. The phases were identified according to the JCPDS-ICDD-PDF data base. [20]

The patterns of the Ni<sub>x</sub>N films deposited on Si substrates are given in Fig. 2-7. In Fig. 2-7 (a), there are six curves from the bottom to the top corresponding to the JCPDS 10-0280 (Ni), JCPDS 36-1300 (Ni<sub>4</sub>N), and Ni<sub>x</sub>N film at P(N<sub>2</sub>) of 0, 0.005, 0.014 and 0.023 Pa, respectively. For the Ni film, two peaks are generally observed at 44.5° and 51.8°, which are assigned to the (111) and (200) patterns of Ni, respectively. The Ni (111) and (200) peaks of Ni<sub>x</sub>N film with P(N<sub>2</sub>) of 0.005 Pa shift to a lower diffraction due to the nitrogen incorporation.[18] In addition, the increase in the resistivity also identifies the nitrogen incorporation. When the P(N<sub>2</sub>) increases to 0.014 and 0.023 Pa, the nitrogen incorporation is much more stronger, and the peak at 50.5° is identified to be Ni<sub>4</sub>N (200) peak. Meanwhile, the intensity of the Ni (111) pick is so weak that it is not easy to be identified. Therefore, the Ni metal has been transformed into Ni<sub>4</sub>N-dominated phase with a relatively low P(N<sub>2</sub>).

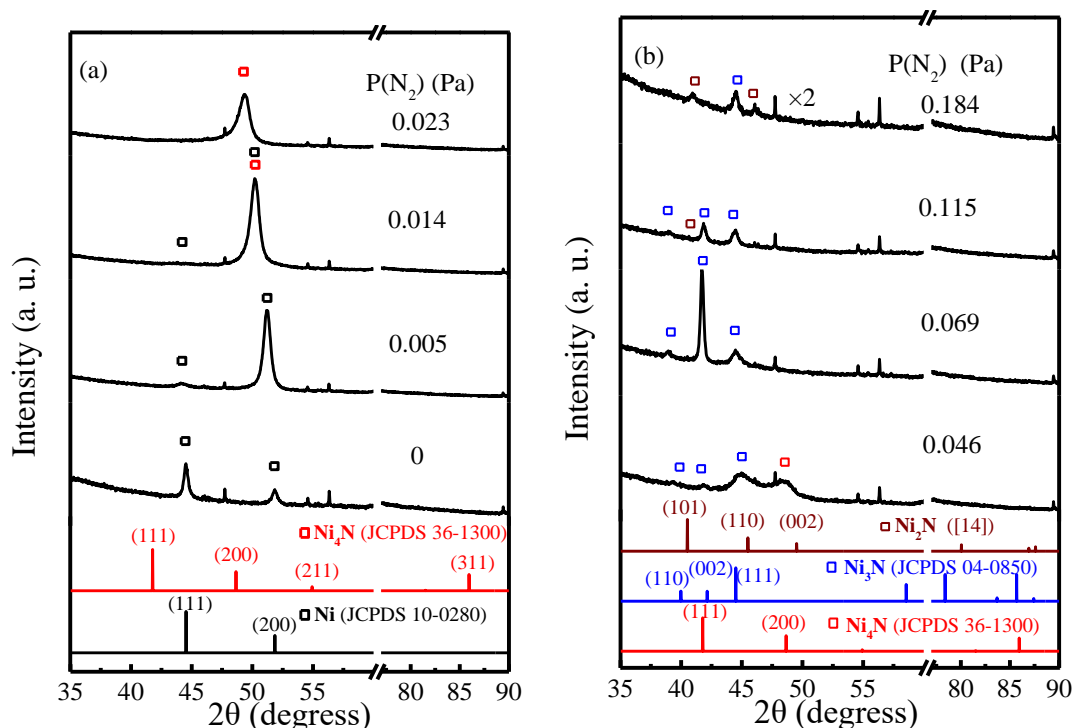


Fig. 2-7. XRD patterns of Ni<sub>x</sub>N elaborated at different P(N<sub>2</sub>), (a) in the low regime (0, 0.005, 0.014 and 0.023 Pa), (b) in the medium and high regime (0.046, 0.069, 0.115 and 0.184 Pa).

Fig. 2-7 (b) shows the XRD patterns of the  $Ni_xN$  films at low  $P(N_2)$  (0.046, 0.069, 0.115 and 0.184 Pa) as well as  $Ni_4N$  (JCPDS 36-1300),  $Ni_3N$  (JCPDS 10-0280) and  $Ni_2N$  [14] patterns. The curves of the medium  $P(N_2)$  (0.46 and 0.069 Pa) were dominated by the peaks at around  $39^\circ$ ,  $42.1^\circ$  and  $44.5^\circ$ , which are corresponding to the  $Ni_3N$  (JCPDS 10-0280) patterns. Besides, a peak at  $49^\circ$  is identified to the  $Ni_4N$  (200) peak. While for the  $P(N_2)$  of 0.115 Pa, excepting the  $Ni_3N$  peak, there is an insignificant peak appeared at  $40.5^\circ$  which belongs to the peak of  $Ni_2N$  (101) pattern. When the  $P(N_2)$  increases to 0.184 Pa, the  $Ni_2N$  (101) peak become much visible, and a new peak at  $46^\circ$ , which is identified to be the  $Ni_2N$  (110) peak, appears. None the less, the  $Ni_3N$  (111) peaks at  $44.5^\circ$  could be also distinguished. These mean that there are two  $Ni_xN$  phases presenting in the film with  $P(N_2)$  form 0.115 to 0.184 Pa.

### §2.3.3. The surface morphologies of $Ni_xN$ films

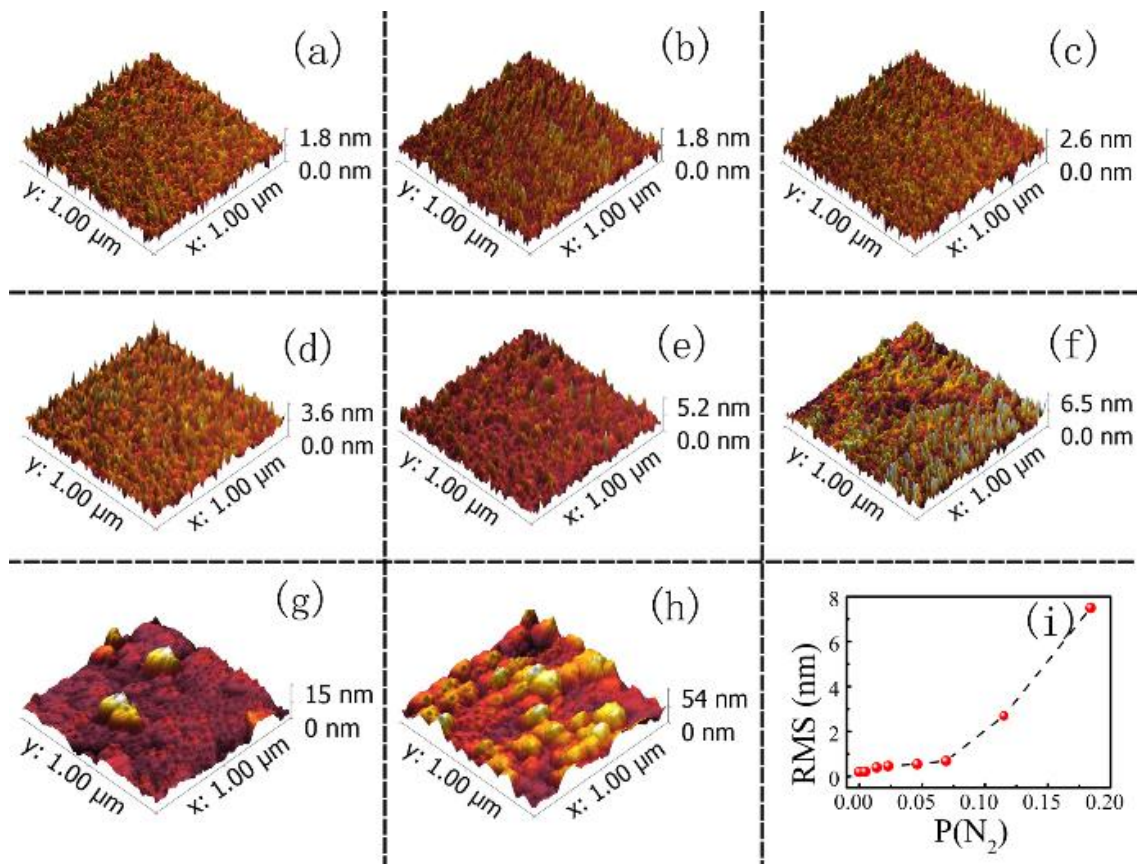


Fig. 2-8. (a)~(h) AFM images ( $1 \mu m \times 1 \mu m$ ) of the Ni and  $Ni_xN$  films deposited with  $P(N_2)$  from 0.005 Pa to 0.184 Pa, (i) RMS roughness of different  $P(N_2)$ .

The surface morphologies of the  $\text{Ni}_x\text{N}$  films at different  $P(\text{N}_2)$  obtained by atomic force microscopy (AFM) are shown in Fig. 2-8 (a-h) and the corresponding root mean square (RMS) roughness are summarized in Fig. 2-8 (i). The surface of the Ni film is very smooth presenting an RMS of 0.20 nm. For the films grown with the  $P(\text{N}_2)$  lower than 0.069 Pa, the surfaces are still smooth with the RMS roughness of 0.22, 0.39, 0.46 and 0.55 nm, respectively. While for the  $\text{Ni}_x\text{N}$  films with the  $P(\text{N}_2)$  of 0.115 and 0.184 Pa, the RMS roughness shows abrupt increase. Observed from Fig. 2-8 (g) and (h),  $\text{Ni}_2\text{N}$  grains are agglomerated to larger mass and increase the surface roughness.

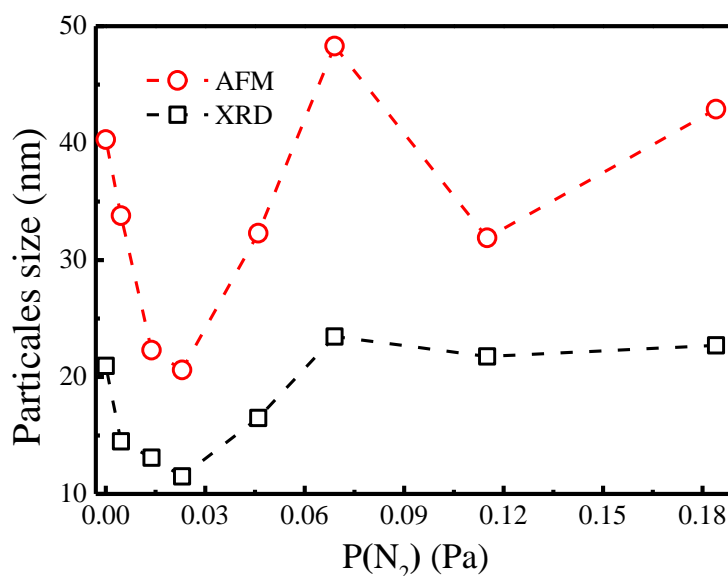


Fig. 2-9. Particle size obtained using XRD and AFM as a function of the  $P(\text{N}_2)$  for  $\text{Ni}_x\text{N}$  films.

The average particle size calculated from XRD using Scherer equation is plotted in comparison with that obtained from atomic force microscope (AFM) (Fig. 2-9). The variation of grain size versus  $P(\text{N}_2)$  shows a similar tendency for the both methods. However, the particle sizes obtain by AFM are larger than that of XRD due to the particle agglomeration in surface.[18] For the Ni film, the particle sizes obtained by XRD and AFM are 21.0 and 40.3 nm, respectively. At low  $P(\text{N}_2)$ , the low deposition ratio can help to enhance the Ni diffusion and form the uniform  $\text{Ni}_4\text{N}$  film with a relatively small grain size. As the  $P(\text{N}_2)$  becomes higher than 0.023 Pa, the well-crystalline  $\text{Ni}_3\text{N}$  phase dominates in the films and the grain size increases.[18] However, further increase  $P(\text{N}_2)$  would cause the degradation of crystalline quality and enhance the formation of  $\text{Ni}_2\text{N}$

phase. Then, the particles size decreased slightly again.

### §2.3.4. The chemical compositions of Ni<sub>x</sub>N films

The chemical composition of the Ni<sub>x</sub>N films obtained at different P(N<sub>2</sub>) was analyzed by XPS system (ULVAC-PHI5000) equipped with a spherical capacitor analyzer and monochromatic Al K $\alpha$  radiation source ( $h\nu=1486.6$  eV). The C1s, with photoelectron binding energy at 284.8 eV, is used for charge correction. The samples were pre-sputtered for 3 min using Ar<sup>+</sup> to eliminate the surface impurities under an acceleration voltage of 1 kV.

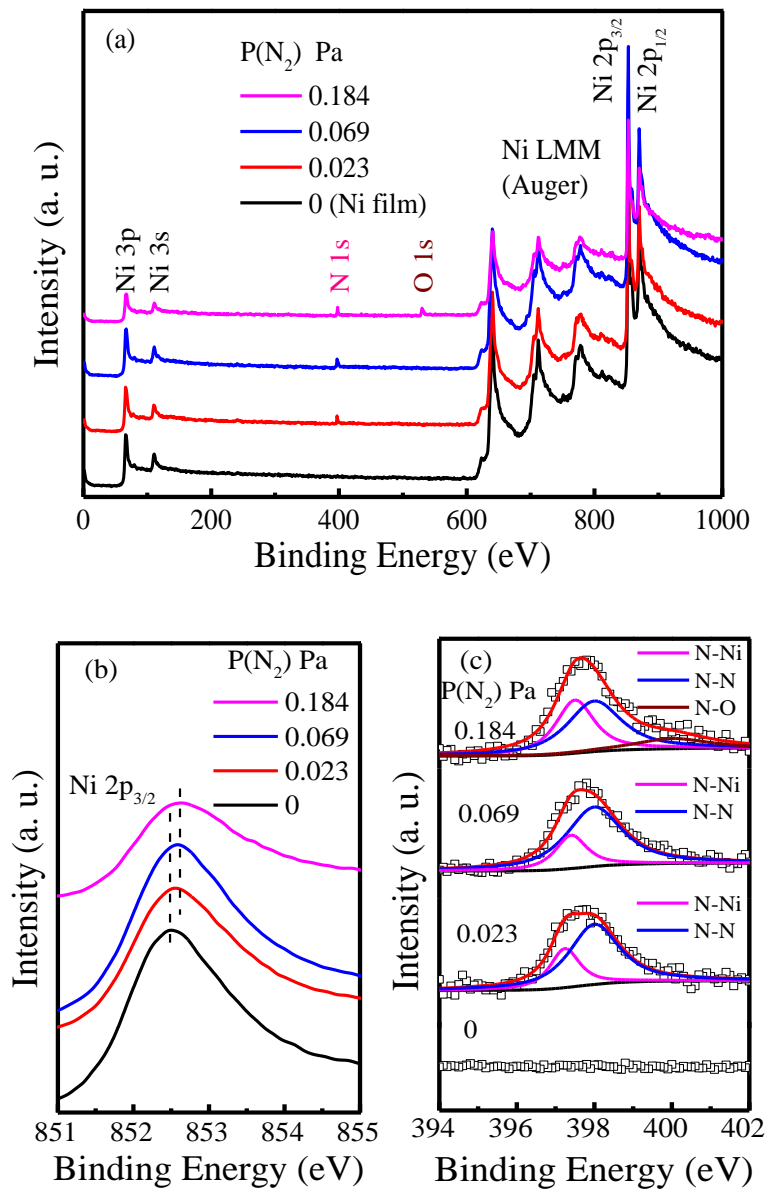


Fig. 2-10. (a) Wide scan range, (b) Ni 2p<sub>3/2</sub>, and (c) N 1s XPS spectra for the Ni<sub>x</sub>N films with P(N<sub>2</sub>) of 0, 0.023, 0.069 and 0.184 Pa.

Fig. 2-10 shows the XPS spectra of the typical Ni<sub>x</sub>N films with P(N<sub>2</sub>) of 0, 0.023, 0.069, and 0.184 Pa. Obviously, only the Ni signal is detected for the Ni film while N signals are showed for other samples (Fig. 2-10(a)). Ni 2p<sub>3/2</sub> peaks of N<sup>0</sup> form Ni films and N<sup>1+</sup> form Ni<sub>x</sub>N with P(N<sub>2</sub>) of 0.023, 0.069 and 0.184 Pa were around 852.4~852.7 eV (Fig. 2-10 (b)), which was in consistent with previous reports.[3, 21-23]

However, these Ni 2p<sub>3/2</sub> peaks have positive shift with the increasing P(N<sub>2</sub>) due to the formation of N-Ni bonds. [3, 24] As shown in Fig.2-5 (c), N 1s peak was clearly shown in the spectra for the Ni<sub>x</sub>N films but not for the Ni film. The peak at 398 eV is N-N bonding, and the Ni-N bonding energy is 397.25, 397.4, and 397.5 eV for Ni<sub>x</sub>N films with P(N<sub>2</sub>) of 0.023, 0.069 and 0.184 Pa, respectively, which correspond to the Ni<sub>4</sub>N, Ni<sub>3</sub>N as well as mixture of Ni<sub>3</sub>N and Ni<sub>2</sub>N. [22] A weak peak at around 400 eV showed in Ni<sub>x</sub>N film with P(N<sub>2</sub>) of 0.184 Pa may originate from the N-O bond, corresponding the O 1s peak in the Fig. 2-10 (a). It worth noting that the peak shift is relatively slight and the obtained films in our experiment are mixture of different phases (confirmed from the XRD results). Therefore, it is very difficult to de-convolute the XPS spectra and obtain the precise composition.

### §2.3.5. The atom proportion of Ni<sub>x</sub>N films

We used XRD and XPS to evaluate phase composition of the Ni<sub>x</sub>N film. XRD curves are effective to determine the different kinds of phases, but it is difficult to determine the exact composition of every Ni<sub>x</sub>N phase in a mix phase sample.

The core level spectra of N1s and Ni2p measured by XPS is also used to further evaluate the composition of Ni<sub>x</sub>N phase. By comparing the binding energies of Ni and Ni<sub>x</sub>N in the literatures, we identify that Ni2p<sub>3/2</sub> peaks positive shifts gradually with the increasing P(N<sub>2</sub>) due to the formation of N-Ni bonds. In addition, N1s peaks located around 397.4 eV of sample with different P(N<sub>2</sub>) are also shown similar tendency. Observed from the XRD results, the obtained films in our experiment are mixture of different phases. However, it is very difficult to de-convolute the XPS spectra and obtain the precise composition.

Therefore, we measure the sample composition and incorporated contamination by the

Co-calibrated EDX (Horiba Emax X-Act: ex-270) using SEM (Hitachi SU1510), and the analysis software is Emax-evolution. The accelerate voltage and sampling time are 15 kV and 50 s, respectively. The  $\text{Ni}_x\text{N}$  samples fabricated for EDX measurement are 500 nm thick  $\text{Ni}_x\text{N}$  layer on the  $6\text{mm}\times 6\text{mm}$  Si substrates. The equipment was calibrated by Co-standard sample before measuring the  $\text{Ni}_x\text{N}$  samples. The composition of N, Ni, O, and C is deduced from the average of 6 different points for every  $\text{Ni}_x\text{N}$  samples.

Table 2-2. The normalized atom proportion of N, Ni, O, and C for  $\text{Ni}_x\text{N}$  samples with different  $P(\text{N}_2)$ , standard deviation is shown in the parentheses.

$P(\text{N}_2)$ /Pa	C /%	N /%	O /%	Ni /%	Ni/N
0	4.9 (0.16)	0.0 (0)	1.3 (0.06)	93.8 (0.26)	0.00
0.005	4.6 (0.13)	5.0 (0.17)	0.8 (0.11)	89.6 (0.22)	0.06
0.014	4.6 (0.14)	10.9 (0.12)	0.5 (0.16)	84.1 (0.18)	0.13
0.023	4.6 (0.21)	13.2 (0.26)	0.6 (0.10)	81.7 (0.16)	0.16
0.046	4.0 (0.26)	17.8 (0.15)	0.8 (0.06)	77.3 (0.20)	0.23
0.069	4.0 (0.12)	20.7 (0.11)	0.5 (0.14)	74.9 (0.17)	0.28
0.115	3.7 (0.11)	24.2 (0.13)	3.5 (0.06)	68.6 (0.13)	0.35
0.184	2.9 (0.13)	27.3 (0.10)	6.0 (0.06)	63.8 (0.14)	0.43

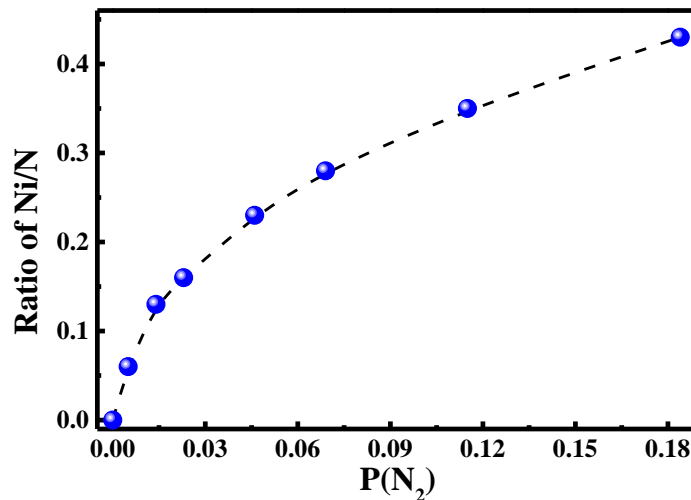


Fig. 2-11. The ratio of Ni/N with different  $P(\text{N}_2)$ .

Table 2-2 shows the normalized atom proportion of N, Ni, O, and C for  $\text{Ni}_x\text{N}$  samples with different  $P(\text{N}_2)$ . The samples were exposed in air ambient after sputtering, O, C and N contamination will inescapability absorb on the surface. The C proportion is about 3~5%

in the  $\text{Ni}_x\text{N}$  films. The O proportion is about 1% in the  $\text{Ni}_x\text{N}$  samples with low  $P(\text{N}_2)$ . However, the value of O proportion with  $P(\text{N}_2)$  of 0.115 and 0.184 Pa increased to 3.5% and 6%, respectively, implying the O atom is easily absorbed in the  $\text{Ni}_x\text{N}$  films with high  $P(\text{N}_2)$ . This result is consistent with the O1s peak in the XPS spectrum. Fig. 2-11 shows that the Ni/N ratio increased with the increasing  $P(\text{N}_2)$ . Meanwhile, the Ni/N ratio is also consistent with the  $\text{Ni}_x\text{N}$  phases showed in XRD spectra.

## §2.4. Conclusion

In this chapter,  $\text{Ni}_x\text{N}$  films were deposited by magnetron reactive sputtering under varying  $P(\text{N}_2)$  conditions range from 0.005 to 0.184 Pa. With the increasing  $P(\text{N}_2)$ , the deposition rate decreased while the resistivity and root mean square roughness increased. XRD and XPS indicate that  $\text{Ni}_4\text{N}$  and  $\text{Ni}_3\text{N}$  phases dominate the films at low and medium  $P(\text{N}_2)$ , respectively. In addition,  $\text{Ni}_2\text{N}$  phase can be also obtained at high  $P(\text{N}_2)$ . The Ni/N ratio evaluated from the energy dispersive X-ray spectrum is consistent with the  $\text{Ni}_x\text{N}$  phases showed in the XRD spectra of different  $P(\text{N}_2)$ .

## §2.5. References

- [1] Young A F, Sanloup C, Gregoryanz E, et al. Synthesis of novel transition metal nitrides IrN<sub>2</sub> and OsN<sub>2</sub>[J]. *Physical review letters*, 2006, 96(15): 155501.
- [2] Wittmer M. Properties and microelectronic applications of thin films of refractory metal nitrides[J]. *Journal of Vacuum Science & Technology A: Vacuum, Surfaces, and Films*, 1985, 3(4): 1797-1803.
- [3] Xie F, Liu T, Xie L, et al. Metallic nickel nitride nanosheet: an efficient catalyst electrode for sensitive and selective non-enzymatic glucose sensing[J]. *Sensors and Actuators B: Chemical*, 2018, 255: 2794-2799.
- [4] Hultman L. Thermal stability of nitride thin films[J]. *Vacuum*, 2000, 57(1): 1-30.
- [5] Xie J, Xie Y. Transition metal nitrides for electrocatalytic energy conversion: opportunities and challenges[J]. *Chemistry—A European Journal*, 2016, 22(11): 3588-3598.
- [6] Balogun M S, Qiu W, Wang W, et al. Recent advances in metal nitrides as high-performance electrode materials for energy storage devices[J]. *Journal of materials chemistry A*, 2015, 3(4): 1364-1387.
- [7] Xu K, Chen P, Li X, et al. Metallic nickel nitride nanosheets realizing enhanced electrochemical water oxidation[J]. *Journal of the American Chemical Society*, 2015, 137(12): 4119-4125.
- [8] Kim H D, An H M, Kim T G. Ultrafast resistive-switching phenomena observed in NiN-based ReRAM cells[J]. *IEEE Transactions on Electron Devices*, 2012, 59(9): 2302-2307.
- [9] Ao J P, Suzuki A, Sawada K, et al. Schottky contacts of refractory metal nitrides on gallium nitride using reactive sputtering[J]. *Vacuum*, 2010, 84(12): 1439-1443.
- [10] Yang L, Mi M, Hou B, et al. Enhanced g m and f T With High Johnson's Figure-of-Merit in Thin Barrier AlGa<sub>N</sub>/Ga<sub>N</sub> HEMTs by TiN-Based Source Contact Ledge[J]. *IEEE Electron Device Letters*, 2017, 38(11): 1563-1566.
- [11] Ao J P, Shiraishi T, Li L, et al. Synthesis and application of metal nitrides as Schottky electrodes for gallium nitride electron devices[J]. *Science of Advanced Materials*, 2014, 6(7): 1645-1649..
- [12] Ao J P, Naoi Y, Ohno Y. Thermally stable TiN Schottky contact on AlGa<sub>N</sub>/Ga<sub>N</sub>

- heterostructure[J]. *Vacuum*, 2013, 87: 150-154.
- [13] Yun M J, Kim H D, Man Hong S, et al. Effect of embedded metal nanocrystals on the resistive switching characteristics in NiN-based resistive random access memory cells[J]. *Journal of Applied Physics*, 2014, 115(9): 094305.
- [14] Dorman G, Sikkens M. Structure of reactively sputtered nickel nitride films[J]. *Thin Solid Films*, 1983, 105(3): 251-258.
- [15] Gage S H, Trewyn B G, Ciobanu C V, et al. Synthetic advancements and catalytic applications of nickel nitride[J]. *Catalysis Science & Technology*, 2016, 6(12): 4059-4076.
- [16] Kawamura M, Abe Y, Sasaki K. Formation process of Ni–N films by reactive sputtering at different substrate temperatures[J]. *Vacuum*, 2000, 59(2-3): 721-726.
- [17] Gajbhiye N S, Ningthoujam R S, Weissmüller J. Synthesis and magnetic studies of nanocrystalline nickel nitride material[J]. *physica status solidi (a)*, 2002, 189(3): 691-695.
- [18] Popović N, Bogdanov Ž, Gončić B, et al. Reactively sputtered Ni, Ni (N) and Ni<sub>3</sub>N films: Structural, electrical and magnetic properties[J]. *Applied Surface Science*, 2009, 255(7): 4027-4032.
- [19] 许振嘉. 半导体的检测与分析[J]. 2007. (In Chinese)
- [20] File P D. Joint Committee on Powder Diffraction Standards, International Centre for Diffraction Data[J]. Newton Square, PA., Card, 1987 (25-1280).
- [21] Grosvenor A P, Biesinger M C, Smart R S C, et al. New interpretations of XPS spectra of nickel metal and oxides[J]. *Surface Science*, 2006, 600(9): 1771-1779.
- [22] Yu Y, Gao W, Shen Z, et al. A novel Ni<sub>3</sub>N/graphene nanocomposite as supercapacitor electrode material with high capacitance and energy density[J]. *Journal of Materials Chemistry A*, 2015, 3(32): 16633-16641.
- [23] Dhunna R, Lal C, Avasthi D K, et al. Irradiation induced effects on Ni<sub>3</sub>N/Si bilayer system[J]. *Vacuum*, 2009, 83(12): 1448-1453.
- [24] Jiang Q W, Li G R, Liu S, et al. Surface-nitrided nickel with bifunctional structure as low-cost counter electrode for dye-sensitized solar cells[J]. *The Journal of Physical Chemistry C*, 2010, 114(31): 13397-13401.

## Chapter 3: Ni<sub>x</sub>N film for GaN-based SBD Application

### §3.1. Introduction

Schottky barrier diode (SBD) is the critical device of antenna-rectifier (rectenna) circuit in the microwave wireless power transmission systems, which is widely used in electric vehicle power charging, energy harvesting systems, power source, and in-building wireless power distribution. [1-3] However, the traditional GaAs- and Si-based commercial SBDs could not meet the development of the microwave wireless power transmission technology, which requires high conversion efficiency under high frequency and high voltage operation. Gallium nitride (GaN)-based materials exhibit many extraordinary features, including large bandgap, higher breakdown field, higher electron mobility and higher electron saturation velocity, accordingly GaN-SBDs have attracted much attention for improving the efficiency of microwave wireless power transmission system.[4-6]

Metal nitrides with high thermal stability were reported to replace the conventional metals as Schottky contact on GaN [7, 8], owing to its potential in suppression interface reaction between metal and GaN. For example, the most common Ni anode is reported to form a Ni-N alloy (a mixture of Ni<sub>3</sub>N, NiN and so on) after thermal treatment, resulting in the degradation of stability. [4, 9] We previous investigated the electrical performance of SBDs with TiN contact fabricated by reactive sputtering. [1, 10] The TiN SBDs have a lower turn-on voltage compared with Ni SBDs and better sensitivity for temperature sensing application. However, the SBDs with TiN electrode suffer from the problem of relatively larger reverse leakage current.

In chapter 2, we synthesize Ni<sub>x</sub>N by using magnetron reactive sputtering at different pressure ratios of Ar and N<sub>2</sub> mixture gas in which the Ni<sub>x</sub>N films show different NiN phase appeared. It was reported that Ni<sub>x</sub>N can avoid interface reaction between anode and GaN, and possesses a high work function, showing the potential to serve as the SBD anode to reduce leakage current. Therefore, it is very necessary to explore the application of Ni<sub>x</sub>N on Schottky contact.

In this chapter, Ni<sub>x</sub>N films, prepared by magnetron reactive sputtering at different

pressure ratios of Ar and N<sub>2</sub> mixture gas, were employed as anode material for GaN SBD application. Comparing with the GaN diodes with Ni anode, the SBH and turn-on voltage of the SBDs with Ni<sub>x</sub>N anode are increased with 0.03~0.18 eV and 0.03~0.15 V, respectively. *C-V* curves demonstrate that good interface quality with no obvious hysteresis was realized. Ni<sub>3</sub>N anode diodes obtained at medium P(N<sub>2</sub>) possess a high barrier height and a low reverse leakage current and are regarded as a promising anode material. In addition, The *I-V-T* characteristics demonstrate that the NiN-SBDs have better thermal stability than that of Ni-SBDs, owing to the suppression of interface reaction between Ni and GaN.

### §3.2 Devices structure and fabrication

The n-GaN epitaxial layers, grown by MOCVD on (0001) sapphire substrate, was used in this experiment. The vertical structure (shown in Fig.3-1 (a)) of the wafers consisted of a thin nucleating layer, a 3.5 μm thickness n-type GaN layer (doping concentration:  $2 \times 10^{18} \text{cm}^{-3}$ ), and a 1 μm Si-doped Schottky contact layer (doping concentration:  $1.6 \times 10^{16} \text{cm}^{-3}$ ) from bottom to top. We adopted standard lithography process to fabricate the Ni<sub>x</sub>N/GaN SBDs and the fabrication process flow chart is shown in Fig. 3-2.

At the beginning of fabrication, the GaN wafers were cleansed by SPM (H<sub>2</sub>SO<sub>4</sub>:H<sub>2</sub>O<sub>2</sub>=4:1), acetone and pure water were used for removing the organic and inorganic matters.

By using a standard photolithography technology, cathode electrode of Ti/Al/Ti/Au (50/200/40/40 nm) multi-layer were deposited on the n-GaN epitaxial layers by reactive sputtering.

After the lift-off process, the samples were annealed under 850 °C for 3 min in a N<sub>2</sub> ambient to from the ohmic contacts.

The Schottky electrode fabrication process was based on the standard photolithography and lift-off technology. Before the deposition of the Schottky electrode, the wafers were soaked in diluted HCl with 5 min for removing the possible oxide layer on the wafer surface formed by the O<sub>2</sub> plasma ashing.

Then, the Ni<sub>x</sub>N/Au (100/30nm) Schottky electrode was deposited by using reactive sputtering in an Ar and N<sub>2</sub> mixture ambient. The Ar partial pressure was kept at 0.11 Pa, while the P(N<sub>2</sub>) were varied from 0.005 to 0.18 Pa (0.005, 0.014, 0.023, 0.046, 0.069,

0.115 and 0.184 Pa).

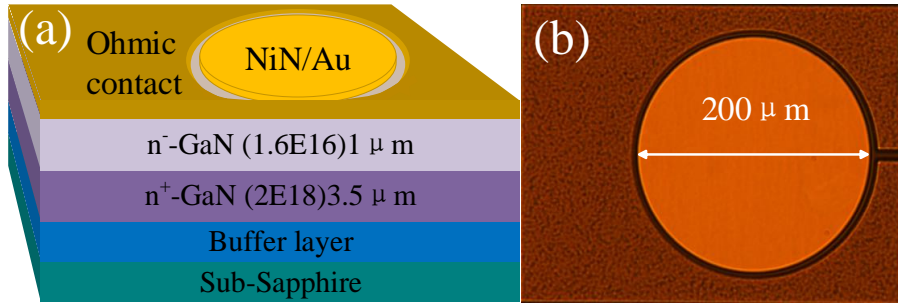


Fig. 3-1. The schematic cross section (a) and optical photo (b) of the circular SBDs.

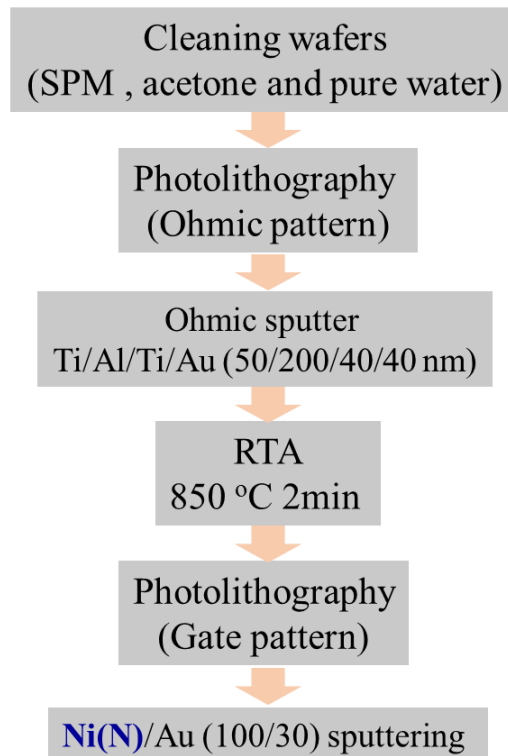


Fig. 3-2. The schematic fabrication process of the Ni(N)/GaN-SBDs.

As shown in Fig. 3-1 (b), circular Schottky anode (diameter of 200 μm) was surrounded by ohmic contacts with a distance of 5 μm. For comparison, we also fabricated samples with Ni electrode under the same process.

### §3.3. Ni<sub>x</sub>N/GaN SBDs characteristics

#### §3.3.1. *I-V* characterization

In order to obtain average value, we measured more than 20 different devices randomly to obtain the current-voltage characteristics at room temperature. Then, the arithmetic mean and the standard deviation were adopted to determine the average value and error bar, respectively. The  $I$ - $V$  characteristics of the  $\text{Ni}_x\text{N}/\text{GaN}$  SBDs were measured under the room temperature by using the semiconductor parameter analyzer Agilent 4155. As shown in the Fig. 3-3, the voltage range of the  $I$ - $V$  curves measured by double-sweep mode is from -10 to 2 V for the reverse and forward. The voltage step is set 0.02~0.2 V, and the protection current threshold is set to be 0.1 A.

All samples show the good rectification characterization at all  $P(\text{N}_2)$ . When the  $P(\text{N}_2)$  is 0.046 and 0.184 Pa, the leakage current of the Ni(N)-SBD measured at -10V is slightly decrease compare with the Ni-SBD, and even samples with  $P(\text{N}_2)$  of 0.005, 0.014 and 0.115 Pa show that leakage current is bigger than Ni-SBD. It's worth noting that, the leakage current at the  $P(\text{N}_2)$  of 0.023 Pa shows significant decrease. However, the curve of the  $I$ - $V$  current at reverse area has significant jitter and is not very smooth, although we have tested multiple devices. When the  $P(\text{N}_2)$  is 0.069 Pa corresponding to  $\text{Ni}_3\text{N}$  phase, the device shows good rectification characterization, and the curve is smoother and the hysteresis is better.

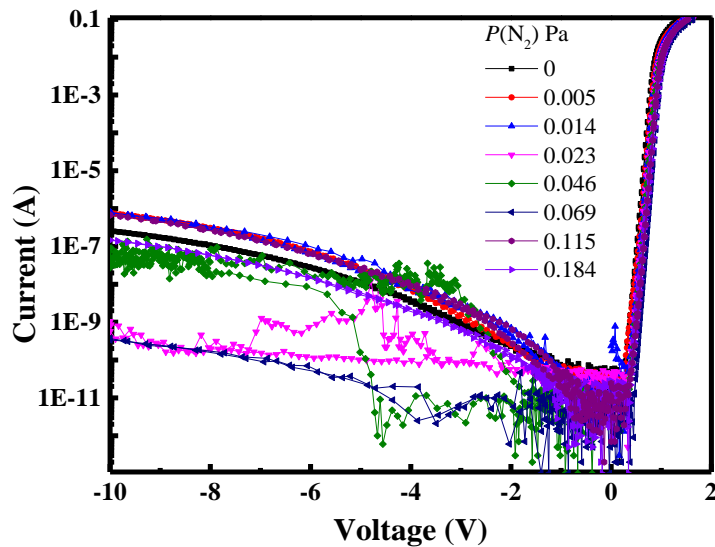


Fig. 3-2.  $I$ - $V$  curves of circular diodes with different  $P(\text{N}_2)$ .

The SBH and ideality factor  $n$  were extracted by fitting the forward-biased  $I$ - $V$  curves of the diodes using the thermionic emission (TE) model [11] which is given in equation (3-1),

$$I = A_e A^* T^2 \exp\left(-\frac{q\phi_B}{kT}\right) \left[ \exp\left(\frac{qV}{kT}\right) - 1 \right] \quad (3-1)$$

$$A^* = \frac{4\pi q m^* k^2}{h^3} \quad (3-2)$$

where  $A_e$  is the effective diode area,  $A^*$  the effective Richardson constant,  $26.9 \text{ Acm}^{-2} \text{K}^{-2}$  for GaN,  $T$  the absolute temperature in kelvin,  $q$  the electron charge,  $k$  the Boltzmann constant, and  $\phi_B$  the effective barrier height from the metal to the semiconductor. The effective Richardson constant is given in equation (3-2), where  $m^*$  is the effective mass for GaN:  $m^* = 0.20$ ,  $m_0 = 1.82 \times 10^{-31} \text{ kg}$ ,  $m_0$  the electron rest mass,  $h$  the Planck's constant ( $h = 6.6261 \times 10^{-34} \text{ J s}$ ).

When  $qV \geq 3kT$ , then  $\exp\left(\frac{qV}{nkT}\right) \geq 1$ , the forward current density can be obtained from equation (3-1), which is following:

$$J = A^* T^2 \exp\left(-\frac{q\phi_b}{kT}\right) \exp\left(\frac{qV}{nkT}\right) \quad (3-3)$$

Solving (3-3) to:

$$\ln J = \frac{qV}{nkT} + \ln(A^* T^2) - \frac{q\phi_b}{kT} \quad (3-4)$$

where,  $J (= I / A_e)$  is the current density of the SBDs.

Then, we select the linearity region for linear fitting, the ideality factor  $n$  can be calculated from the slope  $\left(\frac{q}{nkT}\right)$  of the linear fitting. Meanwhile, the SBH  $\phi_b$  is obtained

from the intercept  $\left(\ln(A^* T^2) - \frac{q\phi_b}{kT}\right)$  of the linear fitting.

Fig. 3-3. shows the logarithmic and linear current density verses voltage characteristics of the Ni<sub>x</sub>N/GaN SBDs in forward bias region. With increasing of the P(N<sub>2</sub>), the curves show positive shift in the forward bias region.

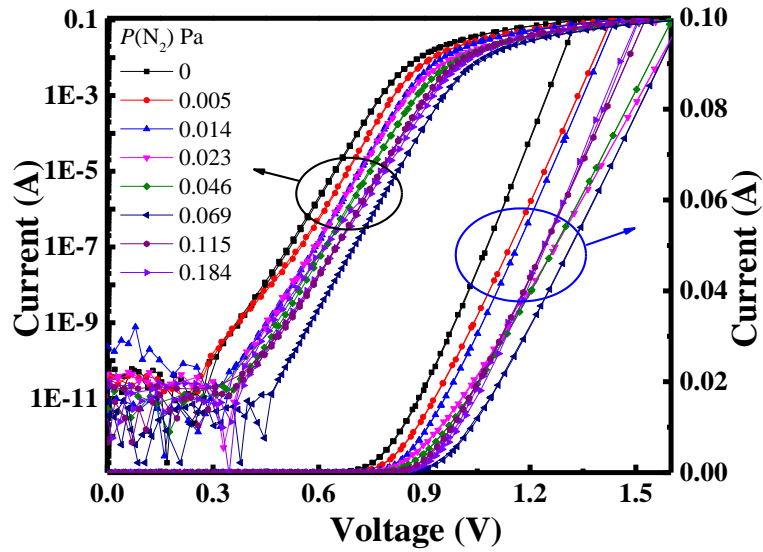
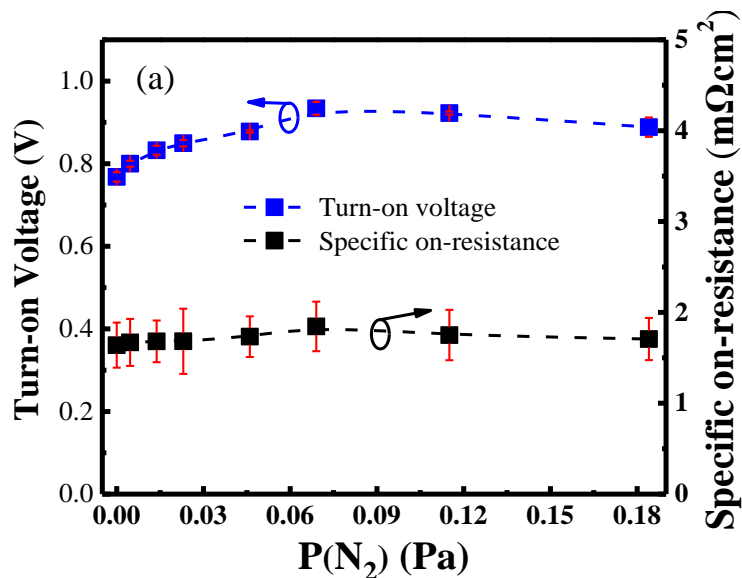


Fig. 3-3  $I$ - $V$  characteristics of Ni(N) SBDs in the forward bias region with linear and logarithmic coordinates.

The turn-on voltages, defined as the voltages corresponding to a current of 1mA, are 0.77, 0.80, 0.83, 0.85, 0.88, 0.93, 0.92, and 0.89 V for the devices with  $P(N_2)$  of 0, 0.005, 0.014, 0.023, 0.046, 0.069, 0.115 and 0.184 Pa, respectively, as shown in Fig. 3-4 (a) and Fig. 3-4 (b).



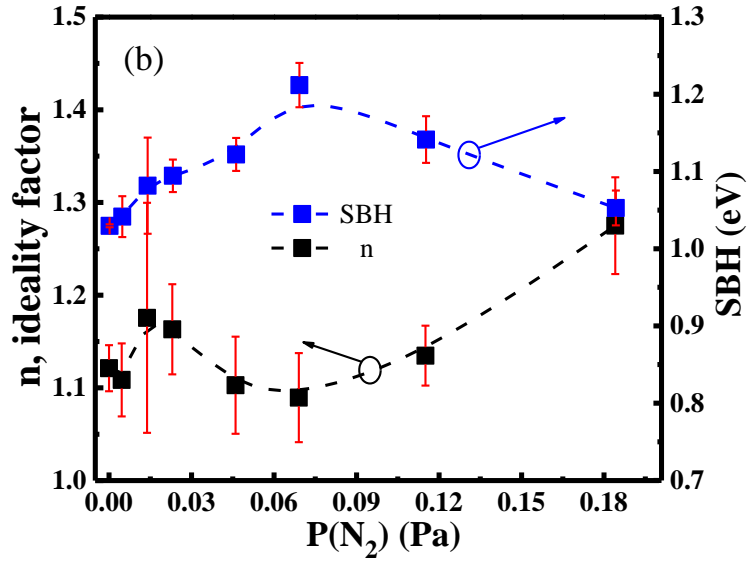


Fig. 3-4. (a) Turn-voltage and specific on-resistance, (b) ideality factor and SBH of Ni<sub>x</sub>N/GaN SBDs.

The reference Ni-GaN SBDs present a SBH of 1.03 eV and ideality factor of 1.12. The ideality factor of all samples with P(N<sub>2</sub>) from 0 to 0.184 Pa are concentrated between 1.04 and 1.27, which indicates that the thermionic emission transport mechanisms is dominant. SBH of the samples increases with the partial pressure and reaches the highest value, and then decreases. The highest SBH of 1.21 eV is obtained with P(N<sub>2</sub>) of 0.069 Pa, meanwhile the ideality factor is 1.09. Comparing with the pure nickel GaN SBDs, all the samples with different P(N<sub>2</sub>) show that the SBH has a certain improvement.

However, the increasing of SBH does not mean the obvious suppression of leakage current in the reverse bias region. The samples with P(N<sub>2</sub>) of 0.005, 0.014, and 0.115 Pa even show a higher leakage current than that of Ni-SBD. A possible reason is that the obtained films are the mixture of Ni and Ni<sub>4</sub>N with small grain size. The high density of grain boundary will increase the leakage current. While for the Ni<sub>3</sub>N dominated film formed at a P(N<sub>2</sub>) of 0.069 Pa, the good crystalline quality and large grain size are beneficial for improving the interface with high SBH and ideality factor, resulting in a leakage current that was two orders of magnitude lower than the Ni-SBDs.

### §3.3.2. C-V characteristics

The C-V curves were measured in double-sweep mode (@1MHz) for samples obtained

at different  $P(N_2)$ , as shown in Fig. 3-5. It demonstrated that no obvious hysteresis was observed in all curves, implying the good interface quality. Moreover, we also measured the  $C-V$  curves under different frequencies (Fig. 3-6). The  $C-V$  curves are smoother under higher frequency and mild fluctuation under lower frequency. However, no obvious hysteresis was observed in all curves.

In fact, the plasma induced by high bias just surrounds the metal target, while the substrate is placed on a water cooling copper hold. The distance between target and substrate is adjusted to about 10 cm. Furthermore, we chose a relative lower growth rate to deposit the films. Therefore, the sputtering process generate relatively slight damage on the surface.

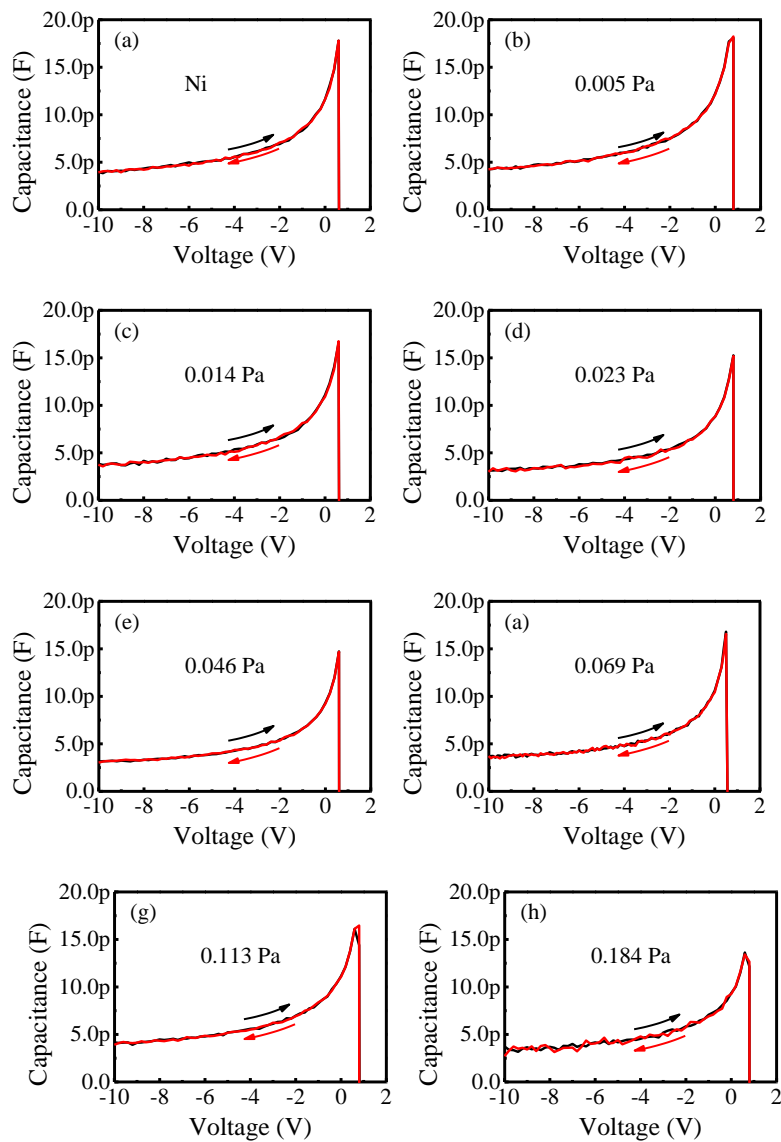


Fig. 3-5. The double-sweep mode  $C-V$  curves of samples obtained at different  $P(N_2)$  samples.

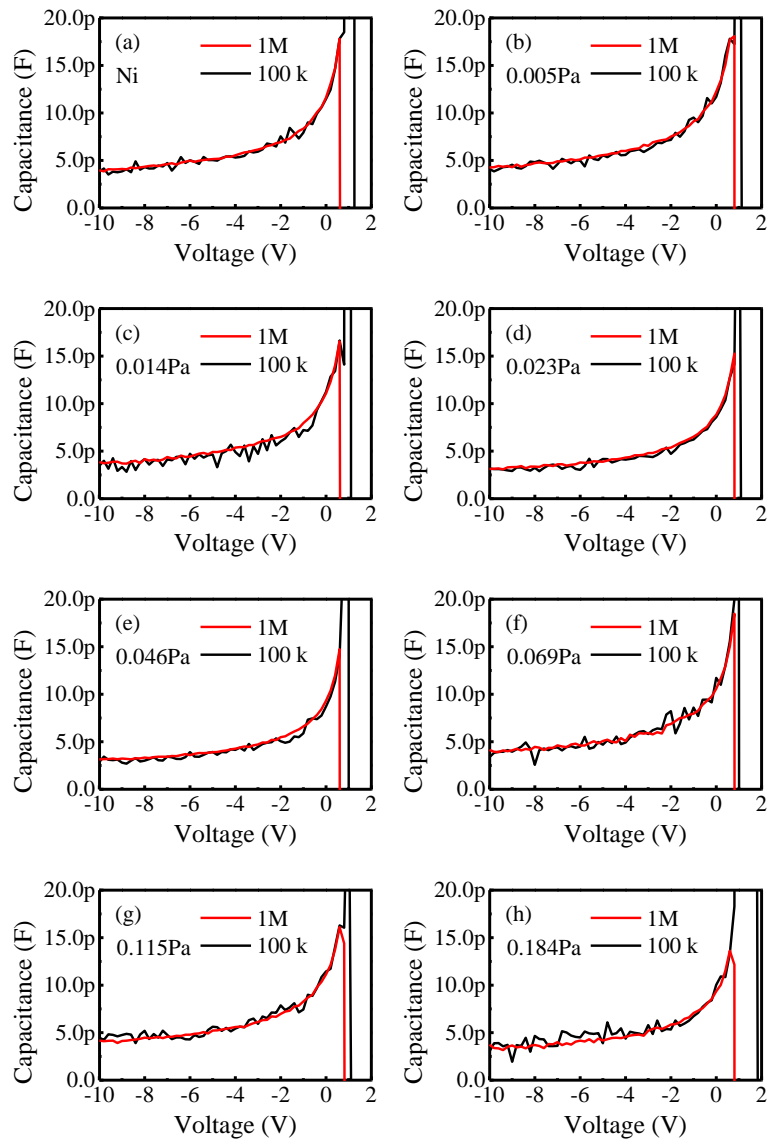


Fig. 3-6. The high and low frequency double-sweep mode  $C$ - $V$  curves of samples obtained at different  $P(N_2)$  samples.

### §3.4. Thermal stability of Ni<sub>3</sub>N/GaN SBD

Thermal stability is a very important performance for a electronic device. Thus, it is necessary to analyze the thermal stability of the NiN/GaN SBD. Based on the previous discussion, when the  $P(N_2)$  is kept at 0.069 Pa, relative pure Ni<sub>3</sub>N phase dominate in the NiN Film. Meanwhile, the NiN/GaN SBD shows a significant leakage current reduction.

### §3.4.1. Characteristic of Ni<sub>3</sub>N/GaN SBD at room-temperature

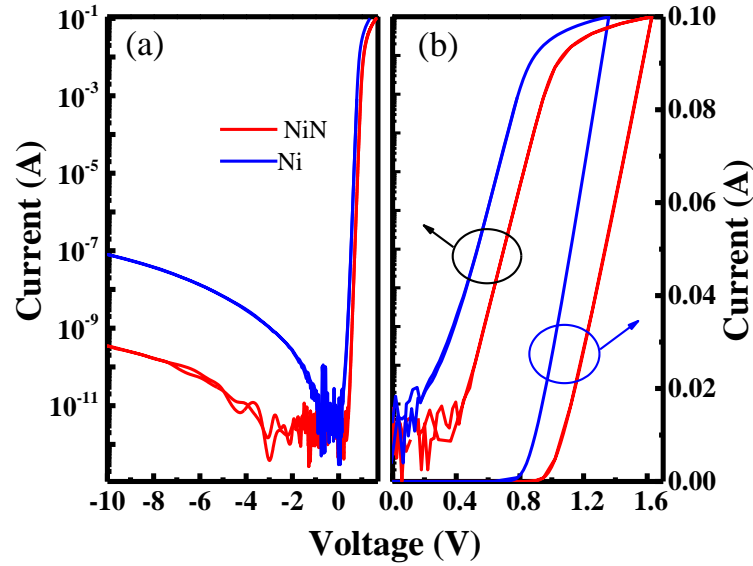


Fig. 3-7. (a)  $I$ - $V$  characteristics of the circular device, (b)  $I$ - $V$  characteristics of NiN- and Ni-SBDs in the forward bias region.

The  $I$ - $V$  characteristics of the NiN- and Ni-GaN SBDs are shown in Fig. 3-7 (a). When thermionic emission theory was used, the SBH of the NiN- and Ni-SBD are deduced to approximately 1.19 eV and 1.03eV, respectively. Meanwhile, the values of ideality factor ( $n$ ) were 1.10 and 1.13 for the NiN- and Ni-SBD, respectively. The reverse leakage current of the NiN device is approximately two orders of magnitude lower compared with the Ni-SBD. Moreover, the calculated reverse current is far less than the measured one, implying other mechanism such as trap-assisted tunneling process dominate the reverse leakage current. [12] From the Fig. 3-7 (b), the turn-on voltages, defined as the voltages corresponding to a current of 1mA, are approximately 0.79 and 0.95 V for the NiN-SBD and Ni-SBD, respectively.

The  $C$ - $V$  characteristics of the Ni- and NiN-SBDs are shown in Fig. 3-8. The capacitances obtained at zero bias are about  $3.73 \times 10^{-7}$  and  $3.12 \times 10^{-7}$  F/cm<sup>2</sup> for the Ni and NiN SBDs, respectively. The SBH can be also determined by the  $C$ - $V$  method [11], and it is given by

$$\phi_{bn}(C - V) = qV_{bi} + (E_c - E_f) \quad (3-2)$$

where,  $V_{bi}$  is the built-in voltage, which can be extrapolated from the line of  $1/C^2$  versus

$V$  (as shown in the inset of Fig. 3-8).  $E_c$  is the conduction-band energy and  $E_f$  is the fermi energy.

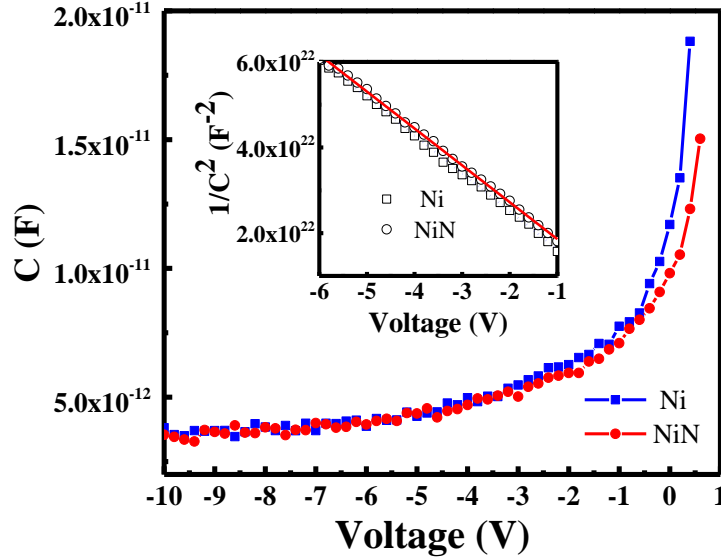


Fig. 3-8.  $C$ - $V$  characteristics and  $1/C^2$  versus applied voltage for NiN and Ni SBD (inset) at room temperature with 1MHz sampling frequency. The red line and the blue line are the linear fit curves (inset).

The energy difference between the conduction-band energy and fermi energy is given by

$$E_c - E_f = \frac{kT}{q} \ln\left(\frac{N_c}{N_d}\right) \quad (3-3)$$

where,  $T$  is 300K,  $N_c$  is the effective density of the state in the GaN, and  $N_d$  is the donor concentration which can be calculated from the  $C$ - $V$  measurements, and the  $N_d$  of Ni and NiN samples are  $1.70$  and  $1.62 \times 10^{16} \text{ cm}^{-3}$ , respectively. From the  $C$ - $V$  method, the SBH of the Ni and NiN SBDs are  $1.0 \text{ eV}$  and  $1.2 \text{ eV}$ , respectively. Those values are slighter higher than that derived from  $I$ - $V$  measurements. This is ascribed to that the capacitance in  $C$ - $V$  method is insensitive to potential fluctuation, resulting in a homogeneous SBH over the whole Schottky area. While for the  $I$ - $V$  measurement, the current flows through the region of low SBH at zero-bias dominate the current.

### §3.4.2. Characteristic of Ni<sub>3</sub>N/GaN SBD at different temperature

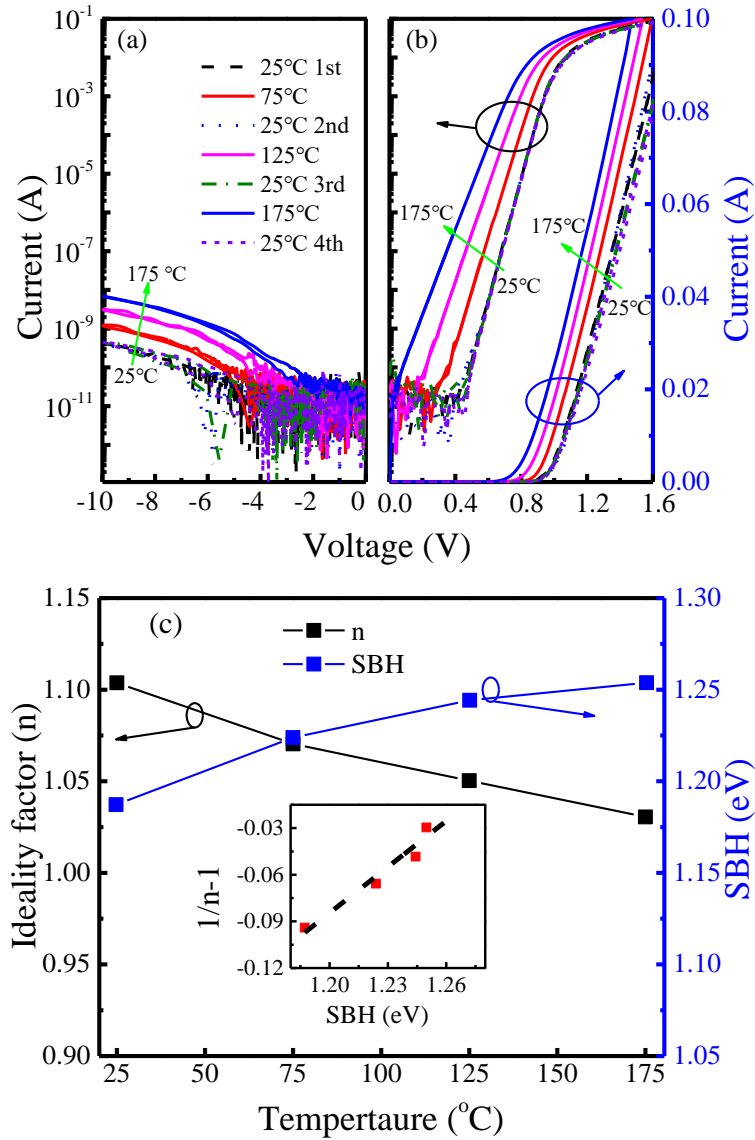


Fig. 3-9. (a)  $I$ - $V$  characteristics of NiN SBD measured at different temperature in the reverse bias region, (b)  $I$ - $V$  characteristics of NiN SBD in the forward bias region, (c) SBH and  $n$  values of NiN SBDs measured under different temperatures, (inset of c) SBH versus  $1/n-1$ .

For evaluating the thermal stability, the devices were heated from 25  $^{\circ}$ C to 75 (125 and 175)  $^{\circ}$ C, and then cooled down to 25  $^{\circ}$ C for measurements of the  $I$ - $V$  curves of the NiN-SBD. As shown in Fig. 3-9 (a), the NiN SBD shows good rectification characterization at all temperatures. After each thermal treatment, the leakage current under -10 V can return to the initial value ( $3.6E-10$  A) measured at 25  $^{\circ}$ C, which confirms that the device has very good thermal stability.

Fig. 3-9 (b) shows the forward bias region of the  $I$ - $V$  characteristics with linear and logarithmic coordinates. With increasing temperature, the turn-on voltage shows negative shift (Fig. 3-9 (b)), but it can still return to the original value after each thermal treatment. Fig. 3-9 (c) shows the SBH and  $n$  values of NiN SBD measured at different temperatures. When the temperature is increased from 25 °C to 75, 125, and 175°C, the SBH increases from 1.19 eV to 1.22, 1.24, and 1.25 eV, respectively, and the  $n$  value decreased from 1.10 to 1.07, 1.05, and 1.03, respectively. From the inset of Fig. 3-9 (c), the plot of SBH versus  $n$  presents a good linear relationship. This is usually ascribed to the inhomogeneous SBH of the Schottky contact. The SBH inhomogeneous behavior is a common phenomenon and the possible mechanism have been ascribed to many factors, such as the gate metal [13], surface morphology of the material [14], surface defect, the metal deposition process. [15, 16] In our experiment, the sputtering ratio of the Schottky electrode is very slow (approximately 0.33 Å/s). Therefore, the RMS is relatively small and the contact between the Schottky electrode and the GaN is relatively homogeneous. A possible reason for this barrier height inhomogeneous may be ascribed to the high dislocation density of the GaN material on sapphire substrate due to the large thermal and lattice mismatch.

The temperature dependency results of Ni SBD are shown in the Fig. 3-10, in which the  $n$  and the SBH also show the inhomogeneous behavior. The Ni SBD was observed weak degradation which appeared after 175 °C thermal, which was consistent with the results of our previous studies [9, 10]. The poor thermal stability of Ni-SBD may be caused by the mixtures of Ni<sub>4</sub>N, Ni<sub>3</sub>N and Ni presenting in the interface of Ni/GaN after annealing [4]. From the temperature dependence of the Ni- and NiN-SBDs, we demonstrated that the NiN Schottky electrode by sputtering can help to suppress the interface reaction, the NiN-SBDs show better thermal stability accordingly.

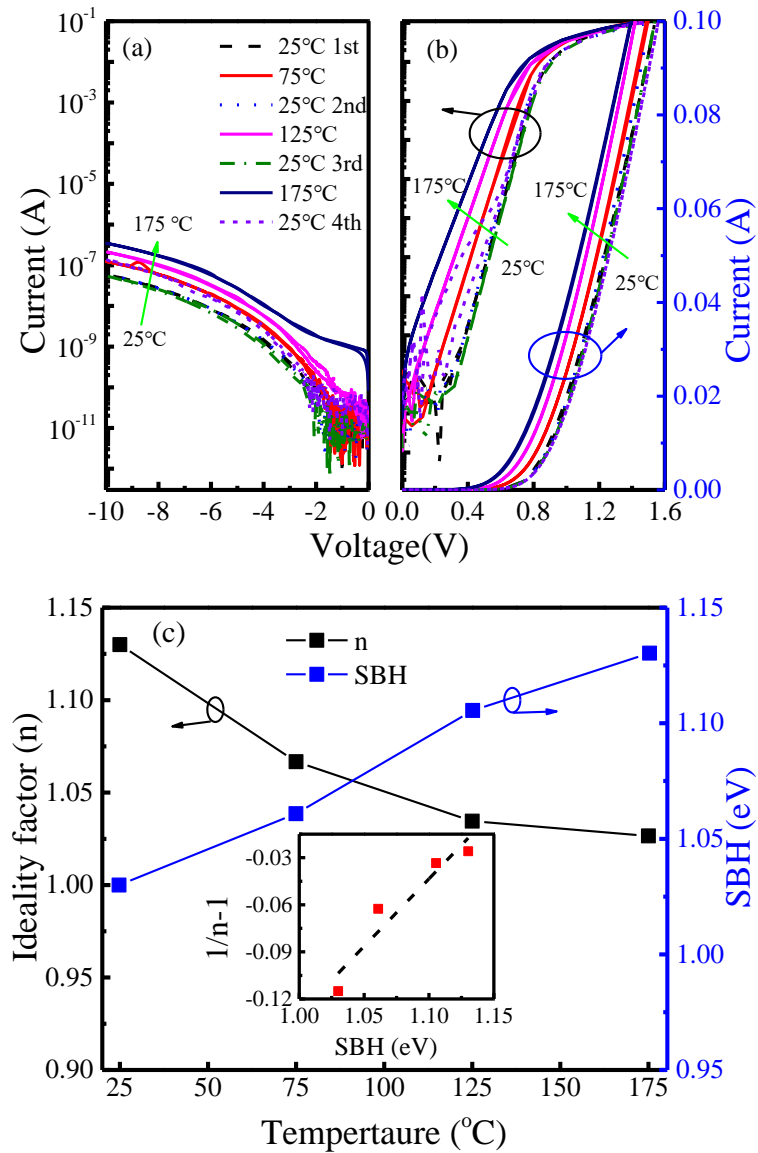


Fig. 3-10. (a)  $I$ - $V$  characteristics of Ni SBD measured at different temperature in the reverse bias region, (b)  $I$ - $V$  characteristics of Ni SBD in the forward bias region, (c) SBH and  $n$  values of Ni SBDs measured under different temperatures, (inset of c) SBH versus  $1/n-1$ .

Fig. 3-11 shows the forward voltage at different currents (20, 40, 60, 80 and 100 mA) versus different temperatures. For the temperature sensor, the sensitivity is defined by the slope of the  $V$ - $T$  profile. By linear fitting the  $V$ - $T$  profile, the sensitivity of the NiN-SBD is deduce to approximately 1.3 mV/K, which is higher than the Ni-SBD (around 1.1 mV/K) and TiN-SBD (around 1.0 mV/K) with the same size [10].

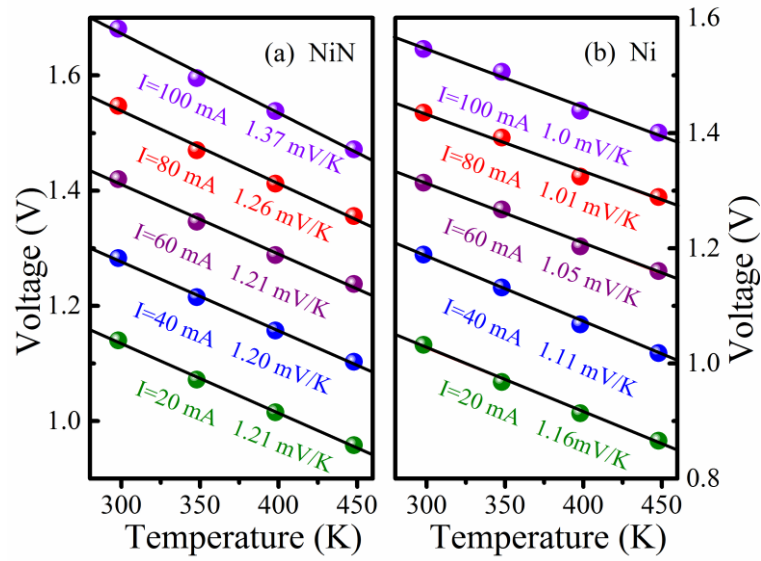


Fig. 3-11. Forward voltage at different currents versus different temperature for the (a) NiN- and (b) Ni-SBD.

### §3.5. Conclusion

Ni<sub>x</sub>N films deposited by magnetron reactive sputtering under varying P(N<sub>2</sub>) conditions range from 0.005 to 0.184 Pa were used for SBD application. Comparing with the Ni GaN sample, the SBH of the Ni<sub>x</sub>N SBDs shows an increase of 0.03~0.18 eV with different P(N<sub>2</sub>). No obvious hysteresis observed in all samples C-V curves, demonstrating the good interface quality in the Schottky contact. The Ni<sub>3</sub>N film with good crystalline quality and large grain size is beneficial for improving the interface with high SBH and low ideality factor, resulting in a leakage current that was two orders of magnitude lower than Ni-SBD.

Finally, the Ni<sub>3</sub>N/GaN SBD shows good rectification characterization at different temperatures without any obvious degradation after thermal treatment. The sensitivity of NiN-SBD varies slightly at different current levels is 1.3 mV/K and shows the potential for temperature sensing application.

### §3.6. References

- [1] Li L, Kishi A, Liu Q, et al. GaN Schottky barrier diode with TiN electrode for microwave rectification[J]. IEEE Journal of the Electron Devices Society, 2014, 2(6): 168-173.
- [2] Lepselter M P, Sze S M. Silicon Schottky barrier diode with near - ideal I - V characteristics[J]. Bell System Technical Journal, 1968, 47(2): 195-208.
- [3] Cetin H, Ayyildiz E. Temperature dependence of electrical parameters of the Au/n-InP Schottky barrier diodes[J]. Semiconductor science and technology, 2005, 20(6): 625.
- [4] Guo J D, Pan F M, Feng M S, et al. Schottky contact and the thermal stability of Ni on n - type GaN[J]. Journal of applied physics, 1996, 80(3): 1623-1627.
- [5] Lu M, Zhang G, Fu K, et al. Gallium Nitride Schottky betavoltaic nuclear batteries[J]. Energy Conversion and Management, 2011, 52(4): 1955-1958.
- [6] Mohammad S N, Fan Z, Botchkarev A E, et al. Near-ideal platinum-GaN Schottky diodes[J]. Electronics Letters, 1996, 32(6): 598-599.
- [7] Ao J P, Shiraishi T, Li L, et al. Synthesis and application of metal nitrides as Schottky electrodes for gallium nitride electron devices[J]. Science of Advanced Materials, 2014, 6(7): 1645-1649.
- [8] Ao J P, Naoi Y, Ohno Y. Thermally stable TiN Schottky contact on AlGaN/GaN heterostructure[J]. Vacuum, 2013, 87: 150-154.
- [9] Li L, Wang X, Liu Y, et al. NiO/GaN heterojunction diode deposited through magnetron reactive sputtering[J]. Journal of Vacuum Science & Technology A: Vacuum, Surfaces, and Films, 2016, 34(2): 02D104.
- [10] Li L, Chen J, Gu X, et al. Temperature sensor using thermally stable TiN anode GaN Schottky barrier diode for high power device application[J]. Superlattices and Microstructures, 2018, 123: 274-279.
- [11] Sze S M, Ng K K. Physics of semiconductor devices[M]. John wiley & sons, 2006.
- [12] E. J. Miller, E. T. Yu, P. Waltereit, and J. S. Speck, Analysis of reverse-bias leakage current mechanisms in GaN grown by molecular-beam epitaxy, Appl. Phys. Lett. 84 (2004) 535-537.
- [13] J-H. Shin, J. Park, S. Y. Jang, T. Jang, and K. S. Kim, Metal induced inhomogeneous Schottky barrier height in AlGaN/GaN Schottky diode, Appl. Phys. Lett. 102 (2013)

243505.

[14] G. Greco, F. Giannazzo, P. Fiorenza, S. D. Franco, A. Alberti, F. Iucolano, I. Cora, B. Pecz, and F. Roccaforte, Barrier Inhomogeneity of Ni Schottky Contacts to Bulk GaN Phys. Status Solidi A 215 (2018), 1700613.

[15] N. Yıldırım, K. Ejderha, and A. Turut, On temperature-dependent experimental and data of Schottky contacts J Appl. Phys. 108 (2010) 114506.

[16] R. T. Tung, Electron transport at metal-semiconductor interfaces: General theory, Phys. Rev. B 45 (1992) 13509.



## Chapter 4: GaN-based Diode for Temperature Sensor Application

### §4.1. Introduction

High temperature environment operation as well as the self-heating effect of a power device will obviously arise the junction temperature, and then deteriorate the device performance. Semiconductor diodes such as SBD and PND are commonly used for temperature sensor application. [1, 2] The sensing ability of a diode temperature sensor bases on the quasi-linear dependence of forward voltage on temperature, [3] requiring good thermal stability and linearity. GaN based power devices show excellent performance and are widely used in space, high radiation, high temperature and other harsh environmen because GaN has advantages of wide-bandgap, high breakdown voltage, radiation-resistant and high temperature stability. [4-5] However, the GaN-compatible temperature sensor that can monitor the device temperature in-situ is not investigated extensively. [6]

In this chapter, we employ NiO and TiN electrodes for the GaN-based PND and temperature sensors application to investigate the correlation between anode area and sensitivity. The contribution of series resistance shows very different between NiO/GaN PND and TiN/GaN SBD temperature sensors in the fully-turn-on state. In the sub-threshold region, the sensitivities of both NiO/GaN PND and TiN/GaN SBD temperature sensors are determined by forward current density, in which a larger current density correspond to a lower sensitivity. What's more, based on the theoretical analysis of the TE mode, we found the NiN electrode SBD temperature sensor shows the high linear and near-ideal sensitivity of the GaN-based SBD temperature.

### §4.2. NiO/GaN PND temperature sensor

NiO is a 3d transition metal oxide [7-8] and a typical direct wide bandgap p-type semiconductor. The bandgap of the NiO film is usually 3.6~4.0 eV [9-11]. Due to its unique electronic structure, NiO has shown excellent application prospects in many fields such as transparent conductive films, gas sensors, UV detectors and electrochromic devices, etc. [11-18].

Recently, NiO has been reported with an excellent chemical stability in GaN-based optoelectronic and electronic devices [19, 20]. The outstanding rectifying behavior and good thermal stability of p-NiO/n-GaN heterojunction diode is suitable for the microwave power rectification [21], meaning that it can be a possible candidate for temperature sensing.

#### §4.2.1. Theoretical modeling of a p-NiO/n-GaN heterojunction diode

Under a forward bias ( $V_F$ ), the diode current ( $I_D$ ) is expressed as the following equation when  $V_F > 3kT/q$  [22, 23]:

$$I_D = A^* e^{-\frac{qE_g}{kT}} e^{\frac{q(V_F - R_S I_D)}{nkT}} \quad (4-1)$$

Where,  $n$ ,  $k$ ,  $q$ ,  $R_S$  and  $T$  are the ideality factor, Boltzman constant, electronic charge, series resistance and Kelvin temperature, respectively.  $R_S I_D$  is voltage drop across series resistance ( $R_S$ ).  $A^* = AqXN_{Dp}(D_{np}/\tau_{np})^{1/2}$ , where  $A$  and  $X$  are the junction area and transmission coefficient for the interface, respectively,  $N_{Dp}$ ,  $D_n$  and  $\tau_{np}$  are the donor impurity concentration, diffusion constant and electron life-time in GaN, respectively. Since these parameters are temperature-dependent,  $A^*$  can be expressed as  $A^* = ACT^r$ , where  $C$  is a constant and  $r$  a process-dependent parameter [22].  $E_g$  is the band gap of n-GaN.

Then the  $I_D$  can be simplified to

$$I_D = ACT^r e^{-\frac{qE_g}{kT}} e^{\frac{q(V_F - R_S I_D)}{nkT}} \quad (4-2)$$

Solving for  $V$  yields

$$V_F = E_g + I_D R_S + \frac{nkT}{q} \left( \ln \frac{I_D}{AC} - r \ln T \right) \quad (4-3)$$

According to some reports [22, 24], the nonlinear part of equation (4-3) has vanishingly small effect until very high temperature. Hence, the  $V_F$  drop is approximately a linear function of temperature at a constant current.

#### §4.2.2. Device structure and fabrication

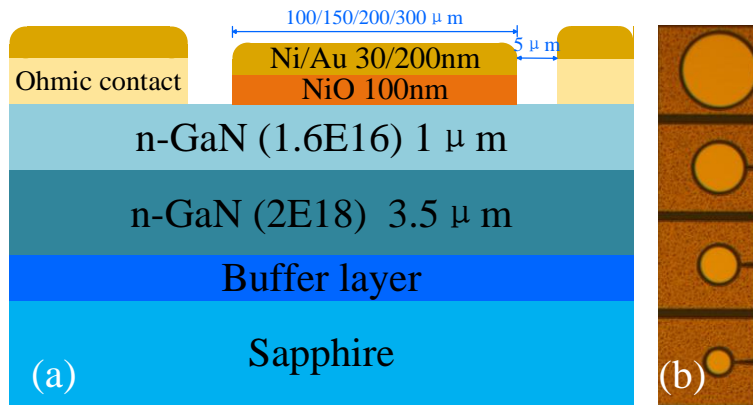


Fig. 4-1. Schematic cross-sectional (a) and optical (b) images of the NiO/GaN diode temperature sensors with diameters of 100, 150, 200 and 300  $\mu\text{m}$ , respectively.

The device structure is shown in the Fig. 4-1, and the fabrication process is based on standard lithography process, which follow the description in chapter 3. The NiO anode electrodes (followed our previous study [21]) with diameters of 100, 150, 200 and 300  $\mu\text{m}$  were deposited by reactive sputtering with a Ni metal target. In order to facilitate probe measurement, thick Au (Ni/Au 30/200 nm) was deposited on all the electrode surface at last.

#### §4.2.3. Characteristics and discussion

##### (1) Sensitivity at the fully-turn-on state

Fig. 4-2 (a) shows the typical forward bias  $I$ - $V$  characteristics in linear coordinate of the diode with a diameter of 150  $\mu\text{m}$ . The  $I$ - $V$  curves with an obvious temperature dependence shift negatively when the temperature increases from 25 to 200 $^{\circ}\text{C}$  with a step of 25  $^{\circ}\text{C}$ . The corresponding  $n$  and  $R_s$  at different temperatures are fitted and summarized in Fig. 4-2 (b). The fact that the  $n$  values close to 2 implies that the recombination current dominates. The decrease of the  $n$  and  $R_s$  values at higher temperature as well as the linear negative shift of the turn-on voltages were caused by the thermally excited carriers and enhanced current diffusion [25].

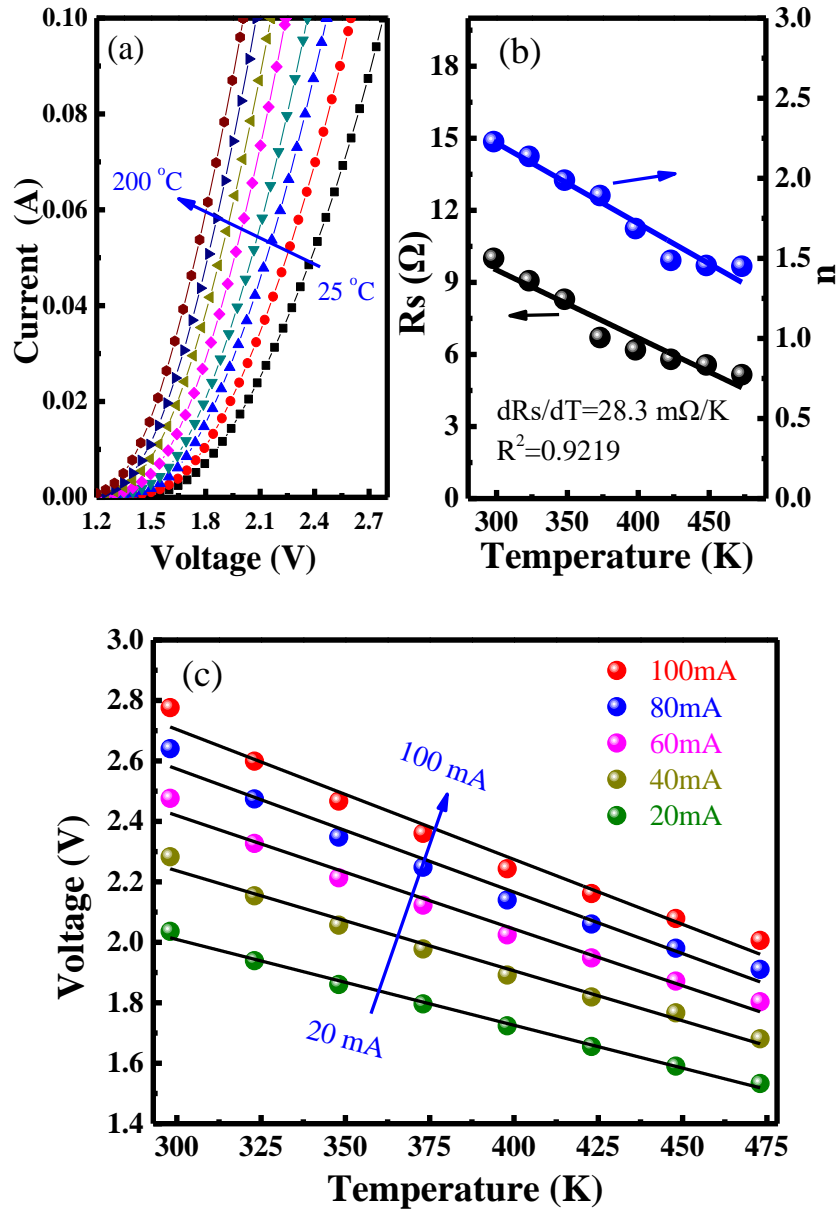


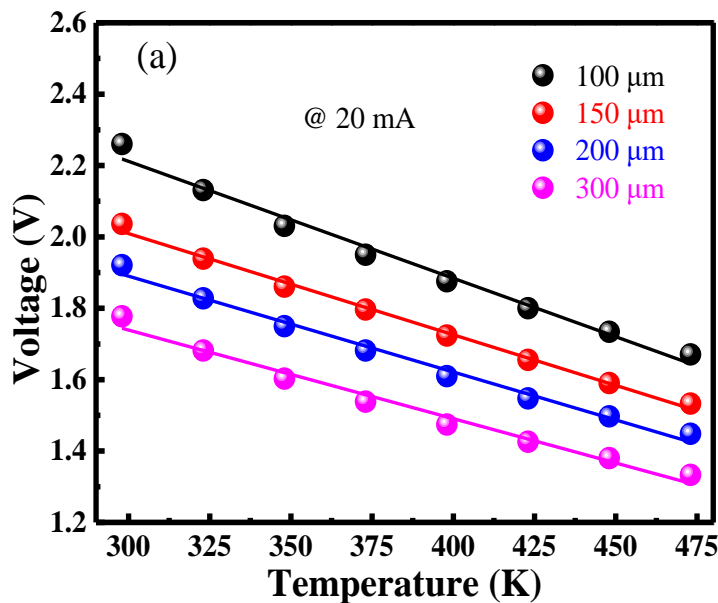
Fig. 4-2. (a)  $I$ - $V$  characteristics of a  $150\ \mu\text{m}$  diameter NiO/GaN diode temperature sensor at the fully-turn-on state, (b) the series resistance and  $n$  versus temperature, solid lines are the linear fitting. (c)  $V_F$  at current from 20 to 100 mA versus different temperatures. The temperature sensitivities are obtained by calculating the slopes of the linear fitting curves.

To evaluate the sensing ability of the pn diode, the curves of  $V_F$  versus temperatures at the currents of 20, 40, 60, 80 and 100 mA are shown in Fig. 4-2 (c). The voltage in the fully-turn-on range decreases linearly with the increasing temperature at different specific current levels. As shown in Table 2-1, the sensitivities of the NiO/GaN diode temperature sensor are  $2.84\ \text{mV/K}$  at 20 mA and  $4.29\ \text{mV/K}$  at 100 mA, which are significantly larger

than that of Ni, TiN or NiN- GaN SBD temperature sensors (the typical value is below 1.4 mV/K). From equation (4-3), the voltage drop across the  $R_s$  also has contribution on the sensitivity. By fitting the  $R_s$  versus temperature, the slope of  $dR_s/dT$  is approximately 28.7 m $\Omega$ /K with a coefficient of determination ( $R^2$ ) of 0.957. Therefore, the sensitivities caused by the  $R_s$  ( $S_{R_s}$ ) at 20, 40, 60, 80 and 100 mA are 0.56, 1.13, 1.69, 2.26 and 2.82 mV/K, respectively (Table 4-1). Then, after subtracting the contribution of the  $R_s$ , the sensitivities of the diode are approximately 2.28, 2.18, 2.06, 1.82 and 1.48 mV/K, respectively. It worth noting that the slopes of the  $V_F$ - $T$  curves are negative, indicating that the natural logarithm part in equation (4-3) is negative. The reason could be that  $I_D/A$  is smaller than 1 at a relatively small current density. Therefore, a larger current density will decrease the absolute value of  $\ln(I_D/A)$ , resulting in a relatively lower sensitivity.

Table 4-1 Sensitivity,  $R^2$  and  $S_{R_s}$  calculated from the linear fit of the experiment measurement in fully-turn-on state for a 150  $\mu\text{m}$  diameter device.

$I_D$ [mA]	$S$ [mV/K]	$R^2$	$S_{R_s}$ [mV/K]	$S-S_{R_s}$ [mV/K]
20	2.84	0.995	0.56	2.28
40	3.31	0.986	1.13	2.18
60	3.75	0.983	1.69	2.06
80	4.07	0.978	2.26	1.81
100	4.29	0.977	2.82	1.47



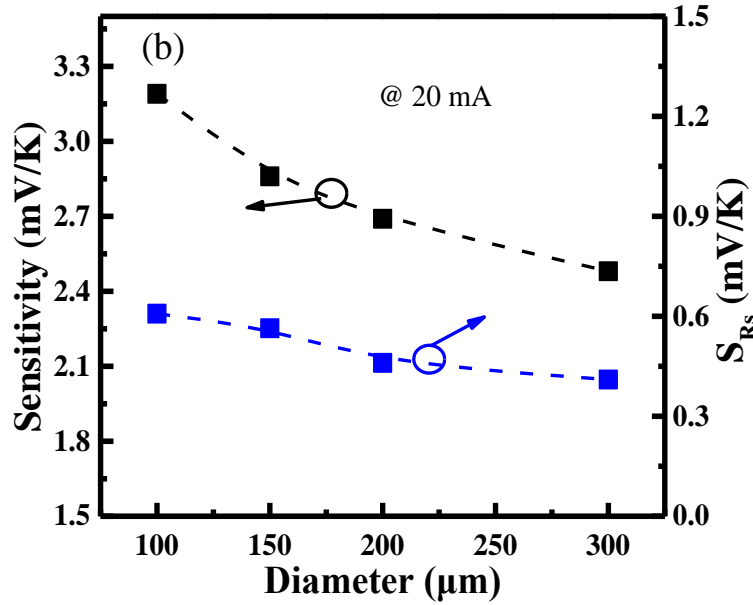


Fig 4-3. (a)  $V_F$ - $T$  curves for the device with different diameter at  $I_D$  of 20 mA, (b) sensitivity and  $S_{R_s}$  versus diameter.

Table 4-2 Sensitivity,  $R^2$  and  $S_{R_s}$  calculated from the linear fit of the experiment measurement at  $I_D$  of 20 mA for different diameter devices.

Diameter [ $\mu\text{m}$ ]	$S$ [ $\text{mV/K}$ ]	$R^2$	$S_{R_s}$ [ $\text{mV/K}$ ]	$S-S_R$ [ $\text{mV/K}$ ]	$n$ @ RT
100	3.19	0.984	0.61	2.58	2.80
150	2.84	0.995	0.56	2.28	2.23
200	2.69	0.988	0.46	2.23	2.03
300	2.48	0.979	0.41	2.07	1.80

Furthermore, the effect of the anode diameter on the sensitivity of diode was investigated. The forward voltage-temperature ( $V_F$ - $T$ ) profiles (@  $I_D=20$  mA) of the devices with anode diameters of 100, 150, 200, and 300  $\mu\text{m}$  are shown in Fig. 4-3 (a). Meanwhile, the  $dR_s/dT$  of the devices shows the similar decreasing tendency with the increasing of device diameter. Combining the slope of  $V_F$ - $T$  and the  $R_s$ - $dT$  curves (Fig. 4-3 (b)), the sensitivities of the devices decrease as the increasing anode diameter (area) (Table 4-2). Theoretically, the increase of area ( $A$ ) at a specific current level will decrease the  $I_D/A$  value while increase the absolute value (sensitivity) of  $\ln(I_D/A)$  in equation (3). Therefore, one possible reason for the decreasing sensitivity is ascribed to the decrease

of  $n$  at larger diameter. It is worth noting that the slopes of  $n$  versus  $T$  are 0.007, 0.005, 0.004 and 0.003 /K for 100, 150, 200, and 300  $\mu\text{m}$  devices, respectively. Therefore, the  $n$  values show a relatively weak temperature dependence but may play an role in the sensitivity decreasing.

(2) Sensitivity at the sub-threshold region

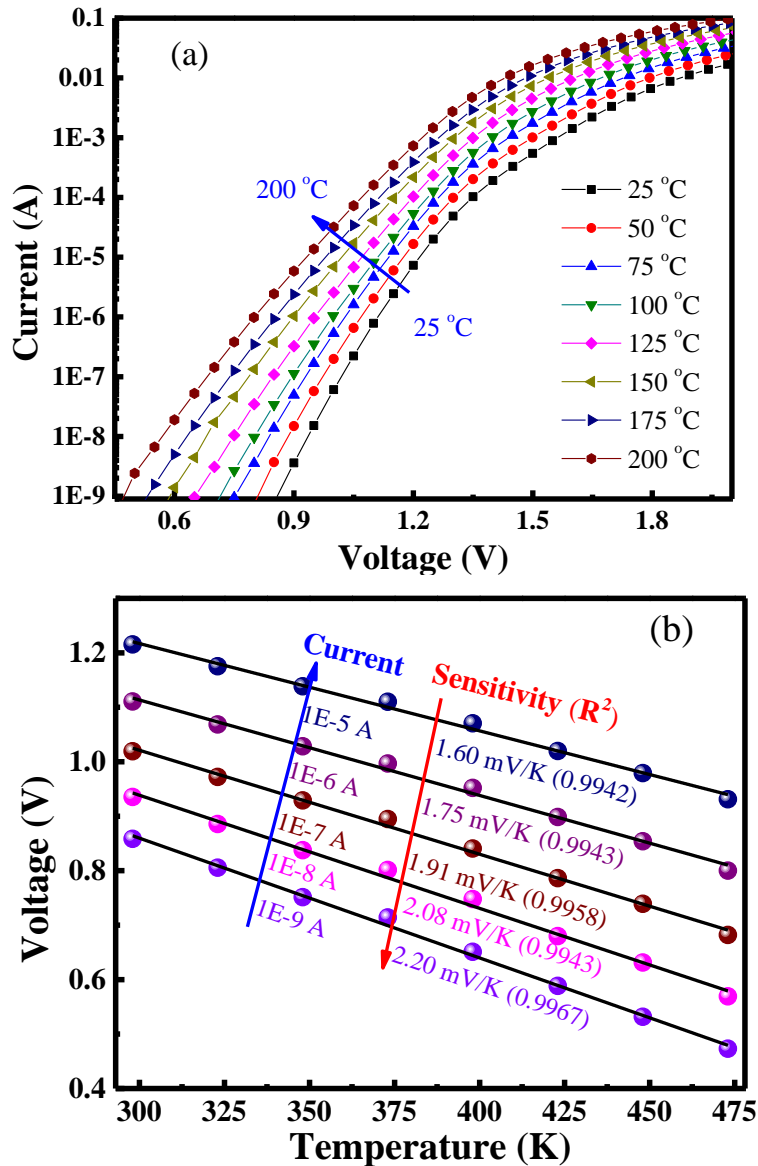


Fig. 4-4. (a) Logarithm  $I$ - $V$  curves of a 150  $\mu\text{m}$  device and (b) is the forward voltage versus temperature at sub-threshold state with specific  $I_D$  levels of 1 nA, 10 nA, 100 nA, 1  $\mu\text{A}$  and 10  $\mu\text{A}$ , respectively.

Based on the discussion above, the contribution of  $R_s$  can't be ignored in the fully-turn-

on state when the current level is relatively large. Therefore, it is necessary to investigate the sensitivity in the sub-threshold voltage region. Fig. 4-4 (a) shows the logarithmic plots of the forward bias  $I$ - $V$  curves from 25 to 200 °C. Then, the  $V_F$ - $T$  profiles at specific  $I_D$  levels of 1 nA, 10 nA, 100 nA, 1  $\mu$ A and 10  $\mu$ A are obtained, respectively, as shown in Fig. 4-4 (b). It can be seen that the sensitivity varies from 1.60 to 2.20 mV/K with the current decreasing from 10  $\mu$ A to 1 nA. The variation tendency of the sensitivity in the low current range is opposite to the fully-turn-on range. In this range, the  $I_D$  below 10  $\mu$ A will result in a vanishingly small  $S_{R_s} < 0.0002$  mV/K which can be ignored. Thus, a better linear sensitivity with  $R^2$  values larger than 0.994 is obtained.

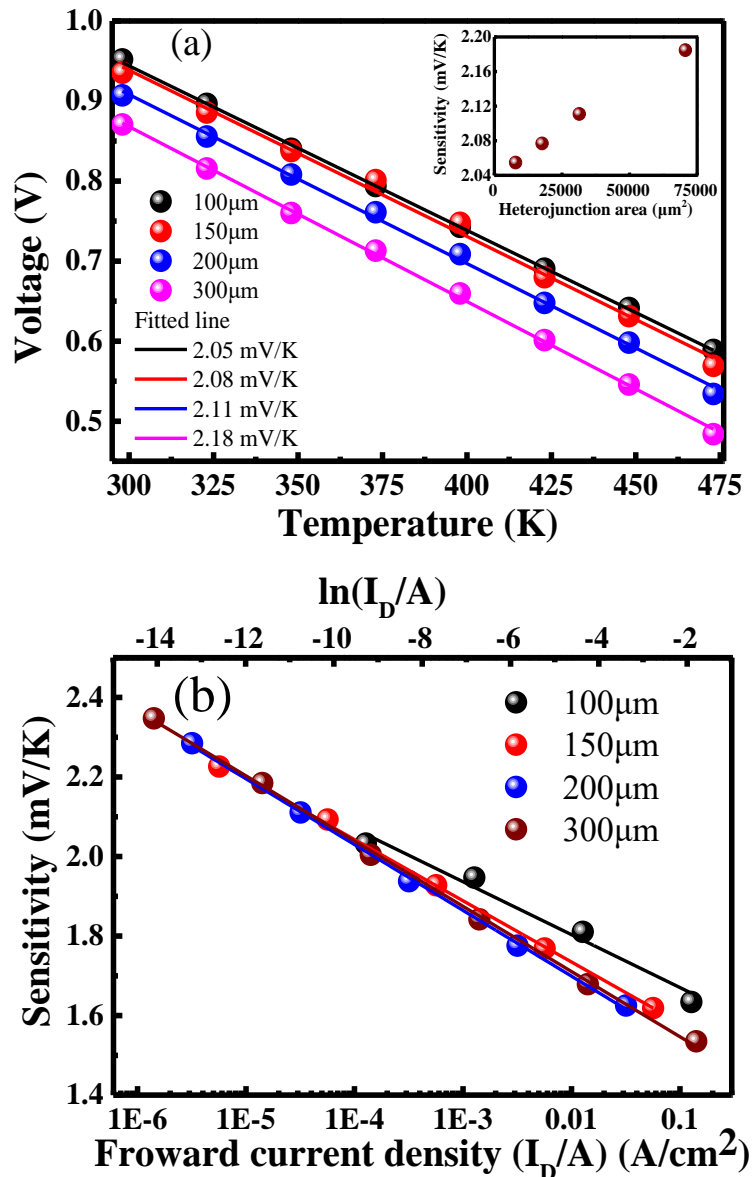


Fig. 4-5. (a) Forward voltage versus temperature for the devices with different diameters at  $I_D$  of 10

nA, (b) measured sensitivity versus  $I_D$  density of the different junction area NiO/GaN pn diode temperature sensors.

The  $V$ - $T$  profiles of the 100, 150, 200, and 300  $\mu\text{m}$  devices at  $I_D=10$  nA are shown in Fig. 4-5. From the fitted linear line, sensitivities of the 100, 150, 200, and 300  $\mu\text{m}$  devices are 2.05, 2.08, 2.11 and 2.18 mV/K, respectively, which shows a positive linear correlation with the junction area (inset of Fig. 4-5(a)). To understand this variation trend, the sensitivity versus forward current density of different devices are shown in Fig. 4-5 (b). Good linear relationship between sensitivity and  $\ln(I_D/A)$  is observed from four different diameters. Furthermore, different diameter devices are all arranged with one linear relationship. These results can also be theoretically analyzed from equation (4-4). When we ignore the  $IR_s$  and  $E_g$  [26], we can get

$$\frac{dV_F}{dT} \propto \ln \frac{I_D}{A} \quad (4-4)$$

The sensitivity versus the  $\ln(I_D/A)$  is linear, as shown in Fig. 4-5 (b). Meanwhile, the relatively larger sensitivity at a relatively lower forward current density (smaller  $I_D/A$ ) is also observed, which also accords with the results of different diameters at a given forward current of 10 nA, as shown in Fig. 4-5 (a).

### §4.3. Correlation between anode area and sensitivity for the TiN/GaN SBD temperature sensor

TiN is commonly employed as anode or gate material in GaN-based electronic devices, showing very good interface conditions and thermal stability.[27] In our previous study, [28, 29] GaN SBDs with TiN anode were fabricated and evaluated at different temperatures. Good rectifying characteristic with relatively small interface state density was confirmed in the temperature range from 25 to 200 °C. Furthermore, we also presented the feasibility of temperature sensing application. A sensitivity of approximately 1.0 mV/K was obtained which varied slightly versus current level, series resistance and diode area. [29] However, the relationship among those parameters was not evaluated in detail. It was reported that, for a p-NiO/n-GaN PND temperature sensor, the series resistance dominated the sensitivity at the fully-turn-on region, while the current density dominated the sensitivity in the sub-threshold regions.[30] Therefore, a clear

interpretation of the relationship among those parameters is also beneficial to realize a GaN SBD temperature sensor with high sensitivity.

#### §4.3.1. Device structure and fabrication

TiN anode SBD temperature sensors with four kinds of diameter were fabricated on n-GaN wafer which is similar to the NiO/GaN PND (shown in Fig. 4-6). The fabrication process is based on standard lithography process, which also follow the description in chapter 3. The TiN anode electrode was reactively sputtered using a pure Ti metal target in a N<sub>2</sub> and Ar mixed gas ambient, in which the flow rate of Ar and N<sub>2</sub> are 15 and 3 sccm, respectively [28, 29]. Finally, Ni/Au layers with thickness of 30/200 nm were deposited on all the electrode surface. In order to improve the contact property, post rapid thermal annealing (300 °C, 10 min) was conducted before device characterization. Fig. 4-6 (b) shows the optical images of the TiN SBD temperature sensors with diameters of 100, 150, 200 and 300 μm, respectively. After measuring the *I-V* property at room temperature, the sample was retrieved and the temperature was adjusted to the set temperature (stabilized for 5 min). Then, the *I-V* curve was measured again until 200 °C.

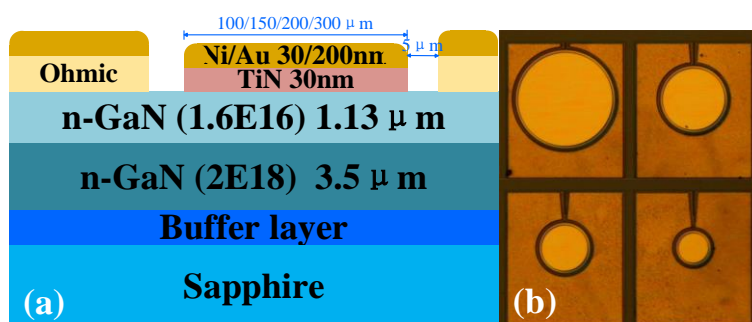


Fig. 4-6 (a) Cross-sectional schematic and (b) optical images of the TiN SBD temperature sensors with diameters of 100, 150, 200 and 300 μm, respectively.

#### §4.3.2. Theoretical modeling of the Schottky diode

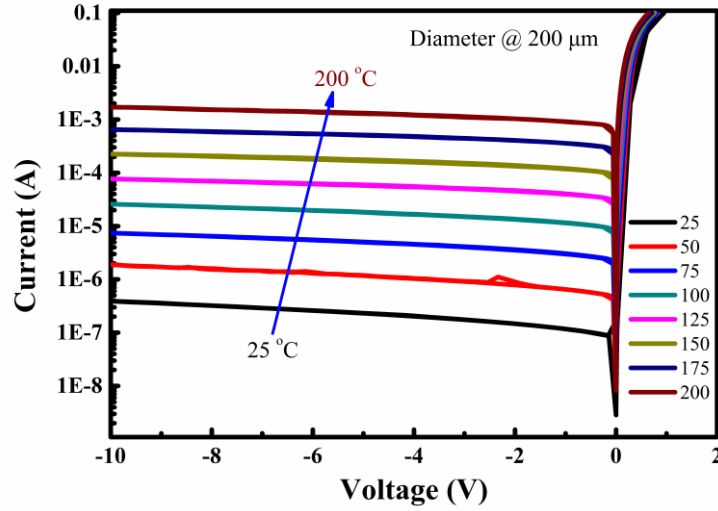


Fig. 4-7. Typical temperature-dependent  $I$ - $V$  curves under reverse and forward bias of a 200  $\mu\text{m}$  diameter device.

$I$ - $V$  characteristics of SBDs were recorded at the temperature from 25 to 200  $^{\circ}\text{C}$  with a step of 25  $^{\circ}\text{C}$ . As shown in Fig. 4-7, the typical  $I$ - $V$  curves of the device with a diameter of 200  $\mu\text{m}$  show good rectification characteristic and strong temperature dependence. The leakage current increases with the increasing temperature, implying that the thermionic emission dominates the leakage current. [25] Following the thermionic emission ( $TE$ ) theory, when  $V_F > 3kT/q$ , the forward current ( $I_D$ ) can be simplified to:

$$I_D = A_e A^* T^2 \exp\left(-\frac{q\phi_b}{kT}\right) \exp\left(\frac{qV_F - R_s I_D}{nkT}\right) \quad (4-5)$$

Where  $\phi_b$ ,  $A_e$ ,  $T$ ,  $q$ ,  $n$ ,  $k$ ,  $V$ ,  $A^*$  and  $R_s$  are the SBH, Schottky contact area, Kelvin temperature, electronic charge, ideality factor, Boltzmann constant, bias, Richardson constant and series resistance, respectively.  $R_s I_D$  is voltage drop across series resistance.

Solving for  $V_F$  yields

$$V_F = n\phi_b + \frac{nkT}{q} \left[ \ln\left(\frac{I_D}{A_e A^*}\right) - 2\ln(T) \right] + I_D R_s \quad (4-6)$$

As discussed in the previous reports, [22, 24] the effect of temperature on the nonlinear part  $\ln(T)$  of equation (4-6) is vanishingly small until very high temperature. Hence, the  $V_F$  for an idea diode at a constant current drops linearly versus the temperature.

#### §4.3.3. Characteristics and discussion

## (1) Sensitivity at the fully-turn-on state

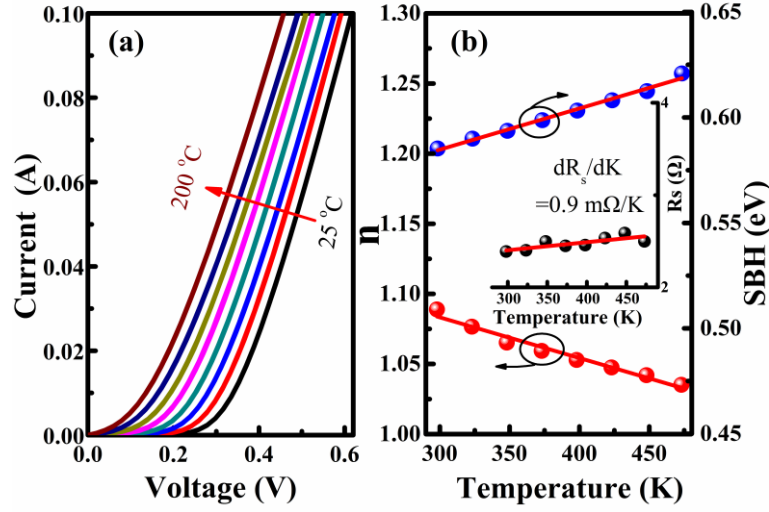


Fig. 4-8. (a)  $I$ - $V$ - $T$  curves of a 200  $\mu\text{m}$  diameter temperature sensor under forward bias. (b) The deduced  $n$  and SBH versus temperature. Inset of (b) is the variation of  $R_s$  versus temperature.

As shown in Fig. 4-8 (a), the  $I$ - $V$ - $T$  curves show a strong temperature dependence, shifting negatively with the increasing temperature. The  $n$ ,  $\varphi_b$  and  $R_s$ , calculated from the thermal emission theory, versus temperature are shown in Fig. 4-8 (b). Due to the barrier inhomogeneous behavior, the  $n$  value decreases with the increasing temperature, while the SBH increases with the increasing temperature. But both of the temperature dependence are relatively weak. It worth noting that the product of  $n$  and  $\varphi_b$  (first term in equation (4-6)) is nearly constant versus temperature due to the opposite trendence of  $\varphi_b$  and  $n$ . Besides, the  $R_s$  appears positive temperature tendency with a slope value ( $dR_s/dT$ ) of approximately 0.9  $\text{m}\Omega/\text{K}$  by fitting the  $R_s$ - $T$  curves.

$V_F$ - $T$  Plots at the given current levels of 5, 10, 15, 20, 40, 60, 80 and 100 mA are shown in Fig. 4-9, in which the dot lines are the linear fitting of experimental data based on the best-calculated linear model ( $f_L(T)$ ). [31, 32] The sensor sensitivity ( $S$ ) is calculated from the slope of the fitting line. Usually, coefficient of determination ( $R^2$ ) is used for quantifying the sensor linearity, which can be alculated by the following equation:

$$R^2 = \frac{\sum_{i=1}^m [f_L(T_i) - \overline{V_F}(T_i)]^2}{\sum_{i=1}^m [V_F(T_i) - \overline{V_F}(T_i)]^2} \quad (4-7)$$

Where,  $V_F(T_i)$  is the measured forward voltage of each temperature,  $\overline{V_F}(T_i)$  is the

average value of forward voltage,  $f_L(T_i)$  is the voltage value on the fitted line at a particular temperature ( $T_i$ ),  $m$  is the number of the temperature points and equals to 8 in this work; Therefore, the  $\sum_{i=1}^m [f_L(T_i) - \bar{V}_F(T_i)]^2$  is the regression sum of squares and  $\sum_{i=1}^m [V_F(T_i) - \bar{V}_F(T_i)]^2$  is total sum of squares.

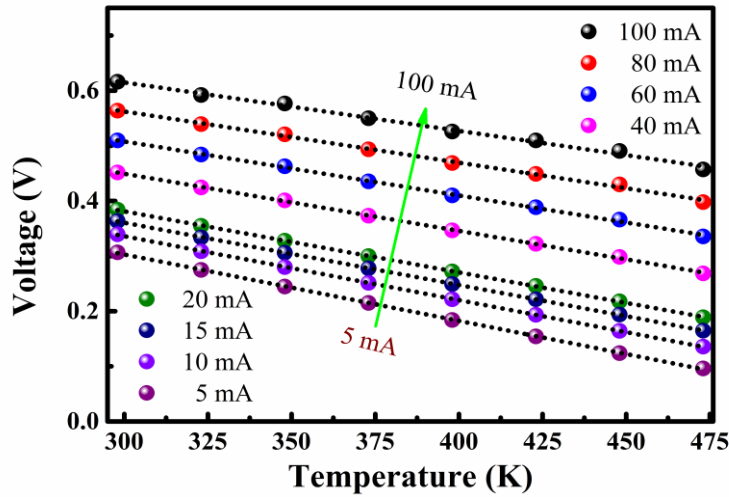


Fig. 4-9.  $V_F$ - $T$  curves at the given current levels of 5, 10, 15, 20, 40, 60, 80 and 100 mA. The dot lines are the linear fitting of experimental data.

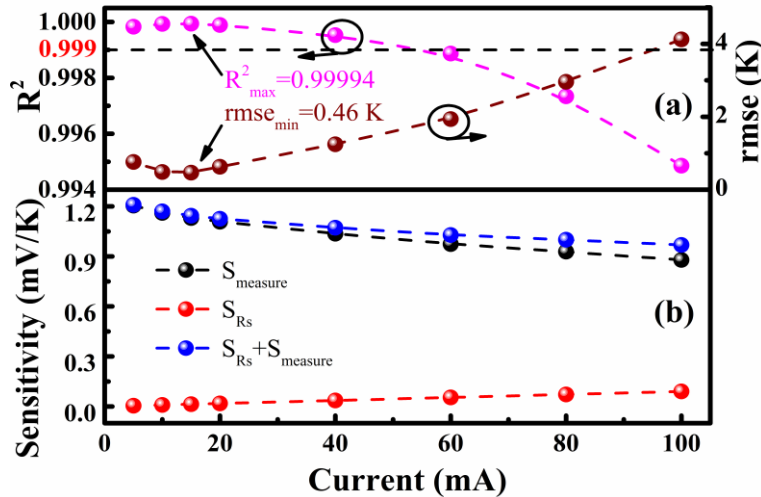


Fig. 4-10. (a)  $R^2$  and  $rmse(T)$  versus the  $I_D$  at the given current, (b)  $S_{measure}$  and  $S_{R_s}$  versus the  $I_D$  at the given current level.

The obtained  $R^2$ - $I_D$  plot for the fully-turn-on region is reported in Fig. 4-10 (a). It demonstrates that all the data show good linearity ( $R^2 > 0.9998$ ) in the relatively lower

current range (from 5 to 20 mA), showing a maximum  $R^2$  of 0.99994 at 15 mA. Although the linearity showed slight degradation in the higher current range (from 40 to 100 mA), the  $R^2$  values are still larger than 0.994.

From S. Rao report, [33] the root mean square error of temperature ( $rmse(T)$ ) is a parameter to evaluate the temperature error and linearity, which is -calculated by dividing the root mean square error of voltage drop ( $rmse(V)$ ) by the sensitivity as follows

$$rmse(T) = \frac{\sqrt{\frac{\sum_{i=1}^m [V_F(T_i) - f_L(T_i)]^2}{m}}}{S} \quad (4-8)$$

Where,  $m$  is the number of the measurement data. The plot of  $rmse(T)$  versus  $I_D$ , showing opposite trendence with  $R^2$ , is also shown in Fig. 4-10 (a). The  $rmse(T)$  is below 0.78 K in the lower current range (from 5 to 20 mA) and the minimum value is 0.48 K at 15 mA. In the higher current range (from 40 to 100 mA), the  $rmse(T)$  value incesased from 1.24 to 4.12 K. This result indicates that the sensor operates more accurately at relatively small current density.

The measured sensitivity ( $S_{measure}$ ) calculated from the slope of the  $f_L(T)$  is reported in the Fig. 4-10 (b). It shows that the  $S_{measure}$  decreases with the increasing current level in the fully-turn-on region, resulting in a maximum value of 1.25 mV/K at 5 mA. From equation (4-6), the variation of  $\ln(T)$  versus temperature in logarithmic part of  $\frac{nKT}{q} \left[ \ln\left(\frac{I_D}{A_e A^*}\right) - 2\ln(T) \right]$  is relatively small until very high temperature. Hence, the logarithmic part is dominated by  $\ln\left(\frac{I_D}{A_e A^*}\right)$ . Generally, the slopes of the  $V_F$ - $T$  curves are negative, implying that the logarithm part in equation (4-6) is smaller than zero. However, The sensitivity contribution by  $R_s$  ( $S_{R_s}$ ) equal to  $I_D * (dR_s/dT)$ , which are calculated at the given current of 5, 10, 15, 20, 40, 60, 80 and 100 mA, are 0.0045, 0.0090, 0.014, 0.018, 0.036, 0.054, 0.072 and 0.090 mV/K, respectively (Fig. 4-10 (b)). Therefore, the sensitivity contribution by  $R_s$  is positive and the effctive sensitivity of the diode is equal to the sum of  $S_{R_s}$  and  $S_{measure}$ . Finally, we can find that the sensitivity of diode decreases with the increasing current levle because of absolute value of  $\ln(I_D/A)$  decreases at the lager current level, which will result in a relatively lower sensitivity.

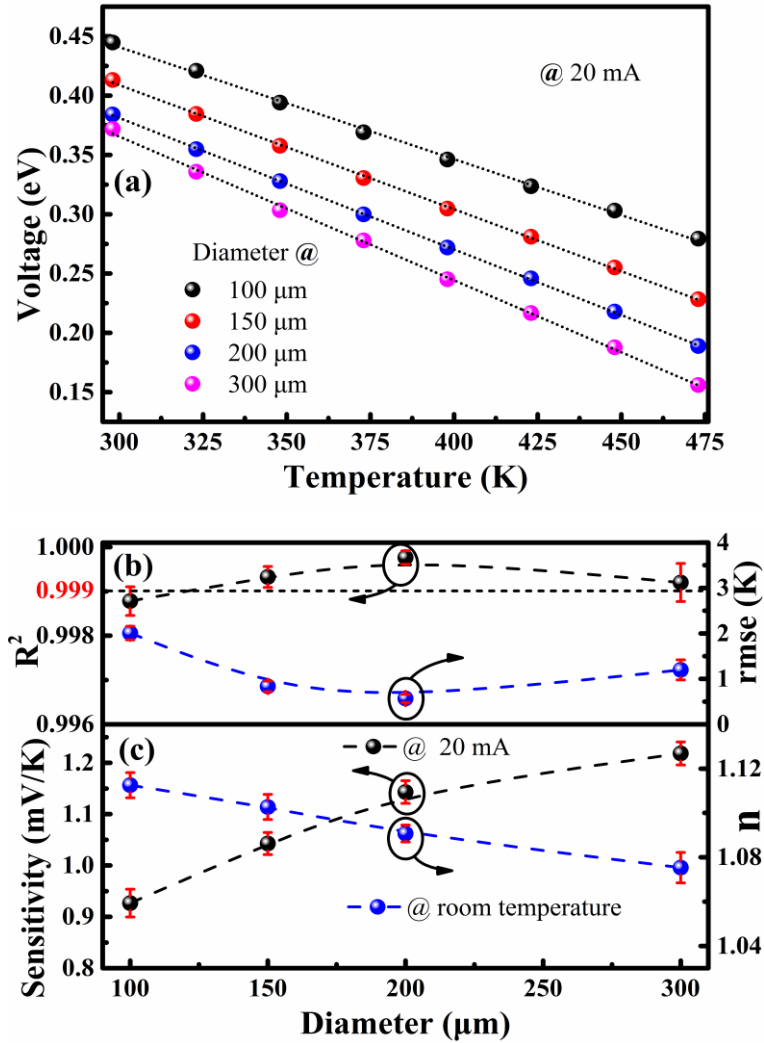


Fig. 4-11. (a) Voltage versus temperature curves of different diameter devices at the given current of 20 mA, (b)  $R^2$  and  $rmse$  of devices with different diameter at 20 mA, (c) sensitivities (@ 20 mA) and  $n$  (@ room temperature) of the different diameter devices.

Fig. 4-11 (a) shows the  $V_F$ - $T$  curves of four devices with different diameters (100, 150, 200 and 300  $\mu\text{m}$ ) under a current level of 20 mA. In order to obtain average value, 5 devices with the same size but different location were measured. As shown in Fig. 4-11 (b), high linearity was confirmed for the sensitivity, in which the average  $R^2$  value is above 0.9987 for all devices as well as low standard deviation ( $stdev < 0.0004$ ). The 200  $\mu\text{m}$  device shows highest  $R^2$  value of 0.9998 ( $\pm 0.00016$ ). Besides, the corresponding  $rmse$  of the four kinds of devices show a opposite tendency with  $R^2$ , in which the values are below 2.0 K ( $\pm 0.21$  K). Based on the discussion above, the  $dR_s/dT$  are 4.2, 2.3, 0.9 and 0.6 m $\Omega$ /K for 100, 150, 200 and 300  $\mu\text{m}$  diameter temperature sensors, respectively. Then, the  $S_{R_s}$

at 20 mA is relatively small ( $< 0.084$  mV/K) comparing with the  $S_{measure}$ . After ignoring the contribution of  $R_s$ , the sensitivity shows increasing tendency with the increasing anode diameter (Fig. 4-11 (c)), even the ideality factors  $n$  present opposite correlation with the Schottky contact area. The possible reason is that a larger diameter will increase the absolute value of  $\ln(I_D/A)$  in equation (4-6), resulting in a relatively higher sensitivity.

(2) Sensitivity at the sub-threshold region

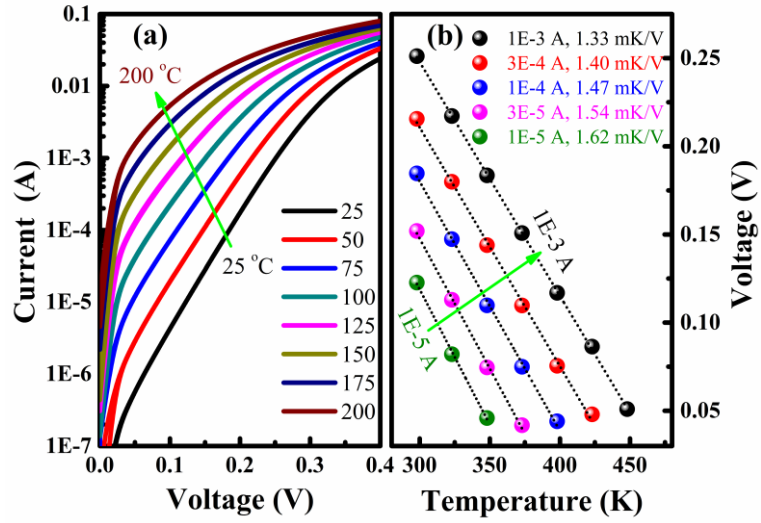


Fig. 4-12. (a) Logarithmic  $I$ - $V$ - $T$  curves of a 200  $\mu\text{m}$  diameter temperature sensor under forward bias, (b) the corresponding  $V_F$ - $T$  curves at different given current levels.

As shown in Fig. 4-12 (a),  $I$ - $V$ - $T$  curves of the 200  $\mu\text{m}$  diameter temperature sensor are plotted in logarithmic coordinates, in which negative shift was also observed with the increasing temperatures. The profiles of  $V_F$ - $T$  as well as their linear fitting lines are shown in Fig. 4-12 (b). The temperature sensitivities at the given current levels of 1E-3, 3E-4, 1E-4, 3E-5 and 1E-5 A are deduced to approximately 1.33, 1.40, 1.47, 1.54 and 1.62 mK/V, respectively. The sensitivity versus current level in the sub-threshold region appears decreasing tendency, which is in agreement with that of the fully-turn-on state.

In sub-threshold region, the contribution of  $n\varphi_b$  and  $IR_s$  (smaller than 0.005 mV/K) can be ignored. Then, we can notice that the sensitivity shows strong correlation with the current density ( $I_D/A_e$ ) as

$$\frac{dV_F}{dT} \propto \ln\left(\frac{I_D}{A_e}\right) \quad (4-9)$$

Therefore, a larger current density at a specific diameter will decrease the absolute value of  $\ln(I_D/A)$ , which will result in a lower sensitivity. On the other hand, a larger area at a given current level corresponds to lower current density and then larger sensitivity, which is accorded with the measured results in Fig. 4-13 (a). Sensitivities of 1.22 (0.007), 1.27 (0.002), 1.32 (0.012) and 1.37 (0.021) mV/K are obtained by fitting the lines of 100, 150, 200, and 300  $\mu\text{m}$  devices, respectively. This positive correlation with the diode area is consistent with equation (4-9). The relationship between sensitivities of the four diameter sensors and  $\ln(I_D/A_e)$  was further confirmed in Fig. 4-13 (b), presenting a good linear relationship with a high overall  $R^2$  of 0.986. However, the fluctuation of ideality factor for diodes with different areas causes a slight variation in slope.

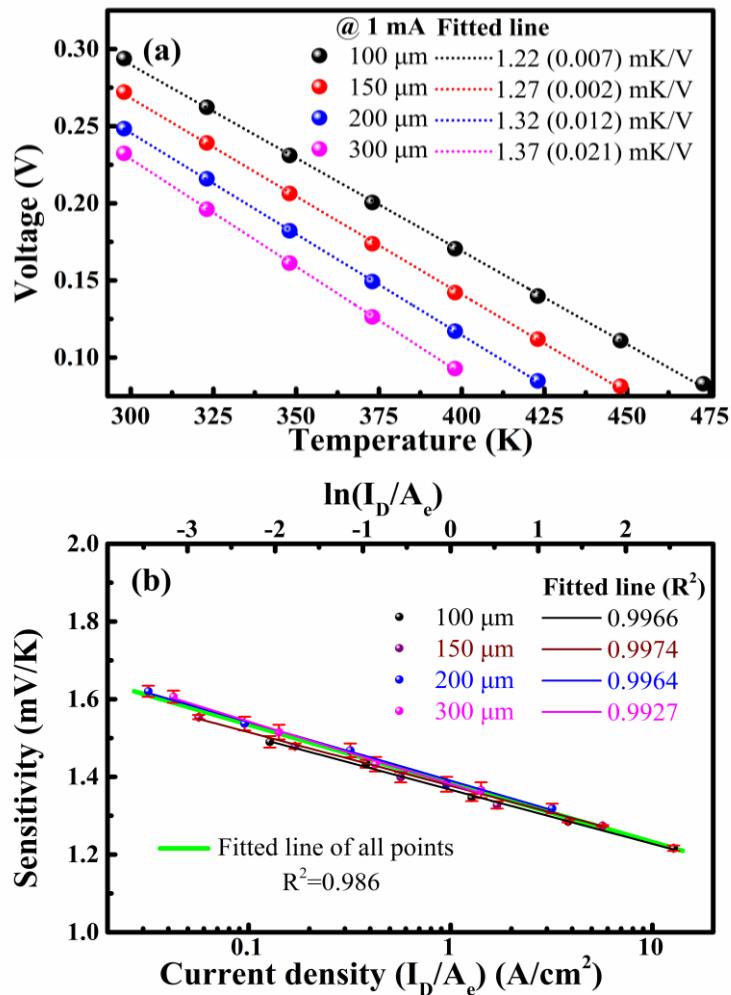


Fig. 4-13. (a) Voltage versus temperature for the devices with different diameters at the given current of 1mA, (b) measured sensitivities versus current density of different diameter TiN schottky diode temperature sensors.

(3) Reverse region

In the reverse bias region, the leakage current is temperature-dependent, implying that it is potential for sensing application. As shown in the inset of Fig. 4-14, exponential relationship was confirmed between the leakage current ( $I_r$ ) and the temperature. Consequently,  $\ln(I_r)$  versus temperature is linear. The sensitivity of  $d\ln(I_r)/dT$  ( $S_{\ln}$ ) are 0.0473, 0.0478, 0.0484, 0.0492 and 0.0499 at -10, -8, -6, -4 and -2 V, respectively, while  $R^2$  are 0.9939, 0.9934, 0.9928, 0.9923 and 0.9913 at -10, -8, -6, -4 and -2 V, respectively. Therefore,  $S_{\ln}$  shows slight decreasing tendency with the increase of reverse bias;  $R^2$  shows slight increasing tendency with the increase of reverse bias. Leakage current and  $\ln I_r$  (@ anode voltage of -6 V) versus temperature for devices with different diameters are shown in Fig. 4-14. From the fitting lines, the  $S_{\ln}$  are 48.4, 48.1, 48.9 and 48.8 mA/K, while the linearity  $R^2$  are 0.9928, 0.9930, 0.99284 and 0.9925, for devices of 100, 150, 200 and 300  $\mu\text{m}$ , respectively. This implies that the influence of the Schottky contact area is weak. The possible mechanism can be explained by TE model, in which the reverse leakage current is represented as  $I_r = A_s A^* T^2 \exp\left(-\frac{q\phi_b}{kT}\right)$ . Then, we can obtain  $\ln(I_r) \propto -\frac{q\phi_b}{kT}$ , implying the  $\ln(I_r)$  only shows direct relationship with the SBH. Therefore, the sensitivity does not depends on the Schottky contact area or bias voltage.

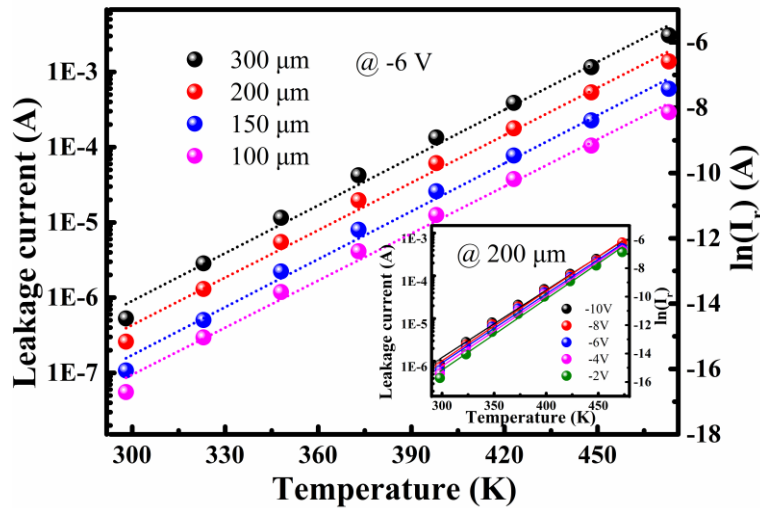


Fig. 4-14. Leakage current and  $\ln I_r$  versus temperature for the devices with different diameters. Inset is the leakage current and  $\ln(I_r)$  versus temperature of a 200  $\mu\text{m}$  diameter device at different anode voltages.

#### §4.4. High linear and near-ideal NiN/GaN SBD temperature sensor

In sections 2 and 3 of this chapter, we discuss the NiO and TiN electrode GaN SBD temperature sensor, the sensitivity shows strong dependence with forward current density. In order to avoid the self-heating effect of the device during the ambient temperature detection, the diode temperature sensor should be operated in the lower current level of sub-threshold region [22, 26]. Usually, the threshold voltage of SBD is approximately one third to half of the GaN PND, implying that the SBD temperature sensor is more suitable for in-situ monitoring during GaN device integration. However, TiN/GaN SBD temperature sensor cannot perfectly meet requisition in the lower current level of sub-threshold region due to its lower threshold voltage.

In chapter 3, NiN film deposited and used for the anode electrode material of a GaN-based SBD, which show high threshold voltage good thermal stability. These superior performances allow the NiN/GaN SBD well meet the temperature sensor requirements in sub-threshold regions.

##### §4.4.1. NiN/GaN SBD temperature sensor in sub-threshold region

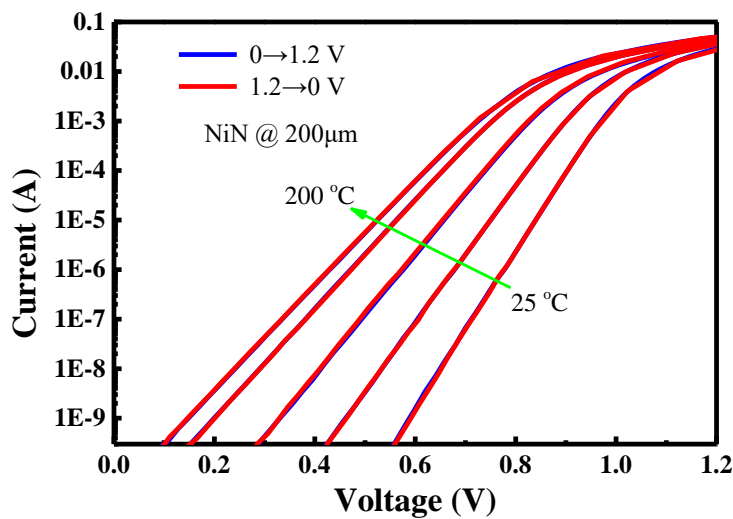


Fig. 4-15. Double sweep  $I$ - $V$ - $T$  curve of a 200  $\mu\text{m}$  NiN/GaN SBD temperature sensor

The stability is an important performance indicator of the temperature sensor, which has proved that the NiN/GaN-SBD temperature sensor has good thermal stability under variable temperature conditions in chapter 3. The retraced stability of the current at the

same temperature is also an important indicator for a temperature sensor. Double sweep  $I$ - $V$ - $T$  curve of a 200  $\mu\text{m}$  NiN/GaN SBD temperature sensor is shown in Fig. 4-15. The curve with bias sweeping from negative to positive ( $0 \rightarrow 1.2$  V) and the curve with bias sweeping from positive to negative ( $1.2 \rightarrow 0$  V) are substantially coincident, indicating that the device presents good hysteresis stability.

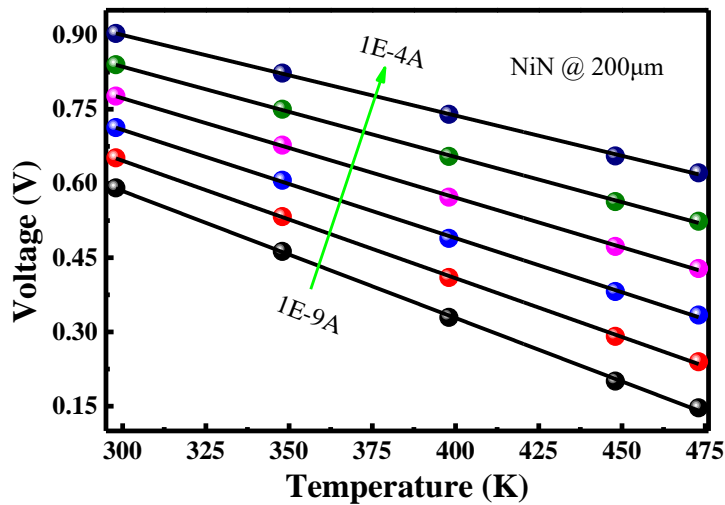


Fig.4-16. Forward voltage at given currents versus different temperature for the NiN anode SBD with a radius ( $r$ ) of 100  $\mu\text{m}$ .

Table. 4-3. Sensitivity of NiN/GaN SBD temperature sensor at given current form double sweep curves.

$I_D/A$	$0 \rightarrow 1.2$ V		$1.2 \rightarrow 0$ V	
	Sensitivity (mK/V)	$R^2$	Sensitivity (mK/V)	$R^2$
1E-4	2.543	0.9993	2.564	0.9995
1E-5	2.359	0.9995	2.374	0.9996
1E-6	2.174	0.9996	2.187	0.9994
1E-7	2.010	0.9996	2.007	0.9997
1E-8	1.823	0.9995	1.824	0.9996
1E-9	1.626	0.9996	1.627	0.9996

The profiles of  $V$ - $T$  as well as their linear fitting lines are shown in Fig. 4-16. The temperature sensitivities calculated from the fit line of the double sweep  $I$ - $V$ - $T$  curve at

the given current levels of 1E-9, 1E-8, 1E-7, 1E-6, 1E-5 and 1E-4 A are listed in Table 4-. The sensitivities of (1.2→0 V) and (0→1.2 V) show very closed value, and the sensitivity versus current level in the sub-threshold region appears decrease tendency. The linearity of the double sweep curves are presenting a good linear relationship with a high overall  $R^2$  of 0.9993.

#### §4.4.2. Theoretical sensitivity of GaN-based SBD temperature sensor

Based on the discussion in sections 2, when the  $n$  close to 1,  $n$  and  $\phi_b$  show weak and opposite temperature dependence. Thus, the first item ( $n\phi_b$ ) value is very small, and can be ignored. In sub-threshold region,  $I_D$  is less than 1E-3 A corresponding a  $S_{R_s}$  smaller than 0.001 mV/k, so the third item of equation (4-6) also can be ignored.

Thus, the equation (4-6) can be solved for:

$$\frac{dV_F}{dT} = \frac{nk}{q} \left( \ln \frac{I_D}{A_e A^* T^2} - 2 \right) \quad (4-10)$$

Solving (4-10) to:

$$\frac{dV_F}{dT} = \frac{nk}{q} \ln \frac{I_D}{A_e} - \frac{nk}{q} (\ln A^* T^2 + 2) \quad (4-11)$$

When the SBD follow the  $TE$  mode, the ideality factor  $n$  is set to 1. The second item value of equation (4-11) vary from 1.44 to 1.51 mV/K when the temperature increases from 25 to 200 °C, namely, the second item of equation (4-11) can be set a constant with a value of  $1.482 \pm 0.028$  mV/K in the temperature region from 25 to 200 °C.

Then, the ideal sensitivity of GaN-based SBD temperature sensor is:

$$\frac{dV_F}{dT} = \frac{k}{q} \ln \frac{I_D}{A_e} - 1.48 \text{ mV/K} \quad (4-12)$$

#### §4.4.3. The ideal GaN-based SBD temperature sensor

From the equation (4-12), the sensitive shows a linear relationship versus the  $\ln(I_D/A_e)$ , and this linear relationship is proven in the previous section. The theoretical curve can be calculated from equation (4-12) by substituting the  $A_e = \pi r^2$ , where,  $\pi$  is constant of 3.1416,  $r$  is radius of the anode. In our study, we employ TiN, Ni and NiN electrode to verify the theoretical sensitivity of GaN-based SBD temperature sensor, the  $I$ - $V$ - $T$  curves and  $V$ - $T$  curves (@ 25, 75, 125, 175 and 200 °C) of TiN, Ni and NiN/GaN SBD temperature

sensors are shown in Fig.4-17 and 4-18, respectively.

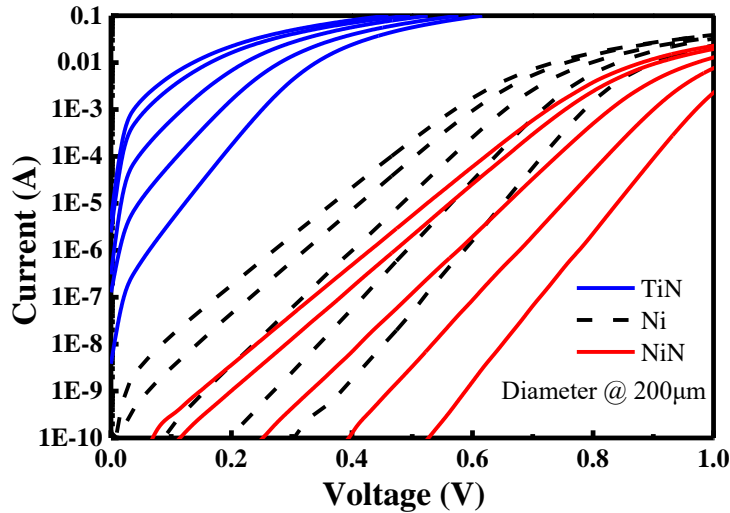


Fig. 4-17.  $I$ - $V$ - $T$  curves of TiN, Ni and NiN/GaN SBD temperature sensors.

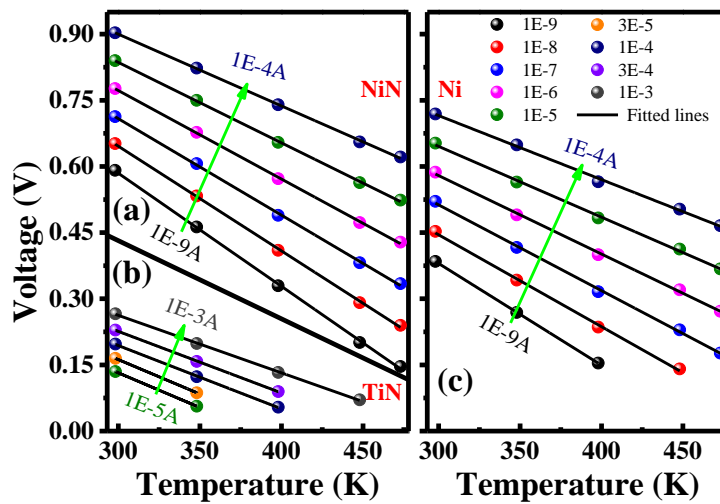


Fig.4-18. Forward voltage at given currents versus different temperature for the NiN, Ni and TiN anode SBD with a radius ( $r$ ) of 100  $\mu\text{m}$ .

The  $I$ - $V$ - $T$  curves of TiN, Ni and NiN electrode are distributed from left to right due to their different turn-on voltage. For comparing their sensitivity and linearity, we list the measured results of three types electrode in the table 4-4. Compare with the Ni and TiN/GaN SBD temperature sensor, the NiN/GaN SBD temperature sensor shows higher sensitivity and linearity at the same forward current.

Table. 4-4. Sensitivity and  $R^2$  of NiN, Ni and TiN/GaN SBD temperature sensor at given current

$I_D/A$	NiN		Ni		TiN
	Sensitivity (mK/V)	$R^2$	Sensitivity (mK/V)	$R^2$	Sensitivity (mK/V)
1E-9	2.54	0.9993	2.31	0.9995	-
1E-8	2.36	0.9995	2.08	0.9992	-
1E-7	2.17	0.9996	1.95	0.9988	-
1E-6	2.01	0.9996	1.78	0.9988	-
1E-5	1.82	0.9995	1.59	0.9985	1.62
3E-5	-	-	-	-	1.56
1E-4	1.62	0.9996	1.45	0.9981	1.47
3E-4	-	-	-	-	1.40
1E-3	-	-	-	-	1.32

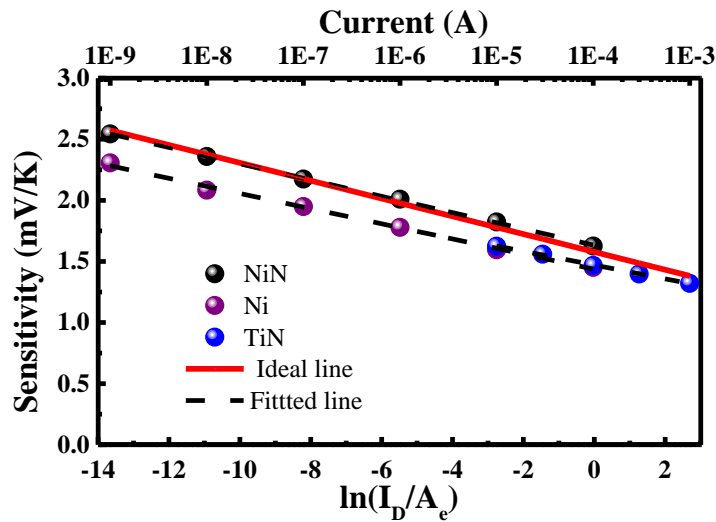


Fig. 4-19. The measured sensitivities versus  $\ln(I_D/A_e)$  and current of 200  $\mu\text{m}$  diameter NiN, Ni and TiN/GaN SBD temperature sensors and the ideal line is calculated from equation (4-12).

Fig. 4-19 shows the measured sensitivities versus  $\ln(I_D/A_e)$  and current of 200  $\mu\text{m}$  diameter NiN, Ni and TiN/GaN SBD temperature sensors. The ideal line calculated from equation (4-12) is shown with a red line, which is closed to the fitted line of NiN/GaN SBD temperature sensor. This approximation to the theoretical value is more obvious at lower current, this also mean that the TE mode dominate in the NiN/GaN SBD. The measured sensitivity of Ni/GaN SBD is smaller than the theoretical value, this cause by

there are other activation model such as phonon-assisted tunneling also contribute to the current [34]. For the TiN/GaN temperature sensor, the narrow sub-threshold range case by lower SBH and lower turn-on voltage, which lead to the measured sensitivity deviate the theoretical value.

#### §4.5. Conclusion

The temperature-sensitive p-NiO/n-GaN diodes were investigated extensively by varying the device diameter and current level. It is demonstrated that the series resistance and ideality factor dominate the sensitivity at the fully-turn-on state. After subtracting the component of series resistance, the sensitivity decreases with the increased device diameters, which is ascribed to the relative ideality factor. A maximum sensitivity of 2.58 mV/K was achieved for the device with a diameter of 100  $\mu\text{m}$  (at 20 mA). While for the sub-threshold state, a good linear relationship between sensitivity and the corresponding current density has been observed for devices with different diameters. A low current density is corresponding to the high sensitivity. The NiO/GaN diodes presenting good thermal stability and linearity from 25 to 200  $^{\circ}\text{C}$  are promising candidates for temperature sensing application.

TiN anode GaN SBDs were also fabricated with different diameters for temperature sensor application. The  $I$ - $V$ - $T$  curves shift regularly versus temperature with a slight barrier inhomogeneous behavior. Taking account of the contribution of series resistance and barrier inhomogeneous, the sensitivity increases with the increasing diode diameter in the fully-turn-on region. A maximum sensitivity of 1.22 mV/K was achieved from the 300  $\mu\text{m}$  diameter device at the given current of 20 mA. In the sub-threshold region, the sensitivity and current density shows a good linear relationship, in which the low sensitivity is corresponding to a high current density. Based on those result, it demonstrates that the sensitivity of a Schottky barrier diode is correlated with the current density ( $I_D/A$ ). The leakage current in the reverse bias region versus temperature ( $S_{I_n}$ ) also presents a sensitivity of approximately 48 mA/K and shows weak dependence on the diameter and bias voltage.

While in the sub-threshold region, a good linear relationship between sensitivity and the corresponding current density has been observed for a 200 $\mu\text{m}$  diameter NiN/GaN SBD temperature sensor. A low current density is corresponding to the high sensitivity.

Based on those result, it demonstrates that the sensitivity of a Schottoky barrier diode is correlated with the current density ( $I_D/A$ ).

Finally, the theoretical sensitivity of GaN-based SBD temperature sensor was calculated by the TE model. By comparing whih TiN, Ni and NiN electrode GaN SBD temperature sensor, the NiN electrode device shows a near-ideal sensitivity of a GaN SBD temperature sensor.

## §4.6. References

- [1] Pristavu G, Brezeanu G, Badila M, et al. A model to non-uniform Ni Schottky contact on SiC annealed at elevated temperatures[J]. *Applied Physics Letters*, 2015, 106(26): 261605.
- [2] Rao S, Pangallo G, Della Corte F G. Highly linear temperature sensor based on 4H-silicon carbide pin diodes[J]. *IEEE Electron Device Letters*, 2015, 36(11): 1205-1208.
- [3] Dinh T, Nguyen N T, Dao D V. Desirable Features for High-Temperature SiC Sensors[M]//*Thermoelectrical Effect in SiC for High-Temperature MEMS Sensors*. Springer, Singapore, 2018: 43-53.
- [4] Bahat-Treidel E, Hilt O, Zhytnytska R, et al. Fast-switching GaN-based lateral power Schottky barrier diodes with low onset voltage and strong reverse blocking[J]. *IEEE Electron Device Letters*, 2012, 33(3): 357-359.
- [5] Vetury R, Zhang N Q, Keller S, et al. The impact of surface states on the DC and RF characteristics of AlGaIn/GaN HFETs[J]. *IEEE Transactions on Electron Devices*, 2001, 48(3): 560-566.
- [6] Müller A, Giangu I, Stavrinidis A, et al. Sezawa propagation mode in GaN on Si surface acoustic wave type temperature sensor structures operating at GHz frequencies[J]. *IEEE Electron Device Letters*, 2015, 36(12): 1299-1302.
- [7] Lovesey S W. Diffraction and absorption of x-rays by 3d transition ions: the process[J]. *Journal of Physics: Condensed Matter*, 1998, 10(11): 2505.
- [8] Hüfner S. Electronic structure of NiO and related 3d-transition-metal compounds[J]. *Advances in Physics*, 1994, 43(2): 183-356.
- [9] Kamal H, Elmaghraby E K, Ali S A, et al. Characterization of nickel oxide films deposited at different substrate temperatures using spray pyrolysis[J]. *Journal of crystal growth*, 2004, 262(1): 424-434.
- [10] Mahmoud S A, Akl A A, Kamal H, et al. Opto-structural, electrical and electrochromic properties of crystalline nickel oxide thin films prepared by spray pyrolysis[J]. *Physica B: Condensed Matter*, 2002, 311(3): 366-375.
- [11] Park Y R, Kim K J. Sol-gel preparation and optical characterization of NiO and Ni<sub>1-x</sub>Zn<sub>x</sub>O thin films[J]. *Journal of Crystal Growth*, 2003, 258(3): 380-384.
- [12] Chigane M, Ishikawa M. Electrochromic properties of nickel oxide thin films

- prepared by electrolysis followed by chemical deposition[J]. *Electrochimica acta*, 1997, 42(10): 1515-1519.
- [13] Martini M, Brito G E S, Fantini M C A, et al. Electrochromic properties of NiO-based thin films prepared by sol-gel and dip coating[J]. *Electrochimica Acta*, 2001, 46(13): 2275-2279.
- [14] Ferreira F F, Tabacniks M H, Fantini M C A, et al. Electrochromic nickel oxide thin films deposited under different sputtering conditions[J]. *Solid State Ionics*, 1996, 86: 971-976.
- [15] Hotový I, Huran J, Spiess L, et al. Preparation and characterization of NiO thin films for gas sensor applications[J]. *Vacuum*, 2000, 58(2): 300-307.
- [16] Hotovy I, Huran J, Spiess L, et al. Preparation of nickel oxide thin films for gas sensors applications[J]. *Sensors and Actuators B: Chemical*, 1999, 57(1): 147-152.
- [17] Sasi B, Gopchandran K G, Manoj P K, et al. Preparation of transparent and semiconducting NiO films[J]. *Vacuum*, 2002, 68(2): 149-154.
- [18] Ohta H, Kamiya M, Kamiya T, et al. UV-detector based on pn-heterojunction diode composed of transparent oxide semiconductors, p-NiO/n-ZnO[J]. *Thin Solid Films*, 2003, 445(2): 317-321.
- [19] Ohta H, Kamiya M, Kamiya T, et al. UV-detector based on pn-heterojunction diode composed of transparent oxide semiconductors, p-NiO/n-ZnO[J]. *Thin Solid Films*, 2003, 445(2): 317-321.
- [20] Li L, Chen J, Liu Z, et al. Fast and slow interface traps in transparent NiO gated AlGaN/GaN heterostructure field-effect transistors[J]. *Applied Surface Science*, 2019, 475: 1043-1047.
- [21] Li L, Wang X, Liu Y, et al. NiO/GaN heterojunction diode deposited through magnetron reactive sputtering[J]. *Journal of Vacuum Science & Technology A: Vacuum, Surfaces, and Films*, 2016, 34(2): 02D104.
- [22] Madhusoodhanan S, Sandoval S, Zhao Y, et al. A highly linear temperature sensor using GaN-on-SiC heterojunction diode for high power applications[J]. *IEEE Electron Device Letters*, 2017, 38(8): 1105-1108.
- [23] Sharma B L, Purohit R K. *Semiconductor heterojunctions*[M]. Elsevier, 2015.
- [24] Santra S, Guha P K, Ali S Z, et al. SOI diode temperature sensor operated at ultra high temperatures-a critical analysis[C]//*SENSORS*, 2008 IEEE. IEEE, 2008: 78-81.

- [25] Sze S M, Ng K K. Physics of semiconductor devices[M]. John Wiley & sons, 2006.
- [26] Chandrashekhar M V S, Duggirala R, Spencer M G, et al. 4 H SiC betavoltaic powered temperature transducer[J]. Applied Physics Letters, 2007, 91(5): 053511.
- [27] Ponon N K, Appleby D J R, Arac E, et al. Effect of deposition conditions and post deposition anneal on reactively sputtered titanium nitride thin films[J]. Thin Solid Films, 2015, 578: 31-37.
- [28] Li L, Chen J, Gu X, et al. Temperature sensor using thermally stable TiN anode GaN Schottky barrier diode for high power device application[J]. Superlattices and Microstructures, 2018, 123: 274-279.
- [29] Li L, Kishi A, Shiraishi T, et al. Electrical properties of TiN on gallium nitride grown using different deposition conditions and annealing[J]. Journal of Vacuum Science & Technology A: Vacuum, Surfaces, and Films, 2014, 32(2): 02B116.
- [30] Li X, Pu T, Zhang T, et al. p-NiO/n-GaN heterostructure diode for temperature sensor application[J]. IEEE Sensors Journal, 2019.
- [31] Nagelkerke N J D. A note on a general definition of the coefficient of determination[J]. Biometrika, 1991, 78(3): 691-692.
- [32] Pangallo G, Rao S, Adinolfi G, et al. Power MOSFET Intrinsic Diode as a Highly Linear Junction Temperature Sensor[J]. IEEE Sensors Journal, 2019, 19(23): 11034-11040.
- [33] Rao S, Pangallo G, Della Corte F. Integrated Amorphous Silicon pin Temperature Sensor for CMOS Photonics[J]. Sensors, 2016, 16(1): 67.
- [34] Wang T T, Wang X, Li X B, et al. Temperature-Dependent Characteristics of GaN Schottky Barrier Diodes with TiN and Ni Anodes[J]. Chinese Physics Letters, 2019, 36(5): 057101.

## Chapter 5: NiN Gate AlGa<sub>N</sub>/Ga<sub>N</sub> HFETs

### §5.1. Introduction

In the past years, due to their wide band gap, low intrinsic carrier concentration, high electronic mobility, and high saturation velocity, Ga<sub>N</sub> and its related AlGa<sub>N</sub>/Ga<sub>N</sub> heterostructure Field-effect transistors (HFETs) have been extensively investigated for application in the high-power, high-frequency, and high-temperature areas [1-3]. Meanwhile, researchers always devote their attention to improve performance of the HFETs and related devices [1, 4, 5]. However, the high performance HFETs devices are not only affected by the high quality epitaxial wafers, but also affected by the performance of the metal contacts as well as the gate materials.

For the gate material, it is required to meet low leakage current and better thermal stability. In now days, metals such as Cu, Ni and NiN are usually used for gate materials in the HFETs [6-9], in which Ni is the most conventional gate metal due to its lower cost and higher SBH. However, Ni is easily occurred reactive interface reaction in the Ni/Ga<sub>N</sub> contact result in the instability after annealing [10, 11]. In chapter 3, we demonstrated the NiN synthesized by optimizing the sputtering condition showed high SBH and low leakage current used as Schottky electrode on the n-Ga<sub>N</sub>, but there are few reports about the application on HFETs.

In this chapter, AlGa<sub>N</sub>/Ga<sub>N</sub> HFETs with NiN electrode were prepared by magnetron reactive sputtering in an ambient of Ar and N<sub>2</sub> mixture gas in which the P(N<sub>2</sub>) is kept at 0.069 Pa. Comparing with the convention Ni-gated HFETs, the NiN-gate HFETs have lower gate leakage current and larger ON/OFF ratio. In addition, the NiN-gated HFETs show the good thermal stability.

### §5.2. Device structure and fabrication

The epitaxial layers of AlGa<sub>N</sub>/Ga<sub>N</sub> used in this experiment were grown by MOCVD on a 4 inch silicon substrate, including a 2 nm i-Ga<sub>N</sub> surface layer, a 25 nm AlGa<sub>N</sub> barrier layer, a 2 μm i-Ga<sub>N</sub> channel layer and a nucleation layer.

The device fabrication process was based on a standard photolithography technology

(Fig.5-1 (a)). At the beginning of fabrication, the GaN wafers were cleansed by SPM ( $\text{H}_2\text{SO}_4:\text{H}_2\text{O}_2=4:1$ ), acetone and pure water were used for removing the organic and inorganic matters. Firstly, the devices were isolated by inductively coupled plasma (ICP) etching with  $\text{SiCl}_4$  gas. Then, the ohmic contact was deposited on the surface of the wafers with Ti/Al/Ti/Au (50/200/40/40 nm) by reactive sputtering. After the lift-off process, the wafers were annealed at  $850^\circ\text{C}$  for 3 minutes in  $\text{N}_2$  ambient to form the ohmic contacts. Before the deposition of the gate, the wafers were soaked in diluted HCl with 5 min for removing the possible oxide layer on the wafer surface formed by the  $\text{O}_2$  plasma ashing. Then, gate was fabricated using NiN /Au (100/30 nm), in which the gate length and width are 4 and  $50\ \mu\text{m}$ , respectively. For comparison, we also fabricated conventional Ni-gate HFET samples with the same structure.

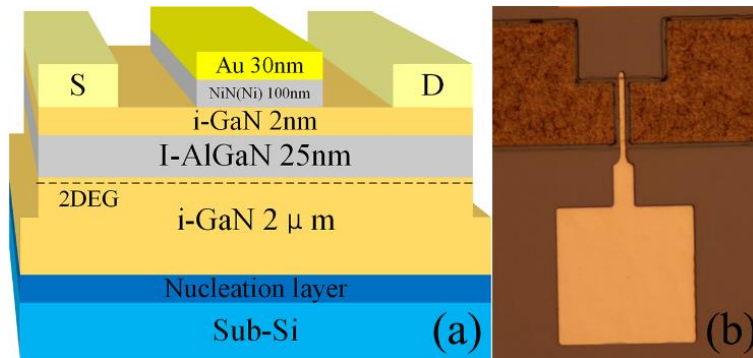


Fig. 5-1. The structure schematic (a) and micrograph (b) of HFET.

### §5.3. Devices performances

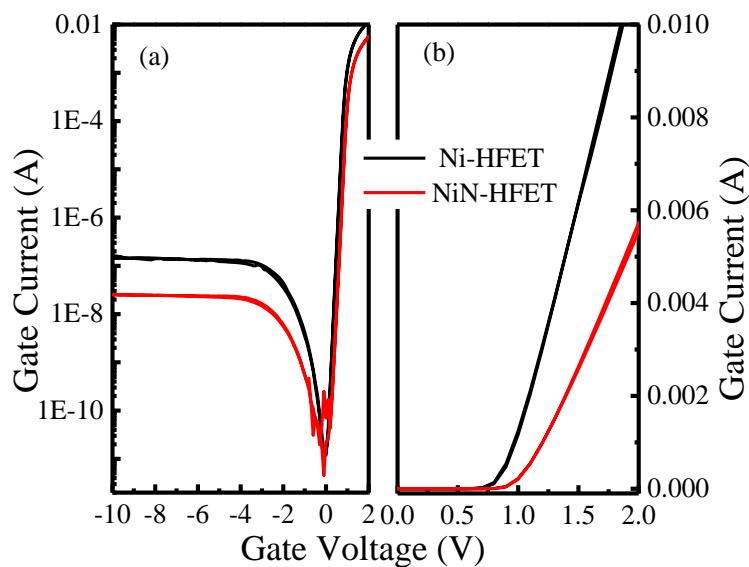


Fig. 5-2. The gate leakage characteristics (a) and forward characteristics (b) of the Ni- and NiN-gated AlGa<sub>N</sub>/Ga<sub>N</sub>.

The gate leakage characteristics were measured on the HFETs from -10 to 2 V. In the reverse bias region as shown in Fig 5-2(a), the leakage current of the NiN-gated HFET is one order magnitudes lower compared with the Ni-gated HFET. In addition, as shown in the Fig 5-2(b), the gate turn-on voltage has positive shift, from 0.8V for Ni-gate HFET to 1.1 V for NiN-gate HFET. The positive shift of gate turn-on voltage is owing to the larger work function of the Ni<sub>3</sub>N material.

The Fig. 5-3 shows the output characteristics of the NiN and NiN-gated HEFM, and the gate voltage is swept from -5 to +2 V. Both devices show the normal drain current-voltage characteristics, and compared with the Ni-gate HFETs the NiN-gate HFETs have a larger drain current.

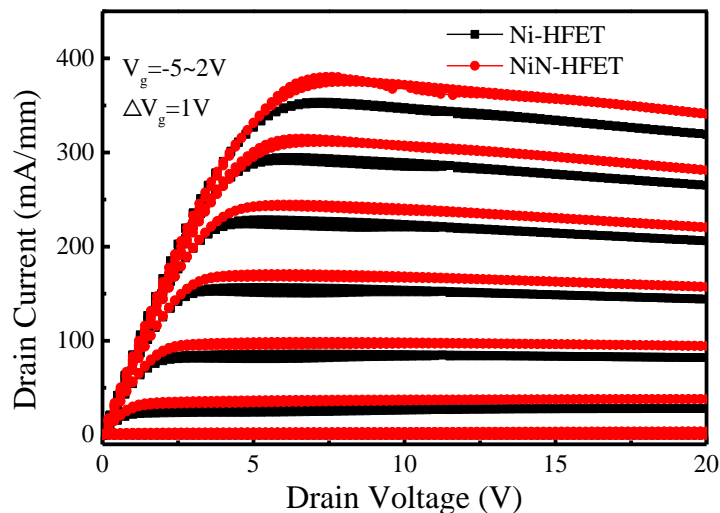


Fig. 5-3. The output characteristics of the Ni- and NiN- gated AlGa<sub>N</sub>/Ga<sub>N</sub> HFETs.

As shown in Fig. 5-4, the transconductance and the drain current of the NiN-gated HFETs are higher than that of the Ni-gated HFETs. In addition, The threshold voltage (determined at drain current of 1mA/mm) of Ni and NiN HFET are about -3.9 and -4.1 V at the drain voltage of 10 V, respectively, which is anomaly with the theory of higher barrier height of gate corresponding higher threshold voltage. [12, 13] This anomaly phenomenon is mainly due to the poor wafer uniformity, even though small positive threshold voltage might have happened owing to the higher barrier height of NiN gate

[21].

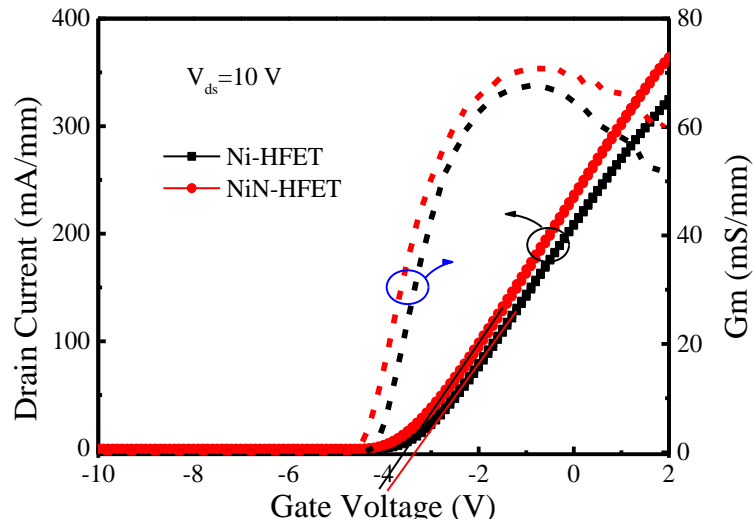


Fig. 5-4. The transfer characteristics of the Ni- and NiN- gated AlGaIn/GaN HFETs.

Fig. 5-5 (a) shows the subthreshold slopes and ON/OFF drain current ratios of Ni- and NiN-gated HFET. Due to the decreased gate leakage, the ON/OFF ratio of drain current for NiN-gated HFET (approximately  $10^7$ ) increased two order of magnitude compare with Ni-gated HFET (approximately  $10^5$ ). The subthreshold swing (SS) values of NiN-gated and Ni-gated HFETs are 106 and 176 mV/dec, respectively. The smaller SS value for NiN-gated HFET imply that less interfacial state density existed in the NiN-gated HFET and the improved trapping behavior at the interface promote the gate control ability.

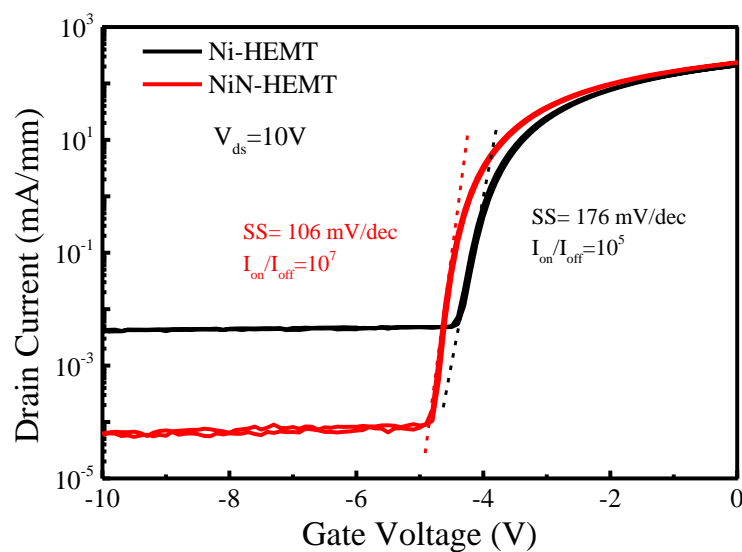


Fig. 5-5. The subthreshold slopes and ON/OFF drain current ratios of Ni- and NiN-gated HFET.

For evaluating the thermal stability of the gate leakage current, the devices were heated from 25 °C to 175 °C by the step of 25 °C for measuring the characterization which are shown in Fig. 5-6 (a). The NiN-gated HFET shows good rectification characterization at all temperatures. The leakage current in the reverse voltage region shows strong temperature dependence, in which the leakage current is increased with increasing of the temperate. Fig. 5-6 (b) shows the Arrhenius plots of leakage of NiN device. The and the gate leakage current at -10 V shows a linearity vs. the 1000/T, in which the increased rate of leakage current at -10V is about  $3 \times 10^{-10}$  A/K from 25 °C to 175 °C. After the measurement at 175 °C, the NiN-gated HFET had no obvious degeneration. In addition, after the measurement at 175 °C, we found the Ni-gated HFET had degeneration, in which the gate leakage current degenerated about 1 order of magnitude this result is also consistence with our previous report. [14]

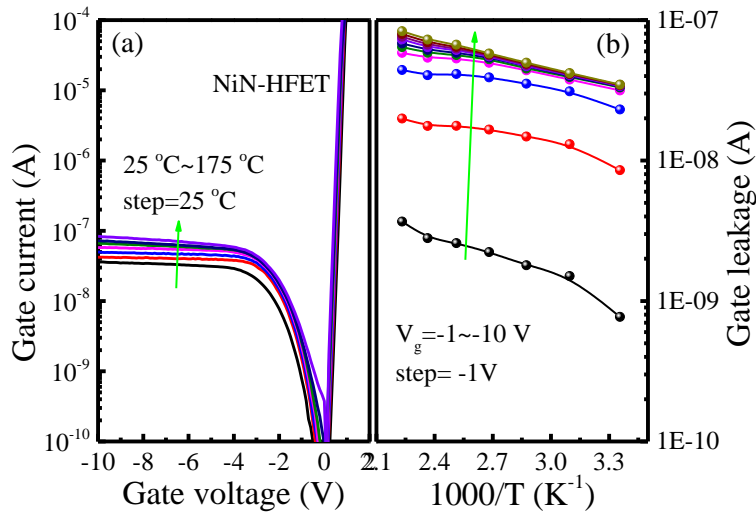


Fig. 5-6. (a) Temperature dependent gate leakage and Arrhenius plots gate leakage of NiN-HFET

The Poole-frenkel (*FP*) emission model is often used to explain the leakage current mechanism, which is given by:

$$\begin{aligned}
 J_{PF} &= qn_0\mu E_n \exp\left[-\frac{q}{kT}\left(\phi_b - \sqrt{\frac{qE}{\pi\epsilon_n}}\right)\right] \\
 &\propto E \exp\left(\frac{q}{kT}\sqrt{\frac{qE}{\pi\epsilon_n}} - \frac{q\phi_b}{kT}\right) \\
 &\propto V \exp\left(a\frac{\sqrt{V}}{T} - \frac{q\phi_b}{kT}\right)
 \end{aligned} \tag{5-1}$$

where,  $J_{PF}$  is the Poole-frenkel current density,  $n_0$ ,  $\mu$ ,  $\Phi_b$ ,  $E_n$ ,  $q$ ,  $k$  and  $T$  are carrier density, effective carrier mobility, the trap state depth, the applied electric field, elementary charge, the Boltzmann constant and the temperature, respectively. As shown in Fig 5-7, the plots of  $\ln(I/V)$  vs. reverse voltage at different temperatures present a good linear relationship, implying the conduction mechanism is most likely due to Poole-frenkel emission. [15]

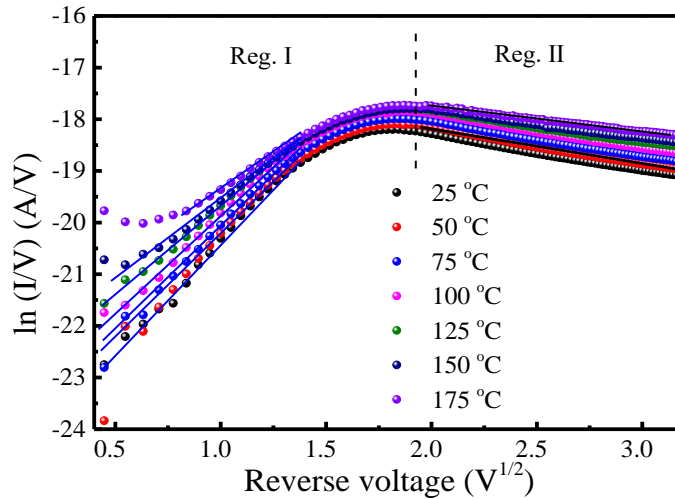


Fig. 5-7 Plots of  $\ln(I/V)$  vs. reverse voltage at different temperatures.

## §5.4. Conclusion

We have fabricated NiN-gated AlGaIn/GaN HFETs by magnetron reactive sputtering with a Ni target in an ambient Ar and N<sub>2</sub> mixture gas. Gate leakage current characteristics showed that the reverse leakage current of NiN-gated HFETs was approximately reduced by one order of magnitude and the ON/OFF drain current ratio increased two order of magnitudes comparing with the conventional Ni-gated HFETs. The temperature-dependent gate leakage current-voltage characteristics demonstrate that the NiN-gated HFETs have better thermal stability.

## §5.5. References

- [1] Li L, Kishi A, Shiraishi T, et al. Evaluation of a gate-first process for AlGa<sub>N</sub>/Ga<sub>N</sub> heterostructure field-effect transistors[J]. Japanese Journal of Applied Physics, 2013, 52(11S): 11NH01.
- [2] Keller S, Wu Y F, Parish G, et al. Gallium nitride based high power heterojunction field effect transistors: Process development and present status at UCSB[J]. IEEE Transactions on Electron Devices, 2001, 48(3): 552-559.
- [3] A. Podolska, M. Kocan, A. M. G. Cabezas, T. D. Wilson, G. A. UmanaMembreno, B. D. Nener, G. Parish, S. Keller, and U. K. Mishra: Appl. Phys. Lett. 97 (2010) 012108
- [4] Angelov I, Bengtsson L, Garcia M. Extensions of the Chalmers nonlinear HEMT and MESFET model[J]. IEEE Transactions on Microwave Theory and Techniques, 1996, 44(10): 1664-1674.
- [5] Wang L, Li L, Xie T, et al. Threshold voltage tuning in AlGa<sub>N</sub>/Ga<sub>N</sub> HFETs with p-type Cu<sub>2</sub>O gate synthesized by magnetron reactive sputtering[J]. Applied Surface Science, 2018, 437: 98-102.
- [6] Feng Q, Li L M, Hao Y, et al. The improvement of ohmic contact of Ti/Al/Ni/Au to AlGa<sub>N</sub>/Ga<sub>N</sub> HEMT by multi-step annealing method[J]. Solid-State Electronics, 2009, 53(9): 955-958.
- [7] Lin Y C, Chang C H, Li F M, et al. Evaluation of TiN/Cu gate metal scheme for AlGa<sub>N</sub>/Ga<sub>N</sub> high-electron-mobility transistor application[J]. Applied Physics Express, 2013, 6(9): 091003.
- [8] Soltani A, Rousseau M, Gerbedoen J C, et al. High performance TiN gate contact on AlGa<sub>N</sub>/Ga<sub>N</sub> transistor using a mechanically strain induced P-doping[J]. Applied physics letters, 2014, 104(23): 233506.
- [9] Ao J P, Kikuta D, Kubota N, et al. Copper gate AlGa<sub>N</sub>/Ga<sub>N</sub> HEMT with low gate leakage current[J]. IEEE Electron Device Letters, 2003, 24(8): 500-502.
- [10] Guo J D, Pan F M, Feng M S, et al. Schottky contact and the thermal stability of Ni on n - type Ga<sub>N</sub>[J]. Journal of applied physics, 1996, 80(3): 1623-1627.
- [10] Li L, Chen J, Gu X, et al. Temperature sensor using thermally stable TiN anode Ga<sub>N</sub> Schottky barrier diode for high power device application[J]. Superlattices and Microstructures, 2018, 123: 274-279.

- [12] Cai Y, Zhou Y, Lau K M, et al. Control of threshold voltage of AlGa<sub>N</sub>/Ga<sub>N</sub> HEMTs by fluoride-based plasma treatment: From depletion mode to enhancement mode[J]. IEEE Transactions on Electron Devices, 2006, 53(9): 2207-2215.
- [13] Ao J P, Kikuta D, Kubota N, et al. Copper gate AlGa<sub>N</sub>/Ga<sub>N</sub> HEMT with low gate leakage current[J]. IEEE Electron Device Letters, 2003, 24(8): 500-502..
- [14] Zhou Q, Liu L, Zhang A, et al. 7.6 V threshold voltage high-performance normally-off Al<sub>2</sub>O<sub>3</sub>/Ga<sub>N</sub> MOSFET achieved by interface charge engineering[J]. IEEE Electron Device Letters, 2015, 37(2): 165-168.
- [15] Hanna M J, Zhao H, Lee J C. Poole Frenkel current and Schottky emission in Si<sub>3</sub>N<sub>4</sub> gate dielectric in AlGa<sub>N</sub>/Ga<sub>N</sub> metal insulator semiconductor heterostructure field effect transistors[J]. Applied Physics Letters, 2012, 101(15): 153504.

## Chapter 6: Conclusions and Future Works

### §6.1. Summary and conclusions

$\text{Ni}_x\text{N}$  films were deposited by magnetron reactive sputtering under varying  $\text{P}(\text{N}_2)$  conditions range from 0.005 to 0.184 Pa. With the increasing  $\text{P}(\text{N}_2)$ , the deposition rate decreased while the resistivity and root mean square roughness increased. XRD and XPS indicate that  $\text{Ni}_4\text{N}$  and  $\text{Ni}_3\text{N}$  phases dominate the films at low and medium  $\text{P}(\text{N}_2)$ , respectively. In addition,  $\text{Ni}_2\text{N}$  phase can be also obtained at high  $\text{P}(\text{N}_2)$ . The Ni/N ratio evaluated from the energy dispersive X-ray spectrum is consistent with the  $\text{Ni}_x\text{N}$  phases showed in the XRD spectra of different  $\text{P}(\text{N}_2)$ . Compared with the GaN diodes with Ni anode, the SBH and turn-on voltage of the SBDs with  $\text{Ni}_x\text{N}$  anode were increased with 0.03~0.18 eV and 0.03~0.15 V, respectively.  $C$ - $V$  curves demonstrate that good interface quality with no obvious hysteresis was realized.

$\text{Ni}_3\text{N}$  anode diodes obtained at medium  $\text{P}(\text{N}_2)$  possess a high barrier height and a low reverse leakage current and are regarded as a promising anode material. Compare with the Ni-SBDs, NiN-SBDs show much better rectification characterization, in which the SBH and the turn-on voltage increase 0.2 eV and 0.18V, respectively, and the leakage current is reduced by two orders. The  $I$ - $V$ - $T$  characteristics demonstrate that the NiN-SBDs have better thermal stability than that of Ni-SBDs, owing to the suppression of interface reaction between Ni and GaN. In addition, the thermal stability of GaN diode with NiN anode is potential for temperature sensing application with the sensitivity of approximately 1.3 mV/K.

p-NiO/n-GaN pn diodes and TiN/GaN SBDs were investigated extensively by varying the device diameter and current level. For the NiO/GaN pn diode, it is demonstrated that the series resistance and ideality factor dominate the sensitivity at the fully-turn-on state. However, the series resistance weakly influenced the sensitivity of the TiN/GaN SBDs temperature sensor at the fully-turn-on state. After subtracting the component of series resistance, the sensitivity decreases and increases with the increased device diameters for the p-NiO/n-GaN pn diodes and TiN/GaN SBDs temperature sensors, respectively.

For both type temperature sensors, in the sub-threshold state, a good linear relationship

between sensitivity and the corresponding current density had been observed for devices with different diameters. A low current density was corresponding to the high sensitivity. The NiO/GaN pn diodes and TiN/GaN SBD presenting good thermal stability and linearity from 25 to 200 °C are promising candidates for temperature sensing application.

We also investigated the NiN/GaN SBD for temperature sensor application. While in the sub-threshold region, a good linear relationship between sensitivity and the corresponding current density had been observed for a 200 $\mu$ m diameter NiN/GaN SBD temperature sensor. By comparing with TiN, Ni and NiN electrode GaN SBD temperature sensor, the NiN electrode device showed a near-ideal theoretical sensitivity of a GaN SBD temperature sensor which was calculated by the TE model from GaN based SBDs.

Finally, the NiN was employed as gate electrode on AlGaIn/GaN HFET. The NiN HFET shows good performance good thermal stability, low leakage current and high ON/OFF drain current ratio.

## **§6.2. Suggestion for future works**

Ni<sub>x</sub>N films have been success employed for the Schottky contact, and shown the better rectification characteristic and thermal stability. In the future works, I think we should focus on the following:

1. Further optimize the NiN deposition situation.
2. Study the application for high voltage devices.
3. Study the application of NiN on free-standing substrate.

## **Acknowledgements**

This paper is carried out during my study in the Global Double Degree Program in Department of Electrical and Electronic Engineering, Faculty of Engineering, University of Tokushima, and State Key Laboratory of Information Photonics and Optical Communications, Institute of Information Photonics and Optical Communications, Beijing University of Posts and Telecommunications, from April of 2017 to March of 2020. On the completion of my thesis, I would like to take this opportunity to thank all those who have helped and supported me in completing the academic life.

First and foremost, I would like to give my sincere gratitude to my supervisors, Associate Professor Jin-Ping Ao in the University of Tokushima and Professor Xianjie Li, in Beijing University of Posts and Telecommunications, for their encouragement, patience and selflessness guidance during entire duration of this research work. Without their enlightening instruction, impressive kindness and patience, I could not have completed my thesis. Their keen and vigorous academic observation enlightens me not only in this thesis but also in my future study.

I would especially like to express my deepest thanks to Professor Yongqing Huang and Xiaomin Ren in Beijing University of Posts and Telecommunications for their help me of Global Double Degree Program.

I would like to gratefully acknowledge Department of Electrical and Electronic Engineering, Faculty of Engineering, University of Tokushima for providing the resources and needs during the thesis. I would like to extend my appreciation to Professor Shiro Sakai, Professor Masao Nagase, Professor Yoshiki Naoi, Professor Masanobu Haraguchi, Associate Professor Yasuhide Ohno, Associate Professor Katsushi Nishino, Associate Professor Takuro Tomita, Assistant Retsuo Kawakami, Assistant Yuusuke Takashima, Technician Azuma Chisato, and Takahiro Kitajima for their unconditional help during this research.

I would also especially like to thank Liuan Li in School of Electronics and Information Technology of Sun Yat-Sen University for the support of my research.

I would like to thank Ms. Sawa Asada, Mr. Yunong Wu of CICEE of University of Tokushima for their unconditional help to my life during my study in Tokushima.

I would also thank Mr. Sachio Kobayashie and Researcher Motoo Ito research professorship of Kochi Institute for Core Sample Research, JAMSTEC for their support of my research.

Many thanks extend to the members Tong Zhang, Taofei Pu, Tian Xie, Ruiling Wang, Yuyu Bu, Zhangcheng Liu, Yang Li, Lei Wang, Naoto Okada, Kensaku Yagi, Taiki Hoshi, Nakao Shunsuke, Tsuda Masataka, Chiai Daiki, Morishita Yuto, Aoki Kazuki et al in Ao group, for their help and patience in my research and life.

I would also especially like to thank the China Scholarship Council for the support of living costs.

Last and certainly not the least, I am forever indebted to my parents and wife, who have been supporting me through all of the accomplishments of my academic life. Their indefinite love has made the things different in every aspect of my life.

## Publication list

### Scientific Papers

1. **Xiaobo Li**, Taiki Hoshi, Liuan Li, Taofei Pu, Tong Zhang, Tian Xie, Xianjie Li, and Jin-Ping Ao, “GaN Schottky barrier diode with thermally stable nickel nitride electrode deposited by reactive sputtering”, *Materials Science in Semiconductor Processing*, 93, 1-5, (2019). doi.org/10.1016/j.mssp.2018.12.018.
2. **Xiaobo Li**, Taofei Pu, Hoshi Taiki, Tong Zhang, Tian Xie, Shigeki Joseph Luke Fujiwara, Hiroshi Kitahata, Liuan Li, Sachio Kobayashi, Motoo Ito, Xianjie Li, Jin-Ping Ao “GaN Schottky barrier diodes with nickel nitride anodes sputtered at different nitrogen partial pressure”, *Vacuum* 162, 72–77, (2019). doi.org/10.1016/j.vacuum.2019.01.030.
3. **Xiaobo Li**, Taofei Pu, Tong Zhang, Xianjie Li, Liuan Li, Jin-Ping Ao, “p-NiO/n-GaN heterostructure diodes for temperature sensor application”, *IEEE Sensors Journal*, 20, 62-66, (2020) doi: 10.1109/JSEN.2019.2939045.
4. **Xiaobo Li**, Taofei Pu, Xianjie Li, Liuan Li, Jin-Ping Ao, “Correlation between anode area and sensitivity for the TiN/GaN Schottky barrier diode temperature sensor”, *IEEE Transactions on Electron Devices*, in press, (2020) doi 10.1109/TED.2020.2968358.
5. **Xiaobo Li**, Taofei Pu, Liuan Li, Jin-Ping Ao, “A High Sensitivity Temperature Sensor Structure with Two GaN Schottky Barrier Diodes in Series”, *IEEE Electron Device Letters*, in press, (2020). doi.org 10.1109/LED.2020.2971263.
6. Taofei Pu, **Xiaobo Li**, Taowei Peng, Tian Xie, Liuan Li, and Jin-Ping Ao, “Influence of metal-insulator-semiconductor gate structure on normally-off P-GaN heterojunction field effect transistors”, *Journal of Crystal Growth*, 128, 99–104,

(2020). doi.org/10.1016/j.jcrysgro.2019.125395

7. Liuan Li, **Xiaobo Li**, Taofei Pu, Yang Liu, and Jin-Ping Ao, “Normally-off AlGa<sub>N</sub>/Ga<sub>N</sub> ion-sensitive field effect transistors realized by photoelectrochemical method for pH sensor application”, *Superlattices and Microstructures*, 128, 99–104, (2019). doi.org/10.1016/j.spmi.2019.01.018
8. Taofei Pu, **Xiaobo Li**, Xiao Wang, Yuyu Bu, Liuan Li, and Jin-Ping Ao, “Ga<sub>N</sub> Schottky Barrier Diodes with TiN Electrode for Microwave Power Transmission”, *Materials Science Forum*, 954, 126-132, (2019) doi.org/10.4028/www.scientific.net/MSF.954.126.
9. Tong Zhang, Lei Wang, **Xiaobo Li**, Yuyu Bu, Taofei Pu, Ruiling Wang, Liuan Li, and Jin-Ping Ao, “Positive threshold voltage shift in AlGa<sub>N</sub>/Ga<sub>N</sub> HEMTs with p-type NiO gate synthesized by magnetron reactive sputtering”, *Applied Surface Science* 462, 799–803, (2018). doi.org/10.1016/j.spmi.2018.09.007.
10. Tingting Wang, Xiao Wang, **Xiaobo Li**, Jincheng Zhang, Jin-Ping Ao, "Temperature-Dependent Characteristics of Ga<sub>N</sub> Schottky Barrier Diodes with TiN and Ni Anodes" *Chinese Physics Letters* 36 , 057101 (2019). doi: 10.1088/0256-307X/36/5/057101
11. Liuan Li, Jia Chen, Xin Gu, **Xiaobo Li**, Taofei Pu, and Jin-Ping Ao, “Temperature sensor using thermally stable TiN anode Ga<sub>N</sub> Schottky barrier diode for high power device applications”, *Superlattices and Microstructures*, 123, 274–279, (2018) doi.org/10.1016/j.spmi.2018.09.007
12. Taofei Pu, Xiao Wang, Qian Huang, Tong Zhang, **Xiaobo Li**, Liuan Li, and Jin-Ping Ao, “Normally-off AlGa<sub>N</sub>/Ga<sub>N</sub> heterojunction metal-insulator-semiconductor field-effect transistors with gate-first process”, *IEEE Electron Devices Letters*, 40, (2019),185-188. doi: 10.1109/LED.2018.2889291

13. Tian Xie, Tao Zheng, Ruiling Wang, Taofei Pu, **Xiaobo Li**, Yuyu Bu, and Jin-Ping Ao, “A promising CuO<sub>x</sub>/WO<sub>3</sub> pn heterojunction thin-film photocathode fabricated by magnetron reactive sputtering”, *International Journal of Hydrogen Energy*, 44, 4062-4071, (2019). doi.org/10.1016/j.ijhydene.2018.12.153.
14. Taofei Pu, Qian Huang, Tong Zhang, Jiang Huang, Xiaomin Li, Liuan Li, **Xiaobo Li**, Lei Wang, and Jin-Ping Ao, “Normally-off AlGa<sub>N</sub>/Ga<sub>N</sub> heterostructure junction field-effect transistors with blocking layers”, *Superlattices and Microstructures*, 120, 448-453, (2018). doi.org/10.1016/j.spmi.2018.05.063

#### **International Conference Presentations**

1. **Xiaobo Li**, Taofei Pu, Taiki Hoshi, Tian Xie, Liuan Li, Xianjie Li, Fujiwara Joseph Luke Shigeki, Kitahata Hiroshi, and Jin-Ping Ao, “Nickel Nitride Gate AlGa<sub>N</sub>/Ga<sub>N</sub> HFETs with Low Gate Leakage Current, 2018 International Workshop on Nitride Semiconductors, Kanazawa, Nov. 2018.
2. **Xiaobo Li**, Taofei Pu, Taiki Hoshi, Tian Xie, Liuan Li, Xianjie Li, Fujiwara Joseph Luke Shigeki, Kitahata Hiroshi and Jin-Ping Ao, “Synthesis of nickel nitride electrodes for application on gallium nitride Schottky contact”, 14th IUPAC International Conference on Novel Materials and their Synthesis, Guangzhou, Oct. 2018.
3. **Xiaobo Li**, Tong Zhang, Taofei Pu, Taiki Hoshi, Tian Xie, Xianjie Li and Jin-Ping Ao, “Ga<sub>N</sub> Schottky Barrier Diode with Nickel Nitride Electrode”, The 2018 Asia-Pacific Conference on Silicon Carbide and Related Materials (APCSCRM2018), Beijing, Jul. 2018.
4. **Xiaobo Li**, Xiao Wang, Tingting Wang, Yuyu Bu, Taofei Pu, Tian Xie, Liuan Li, Xianjie Li, Shigeki Joseph Luke Fujiwara, Hiroshi Kitahata, and Jin-Ping Ao, “Synthesis of nickel nitride electrodes for application on gallium nitride Schottky

- contact”, The 2019 Asia-Pacific Conference on Silicon Carbide and Related Materials (APCSCRM2019), Beijing, Jul. 2019.
5. **Xiaobo Li**, Taofei. Pu, Liuan Li, Xianjie Li and Jin-Ping. Ao, “Correlation between anode area and sensibility for the TiN/GaN Schottky diodes temperature sensor”, The 2019 Asia-Pacific Conference on Silicon Carbide and Related Materials (APCSCRM2019), Beijing, Jul. 2019.
  6. **Xiaobo Li**, Hoshi Taiki, Tong Zhang, Xianjie Li, and Jin-Ping Ao, “ GaNSchottky barrier diode with nitride electrode”, The 13th International Symposium on Global Engineering Education, Tokushima, Mar., 2018.
  7. **Xiaobo Li**, Hoshi Taiki, and Jin-Ping Ao, “Nickel nitride Gated AlGaN/GaN HFETs with low gate leakage current fabricated by reactive sputtering”, The 14th International Symposium on Global Engineering Education, Tokushima, Mar., 2019.